Design and Construction Considerations for Hydroelastic Testing of a Truss Floater Platform

By

Julius de Koning

to obtain the degree of

Master of Science

in Offshore and Dredging Engineering
with a specialization in Structural Analysis and Design
at Delft University of Technology

to be defended publicly on Wednesday February 25, 2026

Student number: 4959299

Thesis committee:

Dr. A. Grammatikopoulos	TU Delft	Chairman
Dr. ir. J.H. den Besten	TU Delft	
Dr. J. O. Colomes Gene	TU Delft	
BEng C.F.D. Hoogendoorn	SolarDuck	Supervisor
Ir J. Ruesen	Mocean	Supervisor

Design and Construction Considerations for Hydroelastic Testing of a Truss-Floater Platform

J. de Koning

TU Delft, Delft University of Technology, Mekelweg 5, Delft, 2628 CD, The Netherlands

Abstract

From the existing literature, no scaled models have been reported that combine slamming on cylindrical bodies with global structural compliance. The absence of validated construction methods hinders experimental validation of slamming predictions, which constitute a design-driving load case for the presented structure. To enable controlled investigation of slamming-induced structural response, this study presents the design, construction, and experimental validation of a scaled flexible model representing a three-floater platform using a beam-based structural idealisation. A coupled FEM–BEM numerical framework was developed to design the model based on scaled wet natural frequencies and global mode shapes. The beam system was fabricated using SLA printing with Tough2000 resin, while the floaters were constructed as rigid elements to concentrate flexibility within the connecting beams. Static and dynamic modal testing was performed in both dry and wet configurations. Following material calibration, the numerically predicted natural frequencies and dominant global mode shapes showed good agreement with experimentally identified modes. Natural frequency deviations remained within 7%, and strain-based measurements confirmed accurate reproduction of the primary global deformation patterns. The results demonstrate that the proposed idealised beam and additive manufacturing approach provides a viable methodology for representing global hydroelastic behaviour of *Merganser*-like platforms. The validated modelling framework establishes a foundation for future investigations into slamming-induced transient response.

Keywords: Hydroelasticity, Scaled model testing, Modal analysis, FEM–BEM coupling, Tough2000

1. Introduction

1.1. Research motivation

As global energy demand continues to increase, while the availability of suitable space for large scale Land based Photo-Voltaic (LPV) installations becomes increasingly limited, Offshore Floating Photovoltaic (OFPV) systems have emerged as a promising solution. By enabling energy generation in offshore environments, such systems offer the potential to significantly expand the available area for renewable energy production without competing with land use. Additionally, recent literature has identified that Floating Photovoltaic (FPV) systems can achieve higher energy yield and improved efficiency compared to conventional LPV systems, primarily due to enhanced thermal regulation provided by the surrounding water body (1).

Within this context, several Offshore Floating Photovoltaic (OFPV) concepts have progressed beyond the conceptual design stage towards offshore demonstration. One such example is the *Merganser* platform, as depicted in Figure 1. The platform is a modular triangular shaped concept developed by SolarDuck, in which a truss structure elevates the PV systems above the water surface by means of vertical cylindrical floaters located at each corner. The triangular geometry enables the interconnection of multiple units through damped joints, forming a compliant and scalable array designed for operation in exposed offshore environments.

The elevated connection of the floaters to the truss structure, combined with their one sided attachment, introduces several associated design challenges however. In order to achieve a cost effective solution, the platform is designed to maximise the span between floaters while minimising structural mass. This design inherently results in a relatively flexible structural system and increases the susceptibility of the platform to bending moments generated at the floater attachment points. As a consequence, slamming loads acting on the floaters at- or close to the waterline, which impose such moments around the connecting truss structure, have been identified as a governing design consideration.

Accurate prediction of slamming loads is, however, not straightforward and is subject to multiple sources of uncertainty. Current engineering practice for estimating slamming loads on vertical slender structures, as adopted in design guidelines such as DNV GL (2), is largely rooted in early impact-flow theories originally developed for rigid, bottom fixed cylinders. These approaches originate from von Karman based formulations, as further developed by Goda et al. (3), and were later extended through the introduction of an analytical curling factor by Wienke and Oumeraci (4), based on experimental observations of wave impact on rigidly fixed piles. Such slamming force predictions are typically combined with predefined critical local impact locations along the structure's height, and probabilistic descriptions of wave breaking events, such as

those proposed by Paulsen et al. (5).

Given the importance of slamming loads in the structural design of the platform, it is reasonable to question whether guideline based approaches provide sufficient accuracy for application to a system such as the *Merganser* platform. In a recent literature review, Ma et al. (6) present numerous models for wave slamming on vertical cylindrical structures. While several of these models introduce refinements to existing slamming formulations, they are often still founded in experimental observations in which an attempt is made to either filter structural dynamic response from results, or reconstruct hydrodynamic loads from locally measured structural motion. Ma et al. emphasise that, despite their theoretical basis, these approaches require further development before they can be reliably applied to complex structural systems exhibiting multiple vibration modes or non-linear elastic behaviour.

Given that structural response must be accounted for both in the post-processing of experimental data, as well as in the development or application of predictive numerical slamming models, and existing methods focus primarily on simplified local structural behaviour under rigid boundary conditions (6). The relative flexibility of the *Merganser* platform, combined with its moored boundary conditions, therefore makes sole reliance on numerical modelling challenging when attempting to reliably quantify slamming loads and the associated structural response.

Ma et al. additionally emphasise that laboratory experiments play a central role in advancing understanding of slamming loads on vertical cylindrical structures (6). In parallel, literature reviews on globally flexible ship models by Grammatikopoulos and Jiao et al. highlight the impracticality of obtaining representative full scale data and the difficulty of fully resolving coupled fluid structure interaction through numerical methods alone (7; 8). They equally state that scaled physical experiments remain an indispensable tool for investigating the global dynamic response of flexible marine structures.

In light of these observations, the coupled hydroelastic nature of the problem therefore motivates the development of a scaled flexible experimental model. Such a model enables controlled experimental realisation of slamming events on the floaters and provides a framework for systematically studying the interaction between hydrodynamic loading and global structural response, while also facilitating validation and refinement of numerical models intended to predict this behaviour more accurately. For these reasons, the design and construction of such a scaled flexible model form the central objective of the present study.

1.2. Literature review scaled models

In order to assess which elements are important for the construction of a flexible scaled model, this section outlines several works that describe experimental model set ups used in hydroelastic research. A distinction is made between studies that focus on slamming on cylindrical bodies and those that consider flexibility at a global model scale.

Figure 1: Merganser platform.

1.2.1. Slamming on cylinders experimental set ups

As previously outlined, experimental investigations of slamming forces on vertical cylinders predominantly employ rigidly mounted cylinders subjected to breaking waves under varying scales, inclination angles, and structural configurations (6).

In addition to these rigid support studies, a second class of experiments focuses on capturing both slamming loads and local hydroelastic response. Early hydroelastic impact experiments by Faltinsen (9) demonstrated that elastic deformation of the impacted body modifies the temporal characteristics of slamming loads. Building on this observation, subsequent studies have replaced rigidly fixed cylinders with flexible bodies, typically using two dimensional sections (10) or three dimensional shell structures subjected to controlled free fall conditions (11).

Although these investigations provide valuable insight into local hydroelastic effects during impact, the structural motion in such experiments remains kinematically prescribed. As a result, the dynamic behaviour of a globally compliant structural system is not represented.

1.2.2. Global elastic models

To the author's knowledge, experimental investigations addressing the global hydroelastic response of scaled models with a geometry and structural topology comparable to the *Merganser* platform are currently not available. For ship like structures, however, a substantial body of research exists. These studies therefore provide the primary reference framework for global hydroelastic scaled experimentation.

In such investigations, Froude similitude is adopted to ensure dynamic similarity under gravity dominated wave loading. Geometric similarity between model and full scale structure is preserved, while wave frequencies and structural natural frequencies are scaled according to $\sqrt{1/\lambda}$, with λ denoting the geometric scale factor. Reynolds similarity is typically not enforced, as slamming events are characterised by fully turbulent flow at both model and full scale, rendering viscous effects of secondary importance (12).

Three principal modelling approaches are identified for re-

producing the global elastic response. In segmented model approaches, the structure is discretised into two or more lightweight and structurally stiff segments, which are connected either through a continuous backbone or through a set of flexible joints. Representative backbone based models are presented by Marón and Kapsenberg (13) and by Dessi and Ciappi (14), where aluminium beams are designed using either response based FEM optimisation or analytical formulations. These studies demonstrate how variations in beam cross sectional properties and the introduction of cutouts, combined with careful tuning of the mass distribution, enable accurate reproduction of the global structural response.

Notable examples of flexible joint models are presented by Drummen et al. (15), as well as the segmented catamaran models developed by Lavroff et al. (12; 16). A key advantage of these configurations lies in their adjustability. By tuning the stiffness of torsional springs and joint assemblies, both uniform and non-uniform global stiffness distributions can be realised with relative ease. This versatility is achieved, however, at the expense of an accurate representation of torsional vibration modes, which are typically not fully captured in such modelling approaches.

The third approach, which has gained increasing attention in recent years, involves the use of fully elastic models. These models typically feature continuous shell geometries and internal structural arrangements that more closely reproduce both local and global stiffness distributions. Their design commonly relies on additive manufacturing combined with detailed finite element validation to ensure accurate representation of the target modal properties (7). A representative example is the continuous ship model with an internal arrangement corresponding to a containership, manufactured using 3D printed ABS polymer, as presented by Grammatikopoulos et al. (17).

Another state of the art example of a fully elastic ship model is provided by Chen et al. (18), who document the complete development process of a geometrically scaled model constructed from Lexan resin, including structural scaling, design, manufacturing, calibration, and hydroelastic testing. Across such fully elastic modelling approaches, the importance of accurate material specification and specimen level static and dynamic testing to determine effective material properties prior to structural design is consistently emphasised (11; 18; 19).

From these studies focusing on globally flexible models, it is observed that researchers predominantly aim to capture the first two or three global mode shapes, which are typically comprised of vertical bending behaviour. Examples however exist in which the analysis is extended to four (17) or up to six modes (13). Modal observations are commonly reported for both dry and wet boundary conditions, with wet natural frequencies most commonly predicted through a coupled FEM-BEM approach (20).

Natural frequencies are matched quantitatively and mode shapes most often assessed qualitatively. Numerical measures such as the Modal Assurance Criterion (MAC) have however also been employed to evaluate mode shape correspondence (18). Torsional modes are less consistently captured and are frequently identified as a secondary objective or a limitation of the adopted structural idealisation.

1.3. Research gap

The presented research on wave slamming and hydroelastic response can broadly be divided into two separate domains: studies focused on the prediction of slamming loads on cylindrical elements, and studies addressing the global hydroelastic response of flexible marine structures.

While multiple experimental models exists for slamming on cylinders, these investigations predominantly consider either rigidly fixed or freely falling configurations. Simultaneously, research on ship hydroelasticity has established a structured framework for constructing flexible experimental models to investigate impulsive wave induced global response, however, the direct transfer of this methodology to construction of a floater based platform with global compliance remains uncertain. To the author's knowledge, no established experimental roadmap therefore currently exists, for the design and construction of scaled structures such as the *Merganser* platform.

1.4. Research goal and scope

The objective of this study is to develop a methodology for constructing a scaled flexible model capable of reproducing the global dynamic properties of the *Merganser* platform, thereby providing a foundation for investigating slamming-induced structural behaviour.

By placing emphasis on the accurate scaling of the global dynamic properties, the hydroelastic interaction between slamming excitation and structural response is represented at model scale. Through the observation of structural response during slamming events, this approach enables investigation of the underlying slamming loads, which remain subject to significant uncertainty.

The research goal is considered to be achieved if the developed methodology enables reproduction of the dominant global dynamic characteristics of the platform and allows meaningful comparison between numerically predicted and experimentally measured structural response under controlled laboratory conditions.

In order to reduce problem dimensionality and enable focused investigation of global structural dynamics, the floaters are treated as rigid bodies in the experimental model. Although local hydroelastic deformation of cylindrical members has been shown to influence slamming loads, such effects are likely not dominant for the global response of the platform and are therefore excluded from the present scope. Rigid body motions of the platform and mooring effects are likewise not explicitly modelled. Finally, the present study is limited to the development and validation of the experimental model, rather than the execution of a full slamming test campaign.

1.5. Research outline and validation approach

Based on the scope defined in the preceding sections, the overall research structure adopted in this work is summarised in Figure 2. As initial steps, the target global dynamic properties of the full scale *Merganser* platform are identified, together

with relevant material and manufacturing constraints. These form the basis for a proposed structural idealisation of the platform, As outlined in Chapter 2.

The defined target properties and structural idealisation are subsequently employed within a numerical framework that combines hydrodynamic added mass prediction and response based structural optimisation. This framework is used to derive a set of structural parameters intended to represent the target global behaviour under wet conditions. The numerical design procedure is described in Chapter 3. The resulting parameters are then translated into a detailed geometric design suitable for additive manufacturing, as presented in Chapter 4.

Following manufacturing and assembly of the scaled platform, experimental modal testing is performed to characterise the dynamic response of the structure. In addition, static beam tests are conducted to support interpretation of the structural behaviour and to reassess effective material properties. The experimental methodology, instrumentation layout, and testing procedures are described in Chapter 5.

Validation of the proposed methodology is achieved by comparing experimentally obtained measurements with construction based numerical predictions. This comparison is used to assess the accuracy of the modelling assumptions and the robustness of the adopted design and construction approach. The results of this comparison are presented in Chapter 6. Finally, the main findings of the study are discussed in Chapter 7 and conclusions are drawn in Chapter 8.

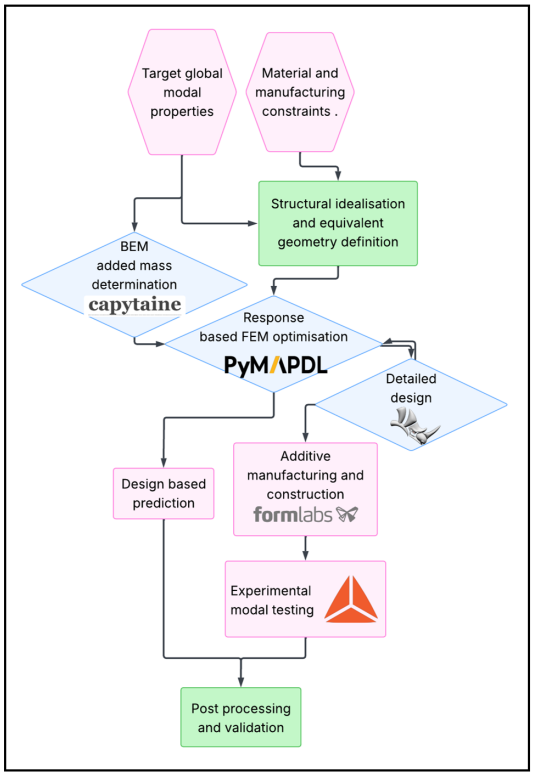

Figure 2: Research structure.

2. Design basis for the scaled elastic platform

Following the definition of the research objectives and scope in Chapter 1, this chapter establishes the proposed structural and construction methodological basis for the development of the scaled elastic model. First, the relevant global deformation patterns of the *Merganser* platform are identified in Section 2.1. The adopted similitude strategy and corresponding scaling of dynamic properties are then defined in Section 2.2.

Subsequently, the structural abstraction of the platform into rigid floaters and an equivalent beam representation is introduced in Section 2.3. The selected additive manufacturing strategy is outlined in Section 2.4, followed by the motivation for material selection and the adopted initial material properties in Section 2.5. Finally, the specimen-level material investigations used to assess and calibrate the effective stiffness parameters are presented in Section 2.6.

Together, these elements define the design basis of the scaled model and provide a framework for the numerical modelling, optimisation, and experimental validation presented in the subsequent chapters.

2.1. Target global Merganser modeshapes

From the literature review presented in Section 1.2.2, it is observed that most studies primarily aim to capture the first global bending modes. For the *Merganser* platform, however, it cannot be readily assumed that a single mode will dominate the structural response during slamming. Since slamming loads act directly on the floaters, any mode involving significant floater rotation is likely to be excited and should therefore be reproduced as accurately as possible.

Free decay tests were performed on the *Merganser* platform to identify structural modes. During these tests, three mode shapes characterised by pronounced floater rotations were observed. The corresponding mode shapes are shown in Figure 3, while the associated natural frequencies and damping ratios are summarised in Table 1.

The vertical lines in Figure 3 represent the floaters located at each corner of the platform, whereas the deformation of the truss structure spanning the centre of the platform is represented by lines along its edges. From this figure it can be observed modeshapes are not easily identified with respect to a global longitudinal or transverse axis. Instead, they are more clearly distinguished by the relative rotations of the floaters about the horizontal axes at each corner. For this reason, each target mode is characterised by the orientation of the combined horizontal rotation axis with the global x axis. This angle is provided for all target modes in Table 1.

Based on the observed deformation patterns, a naming convention is adopted for the identified flexible modes. Mode 1 exhibits a predominantly asymmetric deformation pattern and is therefore referred to as the asymmetric mode. Modes 2 and 3 correspond to inward directed and tangential leg motions with respect to the platform centre, respectively, inducing dominant global bending and torsional deformation of the truss structure. These modes are therefore referred to as the global bending and torsion modes.

Table 1: Observed model scale modal properties and corresponding target values.

Mode	Type	Description	f_{model} [Hz]	f_{target} [Hz]	ζ [%]	θ_A [°]	θ_B [°]	θ_C [°]
–	Rigid	Heave	0.18	0.80	2.19	–	–	–
–	Rigid	Pitch 1	0.19	0.85	0.40	–	–	–
–	Rigid	Pitch 2	0.24	1.07	9.43	–	–	–
1	Flexible	Asymmetric	2.37	10.60	0.90	0	0	90
2	Flexible	Bending	2.80	12.52	1.41	120	60	0
3	Flexible	Torsion	3.93	17.58	1.68	30	150	90

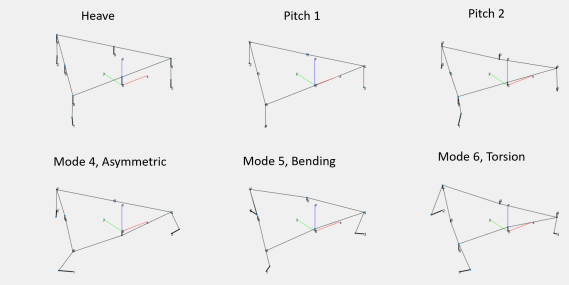

Figure 3: Experimentally observed mode shapes of the TFP obtained from decay tests.

2.2. Scaling factor determination

It is well established that increasing the geometric scale factor, s_f, reduces the relative influence of scale effects on the measured response (8). Consequently, the largest feasible scale factor was sought. As outlined in Section 1.2, scaled flexible models are developed in accordance with Froude similitude (7). Consequently, all hydrodynamically loaded dimensions are scaled linearly by a factor s_f. Since mode shapes are governed by strain, which is a dimensionless quantity, they remain invariant under scaling. Consistent with Froude similitude, the corresponding natural frequencies scale with $s_f^{-1/2}$. The resulting natural frequencies are presented in Table 1.

The geometric scale factor was set to $s_f = \frac{1}{20}$. This choice was governed by the intended experimental application of the model. Given the known dimensions of the wave tank in which the tests were to be conducted, the maximum submerged cross-sectional area of the floaters was compared with the tank cross-sectional area. To limit wall interference effects, the submerged cross-section of the scaled model was restricted to a maximum of 5% of the tank cross-section.

2.3. Structural idealisation

To enable reproduction of the target global dynamic response at model scale, within the proposed methodology, the floaters are connected using beam based components, as illustrated in Figure 4. Following the methodology of Marón and Kapsenberg, a numerical optimisation procedure is employed to identify a beam design capable of capturing the target global mode shapes presented in Section 2.1.

The three floaters are labelled A, B, and C, while the connecting beams are denoted by the corresponding floater pairs AB, BC, and CA, a convention that is adopted consistently throughout this work. Beam representations allow efficient tuning of bending and torsional stiffness and naturally support segmentation for local stiffness variation. This modelling strategy has been shown to facilitate accurate reproduction of global dynamic behaviour in scaled hydroelastic models (13; 14).

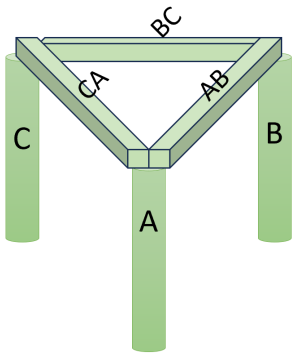

Figure 4: Proposed model layout

2.3.1. Infeasibility exact geometric scaling

As the floaters of the *Merganser* platform are connected through a truss structure, a preliminary investigation was conducted into the feasibility of geometrically accurate scaling of this configuration. When individual truss members are approximated as Euler–Bernoulli beams under bending, correct reproduction of their dynamic behaviour requires simultaneous scaling of the bending stiffness EI and the structural mass per unit length μ. This approach is commonly applied in the scaling of global bending frequencies of ship-like structures (7).

However, the truss members of the *Merganser* platform are not solely loaded in bending but also experience significant axial forces. As a result, the cross-sectional properties cannot be neglected and the axial stiffness EA must be scaled consistently as well. These combined scaling requirements for EI, μ, and EA cannot be satisfied simultaneously using practical model-scale materials and cross-sections. Consequently, direct geometric scaling of the truss structure is considered impractical and is therefore abandoned.

It is noted that the truss structure of the *Merganser* platform contributes a significant portion of the total structural mass, much of which is concentrated near the geometric centre of the platform. As a result, the associated rotational inertia cannot be reproduced exactly using the adopted beam based representation. Consequently, the pitching frequency of the scaled model is not expected to scale accurately. This limitation is acknowledged and accepted within the scope of the present study.

2.4. SLA additive manufacturing

The connecting beams will be manufactured using stereolithography (SLA) additive manufacturing with a Formlabs Form 4 printer. This production technique is adopted to enable the realisation of sufficiently flexible beam geometries resulting from the proposed optimisation design method.

The relatively flexible nature of the *Merganser* platform results in scaled target natural frequencies that are low compared to values commonly reported in the literature. Preliminary investigations indicated that the use of aluminium beams, as employed in many existing hydroelastic model studies, would require extremely slender cross-sections with extensive cutouts to achieve the required stiffness reduction. Such configurations were considered impractical with respect to manufacturability and instrumentation. Additive manufacturing therefore provides a practical alternative by enabling greater geometric freedom while allowing the use of materials with lower elastic stiffness.

For thermoplastic materials such as polylactic acid (PLA), manufacturers typically report distinct material properties parallel and perpendicular to the print direction, reflecting pronounced anisotropy. In contrast, experimental studies on SLA printed resins have shown that material properties are not significantly influenced by printing orientation, indicating reduced sensitivity to build direction compared to FDM based methods (21).

As anisotropic material behaviour would introduce additional complexity in the predictive modelling and calibration of the structural response, such behaviour was considered undesirable in the present study.

Although polymer based materials, including resins and polycarbonate, have been employed in hydroelastic model construction (11; 18), the use of SLA printing as the primary manufacturing method for the production of a scaled hydroelastic platform has, to the authors' knowledge, not been reported in the existing literature.

2.5. Material selection

Two materials were considered for production of the beams of the model, Clear resin and Tough2000 resin. From the material tests presented in the following section, Tough 2000 was selected for the construction of the scaled elastic model. Tough 2000 is the strongest engineering resin advertised by the manufacturer which is compatible with the Form 4 printer.

Experimental characterisation of Tough 2000 reported in the literature indicates favourable elastic behaviour and good interlayer bonding when printed using standard SLA processes (22). However, a pronounced sensitivity to post curing time and temperature has also been reported (23).

Manufacturer provided material properties for Tough 2000 are summarised in Table 2 (24). The reported tensile and flexural moduli are based on quasi static coupon tests conducted in accordance with ASTM D638 and ASTM D790 standards. In literature, however, experimental studies report a wide range of quasi static Young's modulus values, ranging from approximately 0.8 GPa to values exceeding 3.0 GPa, depending on testing method, processing and curing conditions (22; 23).

Table 2: Post cured material properties used for numerical modelling, as reported by the manufacturer.

Property	Tough 2000
Tensile modulus [GPa]	2.2
Flexural modulus [GPa]	1.9
UTS [MPa]	46
Density [g/cm^3]	1.21

2.6. Material specimen tests

Given the wide range of reported quasi static material properties for Tough 2000, and in accordance with previous studies highlighting the importance of material validation prior to constructing fully elastic models (11; 18; 19), a series of material specimen tests was conducted before fabrication of the connecting beams.

Polymer based materials may exhibit viscoelastic behaviour and strain rate dependent stiffness, which can lead to differences between quasi static and dynamic material response. Since the available literature and manufacturer data for Tough 2000 are limited to quasi static tests, while the present study focuses on dynamic structural behaviour, emphasis was placed on a preliminary dynamic characterisation of the material properties. The quasi static flexural moduli were subsequently determined and later compared with dynamic observations obtained after beam assembly.

The material characterisation methodology proposed by Grammatikopoulos et al. (19) was adopted. This approach identifies effective material properties by matching experimentally observed natural frequencies to corresponding numerical predictions.

In practice, the specimen tests did not permit accurate identification of a unique effective Young's modulus. The experimentally identified natural frequencies exhibited substantial scatter between repeated measurements, excitation locations, and sensor configurations. The magnitude of this variability was comparable to the frequency shifts produced by plausible variations in Young's modulus within the numerical model. Consequently, iterative tuning of the material properties based solely on specimen level dynamic tests proved inherently ambiguous.

Despite this limitation, the experimentally observed natural frequencies were consistently bounded by numerical predictions obtained using Young's moduli between 1.9 and 2.2 GPa. Based on observations, a representative Young's modulus of 2.0 GPa was adopted for subsequent numerical analyses. A detailed description of the test setup, data processing, and specimen level results is provided in Appendix A.

3. Numerical design

The objective of the numerical design phase is to develop a structural representation that reproduces the targeted global hydroelastic behaviour of the *Merganser* platform while remaining manufacturable and compatible with experimental validation, within the framework outlined in Chapter 2

Achieving this requires a modelling approach capable of predicting the coupled structural and hydrodynamic response and enabling systematic adjustment of structural parameters toward the desired modal characteristics.

Based on literature, a coupled FEM–BEM approach provides a robust and accessible strategy for modelling such systems (20). This framework is therefore adopted in the present study.

Section 3.1 describes the implementation of the BEM formulation. The structural idealisation and parametrised beam representation adopted in the FE model are detailed in Section 3.2. The optimisation strategy used to identify a beam geometry that best reproduces the target modal properties is presented in Section 3.3. Finally, the resulting numerical modal characteristics and local beam behaviour are discussed in Section 3.4.

3.1. BEM analysis

The BEM model is implemented in Capytaine, where the floaters are represented as scaled rigid bodies. The floater geometries were discretised using a surface mesh compatible with conventional potential flow solvers, allowing direct use within Capytaine. Mesh convergence was verified by monitoring the computed modal added mass under successive refinements. Further refinement beyond the selected resolution resulted in negligible changes, indicating mesh-independent hydrodynamic coefficients within the frequency range of interest.

3.1.1. Modal added mass determination

Modal added mass is commonly determined by prescribing structural mode shapes in a boundary element model and subsequently coupling the resulting hydrodynamic coefficients to a finite element model to obtain wet natural frequencies. As the wet modes depend on the hydrodynamic added mass, while the added mass itself is evaluated from wet modeshapes at the wet natural frequency, this procedure is inherently non-linear and is typically solved using an iterative FEM–BEM coupling approach (25).

From preliminary BEM simulations, however, an opportunity for numerical simplification was identified. Figure 5 shows the frequency-dependent modal added mass for the target global modes, as well as for three individual floaters undergoing pitch motion about their tops.

The computed modal added mass was found to vary only marginally over the frequency range relevant for the scaled model, with differences on the order of 1–2%, and no dependence on the imposed mode shape or floater rotation axis was observed.

As shown in Figure 5, the added mass curves corresponding to the different modes and the simplified pitch motion have converged within the frequency range of interest. This indicates

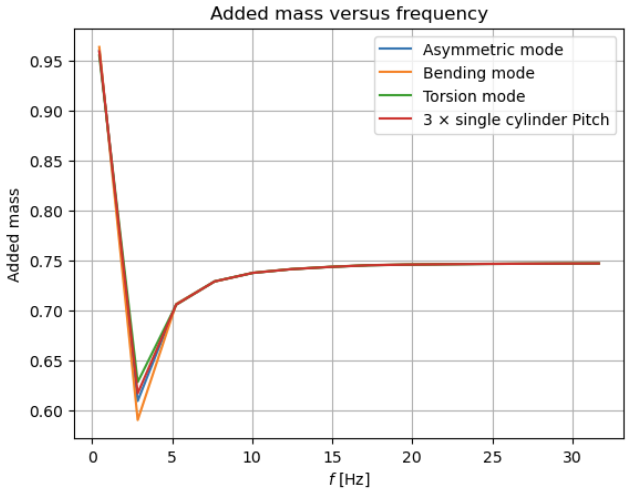

Figure 5: Frequency dependent added mass obtained from BEM.

an absence of hydrodynamic interaction between the floaters across the considered modes and frequencies.

Based on these observations, the modal added mass may be approximated as a constant rotational inertia, $A_{\theta\theta}$, for each individual floater, independent of frequency and rotation direction. As $A_{\theta\theta}$ is constant, it can be incorporated directly into the finite element model, thereby eliminating the need for iterative FEM–BEM coupling during the optimisation process. This simplification results in a substantial reduction in computational cost without a meaningful loss of accuracy for the present application.

3.1.2. Translational added mass

To incorporate $A_{\theta\theta}$ into the FE model, it must however be converted into an equivalent translational added mass M_{eq}. This can be done using Equation 1, where l denotes the effective lever arm between the prescribed pitch axis and the centre of hydrodynamic loading.

$$M_{\text{eq}} = \frac{A_{\theta\theta}}{l^2}, \tag{1}$$

Finding a suitable value of l however poses a challenge, as the instantaneous centre of rotation of the floaters emerges from the combined effects of structural mass distribution, hydrodynamic added mass, and structural stiffness, and can therefore not be assumed to be equal for each mode.

To assess the sensitivity of the adopted added mass formulation to the centre of rotation height, a parametric study was performed in which the rotation axis height was varied systematically. The results are presented in Figure 6a.

This figure shows the equivalent translational added mass M_{eq} as a function of the normalised rotation axis height l. The dotted curves indicate the corresponding surge added mass A_{xx} evaluated at identical frequencies. Figure 6b presents the rotational added mass $A_{\theta\theta}$ over the same normalised range of l.

It can be observed that while $A_{\theta\theta}$ increases over the specified range of l, M_{eq} quickly converges towards A_{xx} as the rotation axis is moved upward, with convergence occurring already for

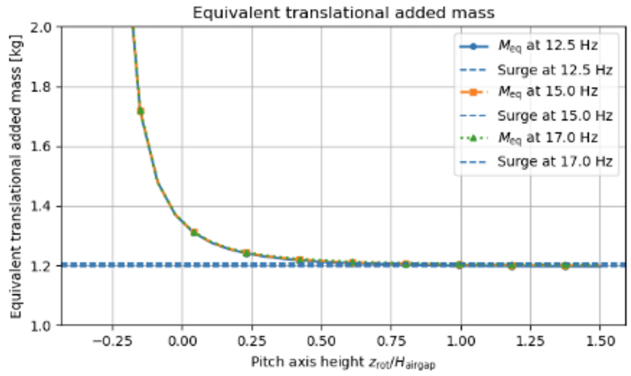

(a) Equivalent translational added mass M_{eq} and Surge added mass A_{xx}.

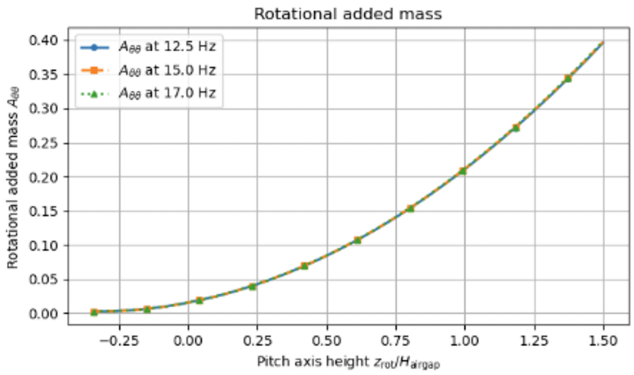

(b) Rotational added mass $A_{\theta\theta}$ as a function of l.

Figure 6: Added mass axis of rotation sensitivity study.

rotation axis heights at around 50% the floater height. This behaviour is consistent across the investigated frequency range.

Importantly, this variation in $A_{\theta\theta}$ does not translate into significant differences of M_{eq} within a physically plausible range of rotation centres. It is therefore assumed that the adopted M_{eq} representation is robust with respect to plausible variations in the global kinematics of the platform. This simplified added mass formulation will therefore not likely compromise the accuracy of the global modal response, while avoiding the need to resolve the exact instantaneous centre of rotation within the optimisation framework.

3.2. FEM modelling

The structural model is implemented in the ANSYS Mechanical APDL environment through the PyMAPDL interface. Embedding the modelling workflow in PyMAPDL allows geometry generation, meshing, boundary condition assignment, and post processing to be fully scripted. This facilitates automated parameter variation and direct export of modal properties to externally defined optimisation routines.

The model formulation is divided into three primary components: the connecting beams, which are subject to optimisation; the floaters, which are modelled as representative cylindrical shells; and the beam–floater interfaces (BFIs) that connect the two.

3.2.1. Beam formulation

The development of the connecting beams is governed by a set of practical and modelling driven constraints. Their geometry must be accurately representable within a numerical framework, reliably manufacturable using additive manufacturing, and compatible with segmentation and mechanical connections between components, as printed components are limited in size. In addition, the geometry must allow for the integration of strain gauges for experimental validation and result in a structure that is sufficiently robust to withstand repeated handling and testing without degradation.

Additionally, based on the mode shapes presented in Section 2.1, it is evident that the connecting beams must accurately represent both bending and torsional behaviour. To achieve this, the geometry will be varied between segments, as this will allow for locally adjusting the stiffness in regions dominated by bending or torsional deformation.

The assumption is that this will enable control over the relative contribution of these mechanisms, thereby facilitating reproduction of the targeted global mode shapes and spacing between natural frequencies.

Within these constraints each connecting beam is assigned a square hollow cross section as a baseline geometry. The cross section is defined in the transverse plane by four keypoints and characterised by the overall height H and width B. The beams are of length L_b, which is fully prescribed by the scaled floater geometry, are divided into N_s segments by the ordered set of segment boundaries $0 = x_0 < x_1 < \ldots < x_{N_s} = L_b$.

By defining the cross section at each segment boundary, a set of eight keypoints encloses the volume of an individual segment, from which four shell areas are generated. To reduce torsional stiffness, cutouts are introduced in the segment webs. Each segment $i = 1, \ldots, N_s$ is therefore defined by its flange thickness $t_f^{(i)}$ and cutout geometry, characterised by the cutout height $h_{\text{co}}^{(i)}$ and width $w_{\text{co}}^{(i)}$. To ensure manufacturability, the section height H, global width B, and web thickness t_w are kept constant along the beam length. A schematic overview of the resulting segment geometry and cutout definition is shown in Figure 7.

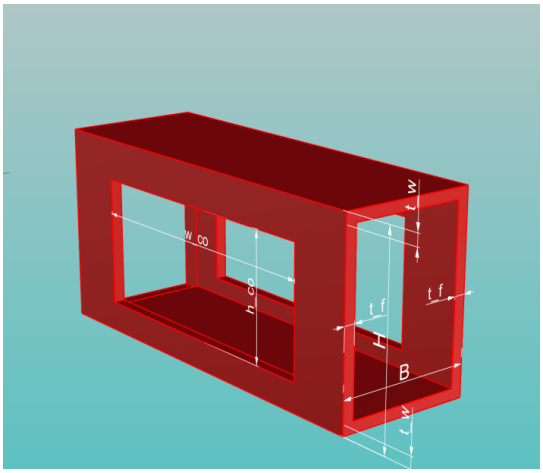

Figure 7: Geometric reference model of the beam segment.

To limit the design space, the cutout geometry was controlled by a single scalar parameter per segment, governing both cutout dimensions. Additionally, all parameters are applied symmetrically about the mid plane of the beam cross-section. Sectional properties such as cross-sectional area, bending rigidities, torsional rigidity, and mass per unit length are quantities derived from the presented parameters.

As the bending stiffness is primarily governed by the section height H and the flange thickness $t_f^{(i)}$, while the torsional stiffness is predominantly influenced by the cutout dimensions $h_{\text{co}}^{(i)}$ and $w_{\text{co}}^{(i)}$, as well as the global width B and web thickness t_w, this beam segment definition was assumed to provide a sufficient design space for independent modal tuning.

The resulting thin to moderately thick plate like walls are well suited for both additive manufacturing and numerical discretisation. In particular, this geometry can be accurately represented using SHELL181 elements.

The choice of SHELL181 elements was motivated by the moderately thick nature of the beam walls and the need to retain through thickness effects, transverse shear deformation, and consistent representation of bending moments within each element. Alternative representations such as plate elements were therefore not suitable.

3.2.2. Floater formulation

As outlined in Section 1.4, local flexibility of the floaters is outside the scope of the present study. Nevertheless, it was recognised that no available material with sufficiently low mass would behave as perfectly rigid in practice. The floater material and thickness were therefore selected at an early stage based on anticipated manufacturing constraints and experimental feasibility.

PMMA extrusion was chosen for the construction of the floaters. The corresponding material properties were prescribed directly in the numerical model and kept fixed throughout the optimisation process. A detailed justification of the selected material, as well as the adopted thickness, material properties, and construction approach, is provided in Section 4.3.2.

3.2.3. Beam-floater interface formulation

A key modelling decision concerns the representation of the structural interface between the connecting beams and the floaters. The Beam–Floater Interface (BFI) transfers all hydrodynamic loads from the floaters into the beam network and therefore influences the global structural response.

In the present study, the mechanical behaviour of the BFI is not treated as a design parameter, as introducing connection compliance would expand the design space without contributing to the primary objective. The BFI's are therefore idealised as rigid.

In the numerical model, this is implemented by allowing the outer beam segments to intersect directly with the floater tops, which are modelled as rigid shells, resulting in effectively clamped boundary conditions.

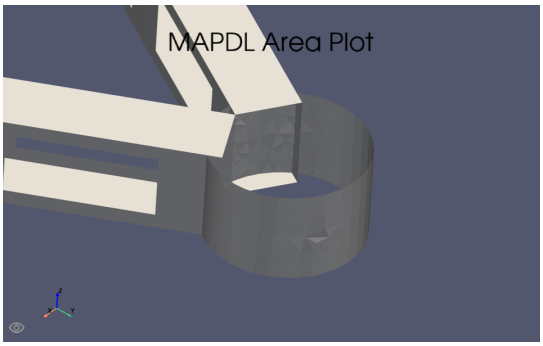

Figure 8: Beam-floater interface area representation.

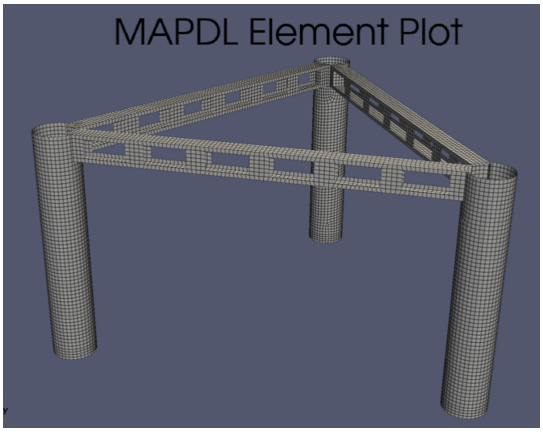

Figure 9: Element representation full model.

3.2.4. BEM-FEM coupling

The observed values of A_{xx} from the equivalent added mass formulation presented in Section 3.1 were implemented in the horizontal directions within numerical model using MASS21 elements. These elements were placed at a vertical position $T/2$ in the centre of the horizontal floater cross-section. The A_{zz} was equally obtained from single floater BEM analysis and applied directly in the vertical direction. The MASS21 elements were connected to all structural nodes located below the still water level using RBE3 constraints.

3.3. Optimisation based beam design

The beam geometry was determined through a constrained optimisation procedure formulated to match the targeted modal properties. Sections 3.3.1 and 3.3.2 define the optimisation framework and objective function, while Section 3.3.3 outlines the staged solution strategy adopted to solve the problem.

3.3.1. Optimisation framework and design space definition

An element based representation of the full numerical model is shown in Figure 9. The mesh size was set to 10 mm based on a mesh convergence study, in which the first natural frequencies were evaluated as a function of element size. The results indicated that further mesh refinement had a negligible influence on the predicted modal response.

The parametric beam formulation introduced in Section 3.2.1 represented the only variable inputs for the numerical optimiser.

Manufacturing constraints were incorporated directly into the optimisation problem to ensure that all candidate designs were compatible with additive manufacturing. These constraints included minimum allowable wall thicknesses, discretisation of geometric parameters to reflect printer resolution and maximum component size, as well as geometric feasibility limits on cutout dimensions and spacing required to preserve local structural integrity.

The feasible design space $\mathcal{D}$ was therefore defined by a set of bound and inequality constraints,

$$\mathcal{D} = \{\theta \mid \theta_{\min} \le \theta \le \theta_{\max},\ g_i(\theta) \le 0,\ i = 1, \ldots, N_c\}, \quad (2)$$

where $\theta_{\min}$ and $\theta_{\max}$ denote lower and upper bounds on the geometric parameters, and $g_i(\theta)$ represent additional geometric feasibility constraints. As a result, all optimised designs were immediately manufacturable without requiring post processing adjustments. Within each optimisation run, the generated geometry was assessed for a predicted mass, by subtracting this mass from target scaled platform weight, a ballast mass was calculated which was placed as MASS21 elements at the floater bottoms.

3.3.2. Objective function determination

A suitable objective function and associated weighting factors had to be defined. While direct comparison between experimentally observed and numerically predicted mode shapes through evaluation of the Modal Assurance Criterion (MAC) has been applied in literature (18; 26), in the present case deformation is confined to the beams, whose behaviour cannot be compared to full scale measurements. As a result, such comparisons can only be meaningfully applied to the floater rotation angles presented in Table 1.

Early exploratory optimisation runs demonstrated that the natural frequency and order of the observed modeshapes varied between different beam geometries. The floater rotation angles, however, converged immediately and were found to be insensitive to variations in the beam geometry.

Consequently, inclusion of the MAC within the objective function did not provide additional optimisation sensitivity and therefore did not improve convergence toward a desirable solution. The MAC was therefore employed only as a validation criterion, whereby the final rotation patterns of the floaters were used to identify the corresponding global modes and verify that they occurred in the correct order. Solutions for which this condition was not satisfied were penalised accordingly.

Exploratory runs also indicated that minimisation of absolute frequency errors alone led to solutions in which a single mode was matched accurately, while other modes remained poorly represented. To mitigate this behaviour, the optimisation objective was formulated to incorporate both absolute frequency accuracy and preservation of modal spacing. The resulting objective function is defined in Equation 3.

$$\mathcal{J} = w_f \frac{1}{N_m} \sum_{k=1}^{N_m} \left| \frac{f_k^{\text{mod}} - f_k^{\text{tar}}}{f_k^{\text{tar}}} \right| + w_r \frac{1}{N_r} \sum_{j=1}^{N_r} \left| \frac{r_j^{\text{mod}} - r_j^{\text{tar}}}{r_j^{\text{tar}}} \right| \quad (3)$$

The variables f_k^{mod} and f_k^{tar} denote the modelled and target natural frequencies of mode k, respectively, while r_j denotes the ratio between selected pairs of natural frequencies. The weighting factors w_f and w_r control the relative importance of absolute frequency accuracy and preservation of modal spacing. The most robust convergence was obtained when preservation of relative modal spacing was prioritised over absolute frequency accuracy, corresponding to weighting factors of approximately $w_r \approx 3w_f$.

3.3.3. Staged optimisation strategy

Given the highly non-linear relationship between beam geometry and global modal response, a staged optimisation strategy was adopted to balance global exploration and efficient convergence. In the initial stage, a broad exploration of the feasible design space was performed using quasi random sampling based on low discrepancy Sobol sequences, which provide improved space filling properties in high dimensional parameter spaces compared to purely random sampling. This phase was used to identify promising regions of the design space while reducing sensitivity to local minima.

In the subsequent stage, the optimisation was refined using a Tree-structured Parzen Estimator sampler, which constructs probabilistic models of favourable and unfavourable regions of the design space and progressively biases sampling toward regions associated with lower objective values.

During the optimisation process, the beam width B consistently converged toward its maximum manufacturable value and was therefore fixed in later optimisation stages. A similar procedure was applied to the beam height H, after which the optimisation focused on progressively narrower bounds for thickness and cutout related parameters. This staged reduction of the design space reduced sensitivity to local minima while preserving sufficient flexibility to tune the global modal properties.

3.4. Optimisation results

This section presents the numerical optimisation results. First, the observed global modes are introduced and compared to the target behaviour in Section 3.4.1. The inherent competing stiffness requirements are then analysed in Section 3.4.2, followed by the final beam design selection in Section 3.4.3. Finally, the resulting global beam behaviour and local strain effects are examined in Sections 3.4.4 and 3.4.5.

3.4.1. Observed numerical modes

The three scaled frequencies presented in Table 1 were used as target values in the objective function. However, six global modes were identified in the numerical analysis. Top view visualisations of these modes, together with their adopted labels, are shown in Figure 10.

The corresponding natural frequencies are listed in the third column of Table 4. As can be observed, modes 1a and 1b, as well as modes 4a and 4b, occur in close frequency proximity and exhibit highly similar global deformation patterns. These closely related modes are therefore distinguished using letter suffixes.

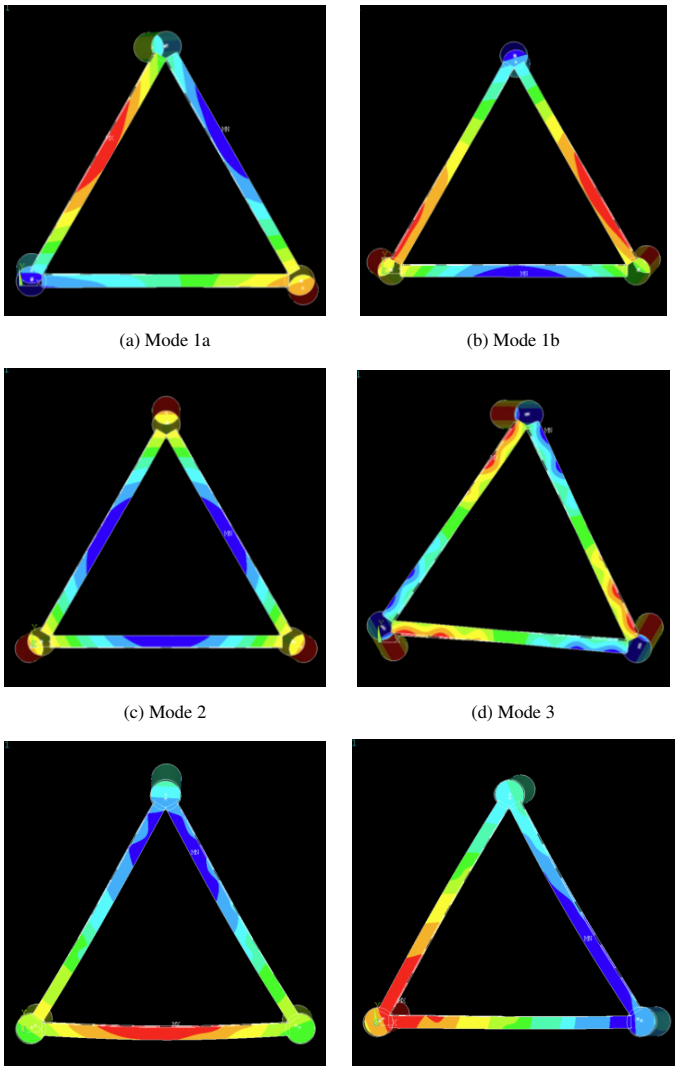

(a) Mode 1a (b) Mode 1b

(c) Mode 2 (d) Mode 3

(e) Mode 4a (f) Mode 4b

Figure 10: Top view global mode shapes. Colours indicate vertical translation.

Figure 10 further demonstrates that the floater rotation patterns of Modes 1a, 2, and 3 accurately reproduce the full scale floater rotations presented in Table 1.

3.4.2. Competing stiffness requirements

As can be observed in Table 4, modes 1a and 1b are predicted at a frequency lower than targeted, while modes 2 and 3 are predicted at a higher frequency. Despite numerous attempts, and elaborate tuning of the optimiser, the spacing between these modes could not be reduced. To assess possible effects leading to this inability to accurately reproduce all modes, the system is analysed further.

The insensitivity of the modeshapes to local beam stiffness tuning highlighted in Section 3.3.2 indicates that the global dynamic response is governed primarily by overall beam stiffness levels rather than by segment wise geometric detail.

To investigate whether a beam design unconstrained by manufacturing limitations could reproduce the targeted frequency spacing, an equivalent platform model was constructed using BEAM188 elements. A detailed outline is provided in Appendix B.1. Within this representation, both the bending stiffness EI and torsional rigidity GJ were varied over a wide range of scaling factors in order to explore the uncoupled stiffness space.

Again, the same six global modeshapes were observed irregardless of beam characteristics, confirming that the deformation characteristics are primarily governed by symmetry and connectivity rather than detailed beam geometry. Additionally, despite substantial variation of both bending and torsional stiffness, no combination of parameters allowed exact matching of the targeted frequency spacing.

Even when the torsional constant J was reduced toward zero, the torsion dominated mode remained at a relatively high frequency. Inspection of the associated deformation pattern revealed that this mode induces three node bending in the beams, and that torsional modes are therefore not governed solely by GJ but also by bending contributions. As a result, bending and torsional modes cannot be tuned independently in this BEAM188 configuration and a perfect frequency spacing could equally not be attained.

It is found likely that similar competing stiffness effects inherent to the BEAM188 representation impose a minimum spacing between modes 1a and 1b, with regard to modes 2 and 3 of the SHELL181 representation.

3.4.3. Beam design selection

As no perfect match could be found, an additional optimisation run was performed in which the beam geometry was set to the minimum manufacturable segment count of six, and constrained to be uniform along its length, allowing the achievable accuracy of a simplified design to be assessed directly.

The resulting geometries from both the detailed and uniform six segment optimisation runs are summarised in Table 3. The natural frequencies are depicted in Table 4.

Adoption of a uniform segment design offers several practical and analytical advantages. A uniform beam configuration is more straightforward to interpret and analyse than a segmented design, while also simplifying manufacturing and assembly.

As the uniform segment optimisation yielded natural frequencies that differed only modestly from those obtained with the segmented configuration, the reduction in numerical accuracy was considered acceptable. The uniform beam design was therefore selected as the final configuration for further numerical analysis and experimental realisation.

3.4.4. Global beam behaviour

Further insight is obtained by analysing beam level deformation characteristics, including bending, axial strain, and twist distributions as functions of the normalised beam coordinate s/L of the targeted global modes 1a, 1b, 2 and 3. These quantities were extracted by tracking a narrow strip of nodes along the mid-span of the top and bottom beam surfaces, where values were obtained by averaging over pairs of adjacent nodes. This approach yields representative results while reducing sensitivity to local stress concentrations at the beam edges. The extracted distributions are directly comparable to experimental

Table 3: Beam design parameters obtained from segmented and uniform optimisation runs.

Parameter	Segmented	Uniform
Number of segments N_s	6	6
Web thickness t_w [mm]	2.0	4.0
Flange thickness $t_f^{(1)}$ [mm]	7.5	4.0
Flange thickness $t_f^{(2)}$ [mm]	3.5	4.0
Flange thickness $t_f^{(3)}$ [mm]	3.0	4.0
Cutout width $w_{co}^{(1)}$ [mm]	117.3	100.9
Cutout width $w_{co}^{(2)}$ [mm]	95.04	100.9
Cutout width $w_{co}^{(3)}$ [mm]	95.04	100.9
Cutout height $h_{co}^{(1)}$ [mm]	56.00	49.6
Cutout height $h_{co}^{(2)}$ [mm]	45.36	49.6
Cutout height $h_{co}^{(3)}$ [mm]	45.36	49.6

Table 4: Target and numerically predicted natural frequencies with relative errors for segmented and uniform beam configurations.

Mode	f_{tar}	f_{seg} [Hz]	Error [%]	f_{uni} [Hz]	Error [%]
1a	10.60	10.05	−5.19	9.51	−10.28
1b	10.60	10.06	−5.09	9.53	−10.09
2	12.52	12.98	+3.67	13.24	+5.75
3	17.54	17.88	+1.94	17.67	+0.74
4a	–	26.12	–	25.93	–
4b	–	26.13	–	25.94	–

strain measurements if corresponding strain gauges were applied at these locations.

The deformation fields shown are normalised with respect to their maximum modal amplitude and are therefore intended to illustrate spatial distributions and relative phase behaviour rather than absolute magnitudes. The corresponding peak deformation amplitudes, derived from the modal analysis, are reported separately in Table 5. Representative beam-level deformation fields for the first two global modes are shown in Figure 12a and 12b, while the characteristic behaviour of the higher modes is illustrated in 12c and 12d.

All beams exhibit axial strain and twist distributions that are heavily locally influenced by the presence of cutouts at the segment level. When the average strain response for each segment is considered at the scale of the full beam length however, the axial distributions are predominantly uniform or linearly varying. This behaviour differs from the classical response of vibrating beams subjected to distributed mass and loading, for which sinusoidal curvature distributions are typically expected.

It is believed that the observed response arises from the dominance of rotational inertia and hydrodynamic added mass of the rigid floaters at the beam ends, which impose inertia induced end moments. A uniform beam subjected to approximately equal bending moments at both ends, develops a constant curvature over its length, which would lead to the observed uniform strain behaviour for the bending dominated global mode.

For the torsion dominated mode, the beam response is governed by a combination of strong torsional shear deformation and inertia induced end moments acting in the same direction. The torsional component additionally induces warping related axial strains, while the simultaneous action of end moments introduces additional bending effects along the beam length. The interaction of these mechanisms results in an axial strain distribution that changes sign along the beam, reflecting a complex deformation state rather than a purely torsional or purely bending response. Modes 1a and 1b exhibit coupled bending and torsional behaviour of a similar nature, leading to weakly varying but non classical deformation patterns along the beam length.

In plane shear deformation contributes to all investigated global modes and is most pronounced in the torsion dominated mode, where co directional floater rotation induces significant transverse deformation. However, due to segment boundaries, cutouts, and the inability to measure through thickness shear strains at the beam surfaces, this contribution cannot be reliably quantified experimentally. It is therefore not included in the quantitative analysis, although it is recognised as a contributing mechanism in the torsion dominated response.

3.4.5. Local through-thickness strain effects

Figure 11 presents the predicted longitudinal strain distributions at the bottom, mid, and top surfaces of Beam BC in Mode 1b. This beam experiences combined bending and torsion. The same nodal locations are used as in the preceding global deformation plots. The vertical dashed lines indicate the midspan positions of the cutouts. It can be observed that, while the overall strain amplitude of all three representations is governed by global bending, significant local deviations occur in the vicinity of the openings.

In particular, relative to the mid-surface strain, the longitudinal strain at the top and bottom surfaces reverses sign within individual cutout regions. This behaviour is observed in all beams under torsional deformation. It is believed the presence of cutouts induces local cross-sectional distortion and warping, causing the remaining surfaces above and below the openings to deform in a plate-like manner under combined bending and torsion. These mechanisms together produce the strong local strain gradients observed.

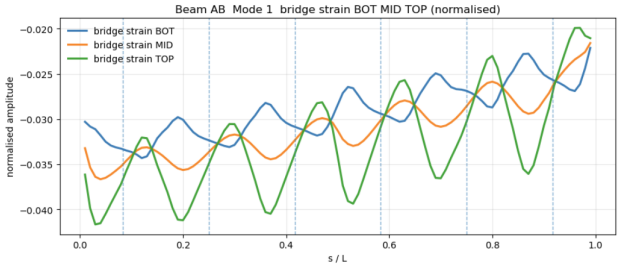

Figure 11: Local strain distributions along Beam BC in Mode 1b.

Mode	Beam	Behaviour	Axial strain dist.	Phase	max $\lvert\theta\rvert$ [rad]	max $\lvert\varepsilon_x\rvert$ [-]	max $\lvert\phi\rvert$ [rad]
1	AB	T. dominated	Decaying	In	0.36	2.1×10^{-2}	5.3
1	BC	B. dominated	Uniform	In	0.72	5.0×10^{-2}	3.3
1	CA	B. dominated	Uniform	Out	0.77	6.4×10^{-2}	2.0
2	AB	B. dominated	Uniform	Out	0.80	6.7×10^{-2}	0.83
2	BC	Coupled B.&T.	Weakly decaying	In	0.65	4.2×10^{-2}	4.3
2	CA	Coupled B.&T.	Weakly decaying	In	0.50	3.3×10^{-2}	5.1
3	AB	B. dominated	Uniform	In	0.81	7.1×10^{-2}	0.44
3	BC	B. dominated	Uniform	In	0.81	7.1×10^{-2}	0.44
3	CA	B. dominated	Uniform	In	0.81	7.1×10^{-2}	0.46
4	AB	T. dominated	Sign changing	In	0.83	1.25×10^{-1}	9.9
4	BC	T. dominated	Sign changing	In	0.84	1.25×10^{-1}	9.8
4	CA	T. dominated	Sign changing	In	0.82	1.21×10^{-1}	9.8

Table 5: Qualitative and quantitative summary of beam level deformation behaviour for the four global modes.

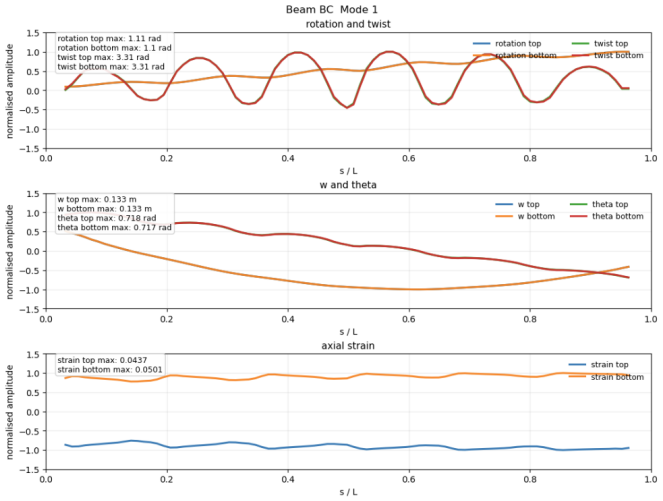

(a) Mode 1, Beam BC

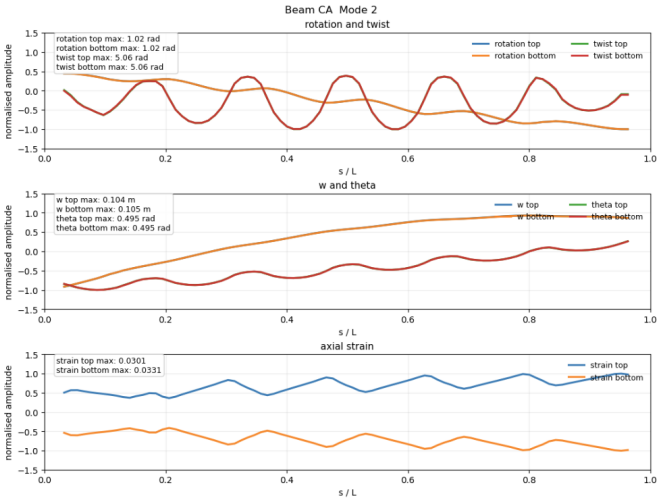

(b) Mode 2, Beam CA

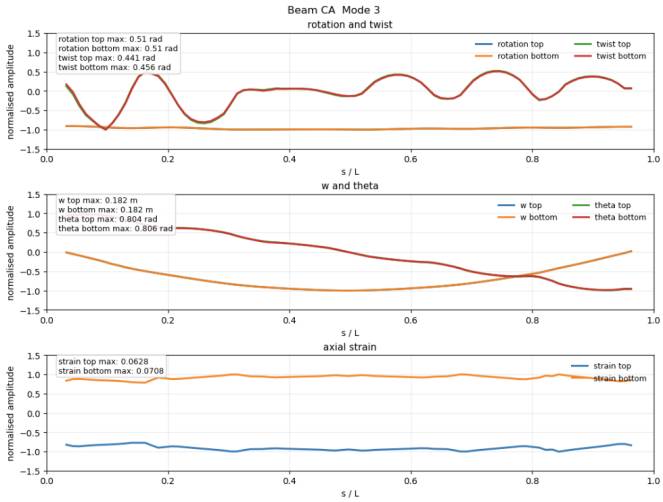

(c) Mode 3, Beam CA

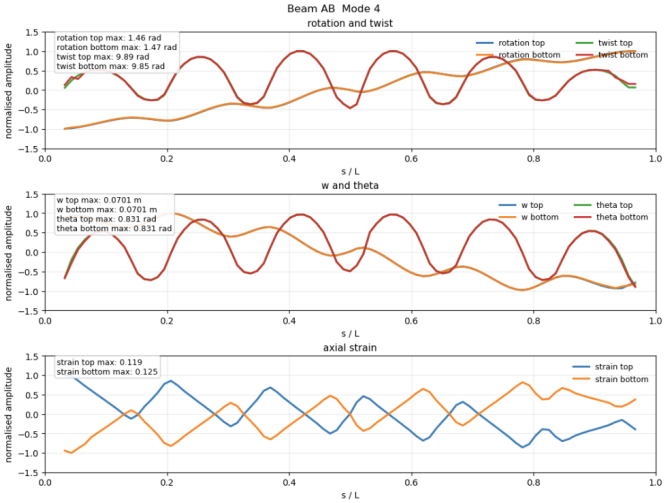

(d) Mode 4, Beam AB

Figure 12: Representative beam deformation fields. Top: twist (red) and rotation (orange), middle: transverse deflection (w, orange) and slope (θ, red), bottom: predicted axial strain top (orange) and bottom (blue) flanges.

4. Detailed design and Construction

This chapter presents the translation of the optimised numerical design into a manufacturable and physically assembled model. First, the beam segmentation strategy and joint geometry are described in Section 4.1, followed by the beam production and assembly procedure in Section 4.2. The floater construction, including material selection and structural detailing, is outlined in Section 4.3, after which the Beam–Floater Interface design is discussed in Section 4.4.

Finally, deviations observed during construction are quantified and incorporated into the numerical representation in Section 4.5, leading to the updated modal predictions presented in Section 4.6.

4.1. Beam segment design

The segmentation strategy required repeatable and mechanically robust connections capable of transferring bending and torsional loads in a manner approaching continuous beam behaviour. To this end, snap fit joints in combination with a two component structural epoxy adhesive (Araldite 2011, Huntsman) were selected.

This combined approach was intended to preserve geometric continuity across segment interfaces and to promote load transfer through distributed surface contact, thereby reducing the risk of joint induced compliance. The adhesive was selected based on its reported stiffness characteristics, which are comparable to Tough2000, and its suitability for thin bond line applications. When applied in combination with a close fitting snap fit geometry, the bonded interface was expected to approximate a continuous material transition while minimising uncertainty in joint stiffness.

The resulting beam layout is depicted in Figure 13. Each beam consists of three distinct segment types. To replicate the clamped outer edge modelling assumption in the physical model, the outer segments, depicted in red, include solid end caps with a thickness of 10 mm. The end caps act as locally rigid extensions of the beam, providing a stiff and well defined interface for the bolted connections to the BFI's that connect the beams to the floaters. A horizontal intrusion profile was integrated into these caps to facilitate fastening.

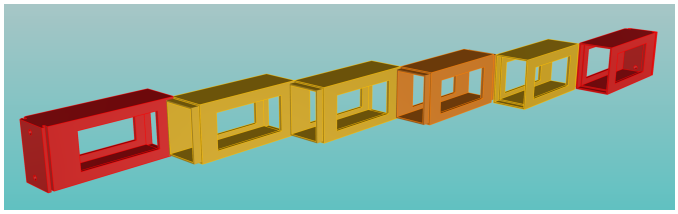

Figure 13: Full beam representation.

The internal beam sections comprise three male–female (MF) segments, shown in dark yellow, and one male–male (MM) segment, shown in orange, with the MM segment positioned at the fourth location along each beam. This configuration ensured as many extrusions as possible are located in outward facing direction, thereby reducing geometric variability between beam sections.

To achieve a close and reliable fit, a set of dedicated test specimens were manufactured to perform assembly trials and explore joint configurations that balance ease of assembly with sufficient stiffness. The snap fit geometry was parametrised by the extrusion and intrusion length L_i, the nominal extrusion and intrusion angle α, and the fillet radius R_f. In addition, a geometric offset Δ was applied to the extrusions only, effectively over-sizing the mating features to ensure reliable engagement while reducing sensitivity to minor surface imperfections.

Based on observations from these specimen, a uniform geometric offset of $\Delta = 0.05$ mm was adopted, no extrusion angle was applied, and the intrusion length was selected as $L_i = 10$ mm in an attempt to maximise frictional engagement and bonding surface while limiting the length of the connection region. The final joint geometry is summarised in Table 6.

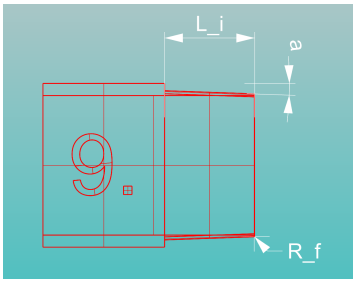

Figure 14: Snap fit extrusion geometry.

Table 6: Final snap fit connection geometry.

Param.	Value
L_i	10 mm
Δ	0.05 mm
α	0°
R_f	0.05 mm

Table 7: Key material properties of Araldite 2011 epoxy adhesive.

Property	Value
Adhesive type	Two component epoxy
Recommended bond line thickness	0.05–0.10 mm
Lap shear strength at 23°C	> 19 MPa
Flexural modulus (ISO 178)	1.9 GPa
Flexural strength (ISO 178)	60 MPa

4.2. Beam production and assembly

This section describes the manufacturing and assembly procedure of the beam segments. First, the adopted additive manufacturing settings and post processing steps are outlined. Subsequently, the surface preparation, bonding procedure, and curing strategy are detailed, with specific attention to geometric tolerances, joint closure behaviour, and their potential influence on structural continuity.

4.2.1. Additive manufacturing settings

The highest available resolution settings were used for all components manufactured using the Form 4 printer during this research. This choice was made to minimise printing induced geometric variability and to promote consistent material behaviour across all specimens and structural components. As a result, all parts were printed with a layer height and in plane resolution of 50 μm.

To further limit systematic variability, all SLA printed parts were oriented with their longitudinal axis aligned with the build direction. This orientation was applied consistently in order to avoid variations associated with possible orientation dependent printing and curing effects.

All SLA printed parts were subsequently post cured in accordance with the manufacturer's specifications (120 minutes 80 $^{\circ}C$). Post curing was performed to increase material stiffness and to reduce variability arising from differences in curing degree, both between individual parts and within more complex geometries.

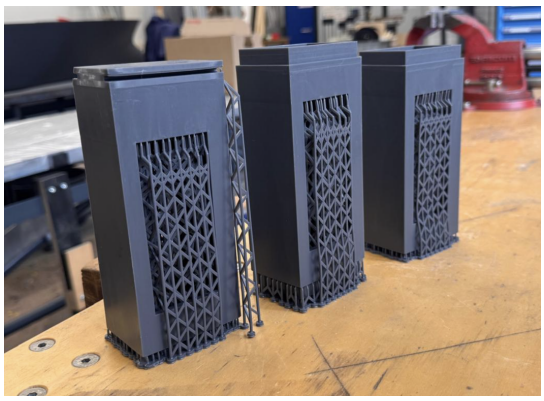

Figure 15: Printed beam segments

4.2.2. Beam assembly

The printed beam segments after initial cleaning and curing, but prior to any assembly preparation, are shown in Figure 15. The support structures visible in this figure were removed by careful clipping using pliers, as the material was found to be sensitive to surface scratching. During this stage, Tough2000 was also observed to be susceptible to aggressive cleaning agents. Acetone was therefore avoided due to its tendency to chemically abrade the surface, and isopropyl alcohol was adopted as the primary cleaning agent.

All mating surfaces were prepared using a consistent procedure. Surfaces were first cleaned with isopropyl alcohol to remove residual contaminants, followed by light abrasion with 320 grit sandpaper to promote adhesion and remove minor surface irregularities. Local edge features were gently filed to correct for non planar surfaces resulting from support contacts during printing. After abrasion, all surfaces were cleaned again using isopropyl alcohol soaked wipes, with residual dust in corners and recesses removed using cotton tipped applicators. Figure 16 illustrates the surface preparation of a representative beam segment prior to assembly.

After surface preparation, a uniform layer of adhesive was applied to the extruded features, after which the corresponding intrusions were aligned and gently tapped into position. Adhesive overflow was controlled by applying tape around the joint region, ensuring that the adhesive remained confined to the intended bonding surfaces while allowing any remaining gaps to be filled.

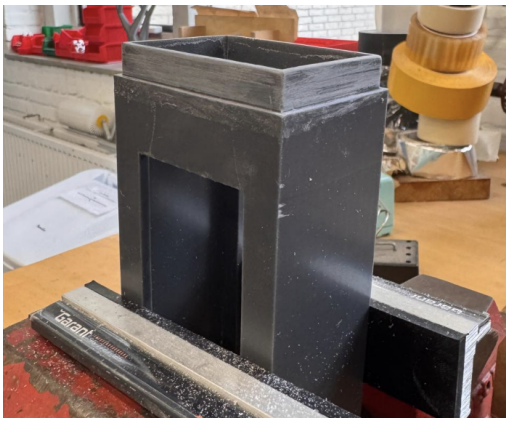

Figure 16: Snap fit extrusion during preparation.

After assembly, each beam was placed on a workbench between two rigidly clamped straight metal profiles. An additional metal profile was positioned on top of the beam and lightly clamped to enforce straightness during curing, as illustrated in Figure 17.

During this process, it was observed that despite careful design of the snap fit geometry, measurements of the in and extruded surfaces occasionally revealed minor irregularities on the order of $\leq$ 0.2 mm. These small deviations affected the ease with which individual segments could be joined. Repeated joining and separation of test segments resulted in slight abrasion near the corner regions, indicating localized contact and bonding at these locations.

Additionally, minor variations in joint closure were observed between individual segment interfaces. While some joints exhibited no visible gaps, others showed small separations ($\leq$ 1.0 mm). These differences are attributed to local variability introduced during surface preparation, such as slight over abrasion of the outer intrusion edges. After final assembly, however, all three beams exhibited equal overall length, indicating that these local variations did not lead to meaningful differences in effective beam length.

Figure 17: Indicative beam assembly and curing procedure.

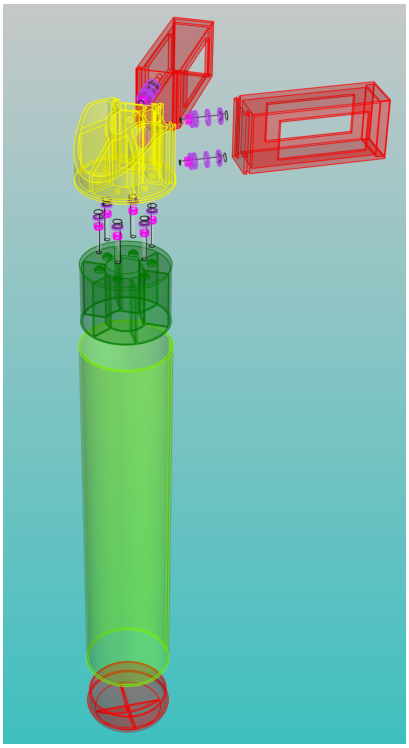

Figure 18: Exploded view of the floater assembly.

4.3. Floater construction

An exploded view of the floater construction is shown in Figure 18, illustrating the component hierarchy. In addition to stiffness at the beam–floater interface (yellow), the floater design was governed by requirements related to overall platform weight, water tightness, modularity, and reliable load transfer. To satisfy these requirements, each floater was constructed from a set of dedicated components, comprising a bottom closure (red), a PMMA shell (light green) and the top insert (dark green). Joining was achieved with the use of bonding agent and fastening materials.

4.3.1. Additive manufacturing PLA-CF

The Tough2000 additive manufacturing strategy described in Section 4.2.1 was applied during production of the beam segments. In addition to the SLA printed beam components, FDM printing using Polyactic Acid Carbon Fibre (PLA-CF) on a Bambu P1S printer was employed for all remaining non-beam components. This combined manufacturing approach was adopted to reduce production lead times and to allow parallel fabrication of components with different functional requirements. PLA-CF was selected for non-beam components due to its increased in plane stiffness over regular PLA and Tough2000, the material properties are presented in Table 8.

Table 8: Manufacturer specified mechanical properties of PLA CF used for non beam components.

Property	Value
Density	1.22 g/cm^3
Young's modulus (through thickness)	2.2 GPa
Young's modulus (in plane)	4.0 GPa

4.3.2. Floater skin selection

To ensure that the rigid floater modelling assumption introduced in Section 1.4 remains valid during the experimental campaign, the floater skins were required to exhibit sufficiently high stiffness. Two criteria were considered: separation from the global platform modes and separation from the characteristic slamming timescale. The lowest local floater deformation frequency was targeted to exceed the highest global platform mode by approximately one order of magnitude and to remain well above the estimated model scale slamming frequency. The detailed assessment procedure is presented in Appendix C. As outlined, these requirements were not easily achieved within the imposed geometric and mass constraints of the scaled model. Aluminium sections were found to be excessively heavy, while composite alternatives were not readily available in the required dimensions.

A commercially available PMMA extrusion with a wall thickness of 3 mm was selected as a suitable compromise between stiffness and mass. The manufacturer specifies a Young's modulus of 3.3 GPa and a Poisson ratio of 0.375.

Numerical modal analyses indicate that, when the Top Insert is included, the lowest local floater deformation modes occur at frequencies an order of magnitude higher the global platform modes and also above the estimated slamming frequency range. As discussed in Appendix C, these estimates are based on dry analyses and should therefore be reassessed prior to the slamming experiments. Nevertheless, given that PMMA represents the stiffest practically available and manufacturable option within the imposed constraints, its selection was considered acceptable.

4.3.3. Top insert assembly

The connection between the Beam–Floater Interface and the floater top was realised through the internal Top Insert bonded to the PMMA shell, as illustrated in Figure 19. The insert was designed to provide a stiff and well defined load transfer path between the beam floater interface and the floater shell, while simultaneously increasing the local stiffness of the floater skin.

The insert was manufactured from PLA-CF and incorporated an internally stiffened geometry to prevent local deformations. It extended 75 mm into the PMMA shell, a length selected to satisfy the minimum frequency requirements for floater skin deformation while simultaneously providing sufficient interface area for effective load transfer and reliable adhesive bonding.

A bolted connection was adopted between the BFI and the Top Insert to enable modular assembly and disassembly of the model. The upper surface of the insert was designed as a solid 5 mm thick PLA-CF plate with integrated hexagonal recesses for embedded steel nuts, as depicted in Figure 19b. When assembled, the bolts clamp the Beam–Floater Interface against the insert and PMMA shell. The hexagonal bolt spacing and bolt diameter were designed such that its bending stiffness exceeded that of the surrounding floater skin to provide a con-

(a) Stiffened top connection insert bonded inside the PMMA shell.

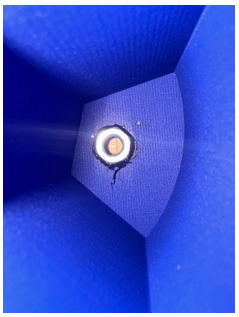

(b) steel nut used for the bolted beam connection.

Figure 19: Top connection assembly at the beam–floater interface.

Figure 20: Assembled floater bottom closures.

servative strength requirement. Based on this requirement, M6 fasteners were selected and distributed evenly around the insert circumference with a 65 mm spacing.

4.3.4. Bottom closure and watertight sealing

The bottom of each floater was closed using an insert manufactured from PLA-CF, as shown in Figure 20. This component was designed to reproduce the curved geometry of the full scale floater bottom while providing sufficient stiffness to prevent deformation under loading. To this end, the insert incorporated an internally stiffened structure.

An external cylindrical extrusion with a height of 20 mm was integrated into the bottom insert to provide sufficient bonding length with the PMMA floater shell. Multiple coats of epoxy were applied to the insert to seal the material and to ensure water tightness of the printed component. Prior to assembly, the bonding surfaces were lightly abraded to promote adhesion. The insert was subsequently positioned inside the PMMA tube using a sealant as the primary bonding and sealing agent. To further enhance the watertight seal at the interface between the PMMA shell and the bottom insert, a circumferential bead of sealant was applied around the lower edge of the tube. A small chamfer was introduced at the top edge of the bottom insert to facilitate uniform distribution of the sealant and to reduce the risk of void formation during assembly.

4.4. Beam–floater interface design

A critical component of the floater assembly is the Beam–Floater Interface (BFI), highlighted in yellow in Figure 18. As demonstrated in Section 3.4.4, bending moments at the beam ends dominate the local structural response. Consequently, the global behaviour of the structure is highly sensitive to the rigidity of the BFI.

The interface was required to fulfil three primary functions: to provide a connection point for the 10 mm thick endcaps of the outer beams, to enable fastening of the BFI to the top insert, and to ensure a rigid load path between the beams and the floaters. The latter requirement was essential to avoid introducing unintended compliance that could alter the targeted global dynamic behaviour.

Given strict mass constraints at model scale, the intended stiffness could not be achieved through over-dimensioning alone. A weight efficient circular PLA–CF printed interface was therefore developed, reusing the inner ring and stiffener concept adopted for the top insert.

To design the BFI, a simplified numerical representation of the connection was developed in PyMAPDL to evaluate its stiffness under conservative static loading. A subsequent parametric study was performed to optimise the interface thickness and material removal strategy. The modelling approach and associated sensitivity analyses are described in Appendix C.4.

The final design was validated through both numerical assessment and physical test prints. A partially assembled beam and BFI specimen was subjected to considerable loading. During testing, visible bending deformation was observed in the beam segments, while no visible deformation occurred in the BFI, indicating that the interface behaves effectively as a rigid connection. The refined representation was subsequently incorporated into the global numerical model, as described in the following section.

4.5. Construction based prediction alteration

During construction of the model, it became apparent that the as-built platform mass exceeded the scaled target value. To account for this deviation and ensure consistency between the physical model and the numerical representation, the global mass properties of the structure were reassessed and incorporated into the numerical model.

4.5.1. As-built mass and density assessment

Geometric measurements were performed using a caliper to assess printing accuracy. For components manufactured from Tough2000, reliable measurements proved challenging due to surface irregularities resulting from support removal and difficult accessibility of certain regions. The mean measured segment thicknesses difference from as designed thicknesses was 0.06 mm, this slightly surpasses the advertised resolution of 0.05 mm. All components were subsequently weighed and compared against mass predictions obtained from CAD volumes and manufacturer specified material densities. A summary of the predicted and measured masses is provided in Table 9.

From the observed mass and the CAD defined volumes, the observed effective material densities presented in Table 10 were defined. Tough2000 showed to be consistently heavier

than predicted. Especially the outer beam segments exhibited slightly higher effective densities, in some cases approaching 1.24 g cm^{-3}. These deviations are attributed primarily to small but systematic differences between the nominal CAD geometry and the as-printed geometry, in particular, small absolute increases in wall thickness in the outer caps. The PMMA skin components were consistently heavier than predicted based on manufacturer specified properties, whereas the PLA–CF components were lighter than predicted.

The scaled target mass of the model was 5258.3 g. As shown in Table 9, the as designed mass of 5619.7 g already exceeded this target. The as constructed mass of 5898.2 g further increased this deviation. Although it is undesirable that the design mass exceeded the target, each component fulfils a structural function that requires a minimum level of stiffness and therefore mass. The additional increase in constructed mass is partially attributed to higher than anticipated material densities for Tough 2000 and PMMA. A significant contribution however also resulted from redesigns of the fastening components within the BFI. The initial mass estimate of 120.6 g was based on a simplified early design. Based on observations during testing, it was decided to increase the amount of fastening material to ensure sufficient stiffness, accepting the associated mass penalty.

Table 9: Measured mass of major structural components in the as built scaled model.

Component	Predicted [g]	Observed [g]
Beams	2301.4	2337.5
PMMA floaters	1770.7	1891.9
BFI's	671.6	647.2
Top Insert	442.3	379.9
Floater Bottoms	214.1	205.2
Fastening material	120.6	391.6
Instrumentation allowance	100	45.0
Total mass	5619.7	5898.2

4.6. Design based prediction alteration

The optimisation predictions presented in Section 3.4 are adjusted to account for these observed mass deviations. First, experimentally measured material densities were adopted in place of the manufacturer specified values. In addition, the mass and inertia of individual components were represented explicitly using discrete MASS21 elements located at their respective volumetric centres. These elements were coupled to the surrounding structure through RBE3 constraint equations, ensuring correct load transfer without introducing artificial stiffness.

The top inserts were modelled using CERIG constraints connecting the floater skin and the bottom plate of the Beam–Floater Interface. In this manner, the insert and bottom plate of the Beam–Floater Interface were represented as an effectively rigid region. To avoid double mass allocation, the BFI elements were assigned zero density. Furthermore, the BFI geometry introduced in Section 4.4 was incorporated to reflect the as built configuration.

Table 10: Measured and manufacturer specified densities.

Component	Observed [g cm^{-3}]	manuf. specified [g cm^{-3}]
Tough 2000	1.22	1.20
PMMA	1.28	1.18
PLA-CF	1.15	1.20

The updated total mass of 5898.2 g was subsequently used to determine a revised static draft. This revised draft formed the basis for generating an updated floater surface mesh for the boundary element analysis, from which a corrected added mass representation was obtained for the dynamic modal predictions.

4.6.1. Added mass error identification

During this process, an error was identified in the original floater mesh used in Section 3.1, which had resulted in incorrect added mass values being supplied to the optimiser. Consequently, earlier numerical predictions were no longer directly comparable to the target scaled modal properties. The target scaled natural frequencies presented in Section 2.1 are listed in the first row of Table 11. The second row presents the frequencies obtained from the numerical optimiser reported in Section 3.4, these values are based on the incorrect added mass representation.

The third row presents the predicted natural frequencies obtained using the optimisation based structural model with the corrected implementation of added mass. As shown, the revised added mass formulation has a substantial influence on the predicted frequencies. These results were computed using the target model mass and draft as input parameters.

The subsequent rows illustrate the individual influence of each modelling refinement on the updated frequency predictions. It is evident that the inclusion of the additional model weight, together with the corresponding draft correction, has the most significant effect. The increased draft leads to a higher added mass contribution, thereby reducing the natural frequencies. The incorporation of additional inertia through the use of higher effective densities and MASS21 elements results in a further reduction. Finally, the non rigid representation of the BFI introduces an additional decrease in the predicted frequencies. The frequencies depicted in the fourth row are the predictions obtained after incorporating all modelling refinements.

Table 11: Influence of successive modelling refinements on predicted wet natural frequencies [Hz]

	Mode 1a	Mode 1b	Mode 2	Mode 3
target	10.60	10.60	12.52	17.54
optimiser	9.51	9.53	13.24	17.67
Added mass corr.	11.44	11.46	16.14	18.29
ρ & MASS21	-0.19	-0.20	-0.19	-0.21
Draft revision	-0.56	-0.56	-0.88	-0.65
non–rigid BFI	-0.08	-0.08	-0.13	-0.02
final model	10.60	10.60	14.93	17.41

5. Experimental Testing

This chapter presents the experimental validation of the constructed model. First, the instrumentation layout and measurement strategy are described in Section 5.1. The dry dynamic testing procedure is then outlined in Section 5.2, followed by the wet experimental configuration and testing protocol in Section 5.3. Finally, the static experimental procedure used for material characterisation is detailed in Section 5.4.

5.1. Instrumentation

The model was instrumented with accelerometers and strain gauges. The overall instrumentation layout is shown in Figure 21, where the global x and y axes are indicated in red and green, respectively. A total of twelve single-axis accelerometers with a mean nominal sensitivity of 1.120 $\mathrm{mV/(m/s^2)}$ were installed on the model. Accelerometer locations are indicated by coloured circular markers, with green, yellow, and cyan denoting measurements in the global x, y, and z directions, respectively.

Strain gauge locations are indicated by square markers, with red representing axial strain gauges and dark blue representing torsional strain gauges. The axial strain gauges were HBM 1 LY16–3–350 gauges with a nominal resistance of 350 Ω and a nominal gauge factor of 2.09. These gauges were configured in half Wheatstone bridge arrangements. This configuration exploits the equal magnitude and opposite sign of bending strain at the top and bottom beam surfaces, thereby increasing measurement sensitivity while suppressing uniform axial strain contributions and thermal effects.

Torsional strain was measured using HBM K 216.93 2217 strain gauge rosettes with a $(-45°, +45°)$ orientation. These rosettes were configured in full Wheatstone bridge arrangements to accurately measure the torsional shear strains present in the beams.

All strain gauges were applied following the manufacturer prescribed surface preparation procedure, including surface abrasion and cleaning. A three dimensional printed alignment template was used to ensure correct gauge orientation during installation, as misalignment could significantly affect the measured strain components.

All instrumentation cables were routed internally through the beam structure wherever possible. The cables were fixed to the internal beam surfaces using a minimal amount of flexible adhesive to prevent relative motion while avoiding the introduction of additional stiffness. Sufficient slack was provided to prevent cable tension. The cables exited the structure at the outer segment cutouts and were bundled into a single cable harness, which was routed away from the model during testing.

All instruments were electrically balanced and shunted to ensure zero output under stationary conditions. The data acquisition system was configured to sample all channels simultaneously at a fixed sampling frequency of 6000 Hz. The strain gauge bridges were excited using a constant excitation voltage of 5 V. In total, 24 active measurement channels were employed to capture the global dynamic response of the platform.

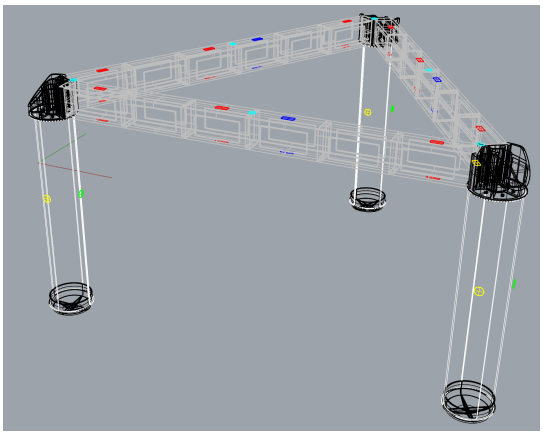

Figure 21: Instrumentation layout.

5.1.1. Accelerometer placement rationale

The global flexible modes are primarily characterised by the orientation of the horizontal rotation axes of the individual floaters. To capture this behaviour, six accelerometers were mounted on the vertical outer walls of the floaters. In dry conditions, the sensors were positioned near the bottom of each floater, whereas in wet conditions they were installed at a height of 5 cm above the still waterline. These sensors measured horizontal accelerations, providing an indirect representation of floater rotations relative to the beam end assemblies.

In addition to floater motion, the dynamic response of the connecting beams and their relative phase relationships are essential indicators of the global modal behaviour. Therefore, six additional accelerometers were installed along the beams at the Beam–Floater Interfaces and at mid span. These sensors were oriented in the global z direction to capture the vertical beam response.

5.1.2. Strain gauge placement rationale

As discussed in Section 3.4, narrow strips along the top and bottom surfaces of each beam provide the most suitable locations for extracting strain measurements associated with global beam deformation. To reduce the influence of the local through thickness effects discussed in Section 3.4.5, strain gauges were positioned at the midpoints of the cutouts along the beam length, resulting in six potential measurement segments per beam.

The final strain gauge configuration was guided by the predicted axial strain and twist distributions obtained from the numerical modal analysis in Section 3.4. Various combinations of axial and shear gauges were evaluated using the Modal Assurance Criterion (MAC), which quantifies the similarity between modes and therefore provides an indication of the potential risk of modal aliasing.

The MAC values were computed by inserting the predicted axial and shear strain distributions into Equation 4. It was observed that, due to the complexity and relative phase differences between beams for different modes, the risk of modal aliasing was already significantly reduced by applying one axial and one shear gauge on each beam, independent of the specific segment

location.

Notable exceptions were Modes 1a and 1b, as well as Modes 4a and 4b. These modes exhibit very similar deformation patterns, resulting in consistently high MAC values between them and therefore a higher risk of aliasing. Even when both axial and shear gauges were applied on all segments, the MAC values between these mode pairs did not reduce below approximately 0.72.

Based on these observations, axial strain gauges were installed on Segments 1, 4, and 6. These locations are indicated by vertical lines with green crosses in Figures 22 and 23, where examples of the resulting linearised predicted strain distributions are also shown.

The predicted torsional strain distributions exhibit more complex, mode dependent spatial variation and are generally of secondary importance in characterising the global modal behaviour. Consequently, torsional strain measurements were not treated as a primary diagnostic quantity. A single torsional strain gauge was therefore installed on Segment 3 of each beam. These measurements primarily serve as a consistency check, providing confirmation of the deformation characteristics inferred from the axial strain observations.

The MAC matrix for the wet configuration corresponding to the selected strain gauge configuration is presented in Table 12.

$$\mathrm{MAC}(\phi_i, \phi_j) = \frac{\left|\phi_i^{\mathrm{T}} \phi_j\right|^2}{\left(\phi_i^{\mathrm{T}} \phi_i\right)\left(\phi_j^{\mathrm{T}} \phi_j\right)} \tag{4}$$

Table 12: MAC values between numerical modes in wet conditions.

Mode	1a	1b	2	3	4b	4a
1a	1.000	.7504	.0000	.0000	.0096	.0139
1b	0.7504	1.000	.0001	.0002	.0136	.0097
2	.0000	.0001	1.000	.0072	.0002	.0002
3	.0000	.0002	.0072	1.000	.0006	.0002
4a	.0096	.0136	.0002	.0006	1.000	.7489
4b	.0139	.0097	.0002	.0002	.7489	1.000

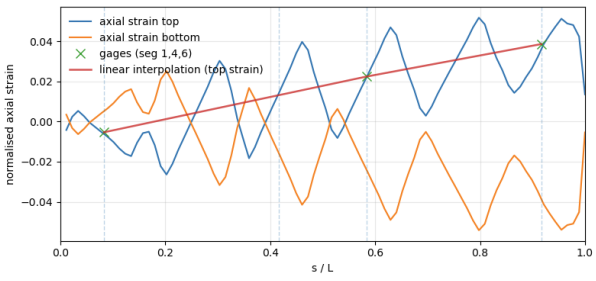

Figure 22: Predicted axial strain distribution beam CA, mode 1b.

5.1.3. *Excitation system*

The specimens were excited using a modal shaker (Dewesoft DS MS 100), applying a sine sweep excitation. The excitation force was measured using a force sensor (Dytran 1051V1)

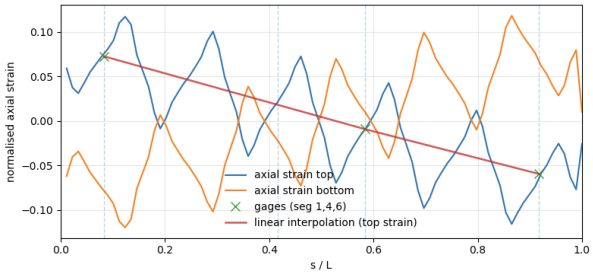

Figure 23: Predicted axial strain distribution beam BC, mode 3

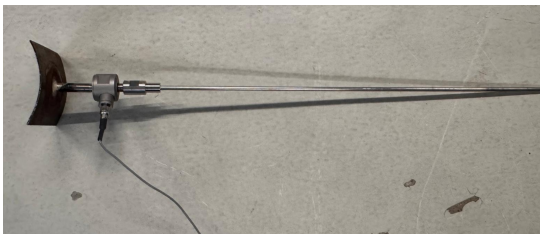

Figure 24: Dytran 1051V1 force sensor with fabricated connection piece

mounted in line with the shaker stinger, with a nominal sensitivity of 112.4 mV/N. The stinger and force sensor assembly is shown in Figure 24.

To enable coherent force measurements without drilling into the PMMA floater shells, which was considered prone to cracking, a dedicated connection piece was fabricated. This component consisted of a 4×4 cm square plate, bent to conform to the curvature of the floater surface, with an attached tapped extrusion to allow direct connection to the force sensor. The connection piece was attached to the floater skin using double sided tape, resulting in a strong and non intrusive attachment method.

The excitation amplitude was adjusted such that the measured force response remained consistent, with peak force levels between 3 and 5 N over the investigated frequency range.

5.2. *Dry dynamic experimental set-up & procedure*

The dry experimental set up is shown in Figure 25. The model was suspended from linear springs at each corner, providing an approximately free–free boundary condition. The springs had a nominal stiffness of 25 N/m, which was verified through numerical simulations to be sufficiently low such that their influence on the global modal properties of the structure was negligible. To accommodate the relatively large spring lengths required, a triangular support tower constructed from aluminium extrusions was used to attach the springs above the model.

During the dry tests, the modal shaker was positioned on the laboratory floor, resulting in an excitation connection point located approximately 7 cm above the bottom of the floater.

Instrumentation cables were routed upward and away from the model to minimise their influence on the dynamic response. The cable harness was guided vertically above the geometric centre of the platform and suspended such that the cables did not introduce additional stiffness or mass. The adequacy of this

Figure 25: Dry experimental set up

arrangement was verified by applying small rigid body excitations, which confirmed that the platform was free to undergo heave and pitch motions while the cable bundle remained effectively stationary.

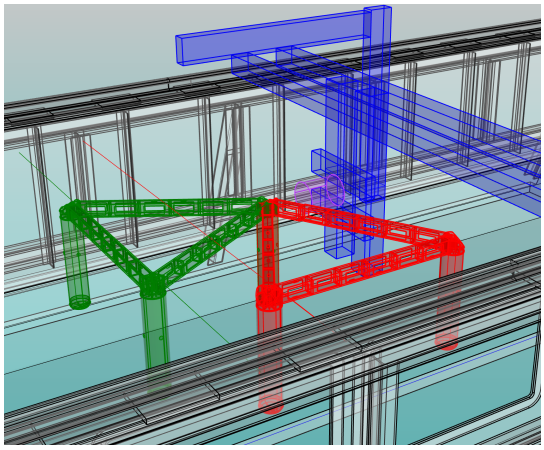

Figure 26: Wet experimental set up in the towing tank.

A roving excitation strategy was adopted for the dry tests in order to assess sensitivity to local boundary conditions associated with a single shaker location. Each floater was excited sequentially in two orthogonal horizontal directions, selected to predominantly excite torsional and bending dominated global responses, respectively. Based on the geometric definition, the two excitation directions are referred to as the radial and tangential directions.

The radial direction is defined as being parallel to the line connecting the centre of the triangular platform to the excited floater and predominantly excites bending dominated global responses. The tangential direction is defined as being perpendicular to this line and predominantly excites torsion dominated global responses.

This resulted in six distinct excitation configurations. The complete excitation sequence was repeated five times to assess influence of run specific variability. The excitation frequency range was limited to 0 to 100 Hz. This range was selected based on numerical predictions indicating that higher order modes are increasingly local in nature and weakly excited through floater motion.

5.3. Wet dynamic experimental set-up & procedure

A diagram of the experimental configurations used for the wet modal tests is shown in Figure 26. The green model and fastening lines represent the radial test. The red model and fastening lines represent the tangential tests. Aluminium profiles, represented in blue, were placed across the width of the towing tank to provide a rigid support for the modal shaker, represented in purple.

This arrangement allowed the shaker to be positioned as close as possible to the waterline, for maximal modal excitation, while maintaining a fixed and well defined boundary condition. The vertical position of the excitation connection point relative to the floater was fixed at 16.3 cm above the still waterline.

The tank width was sufficiently large to allow the shaker to be rigidly fixed at approximately two thirds of the tank width, while the platform itself was repositioned to realise different excitation configurations.

To maintain the platform at a fixed mean position during the wet tests, two vertical flexible springs with a nominal stiffness of 25 N/m were applied using tensioned strings. These springs were oriented perpendicular to the stinger direction and were attached either to the two floaters furthest from the shaker for radial tests, or to the single floater furthest from the shaker for tangential tests. By carefully adjusting the string lengths, the springs were engaged with minimal pre tension while still preventing drift of the platform during the measurements, thereby limiting their influence on the dynamic response.

Repositioning the platform between individual excitation configurations was considered impractical, as the associated disturbances to the water surface and the subsequent settling time would have significantly increased the overall testing duration. Instead, the shaker was repositioned once for each excitation configuration, and multiple measurements were performed without altering the boundary conditions. A total of seven runs were conducted. The excitation frequency range for the wet tests was limited to 0 to 70 Hz.

Images of the radial and tangential excitation tests are presented in Figures 27 and 28.

5.4. Static experimental procedure

To quantify the static material properties of Tough 2000, additional tests were conducted to extract the effective flexural modulus. Three structural configurations were investigated.

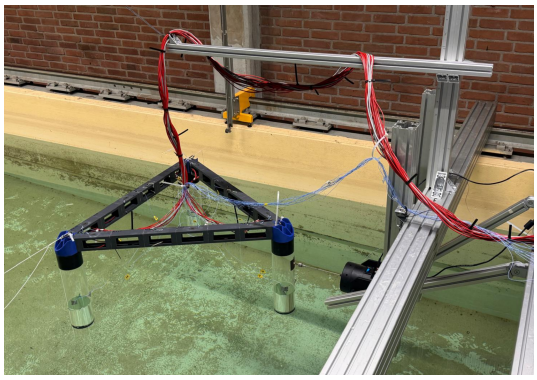

Figure 27: Wet radial excitation test configuration.

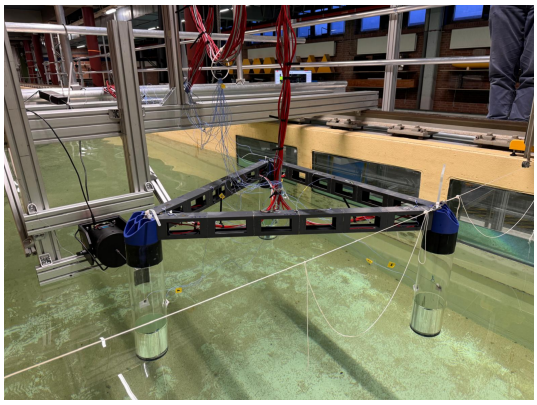

Figure 28: Wet tangential excitation test configuration.

The first configuration consisted of the fully assembled model, representing clamped–clamped boundary conditions (CC). This setup is shown in Figure 29.

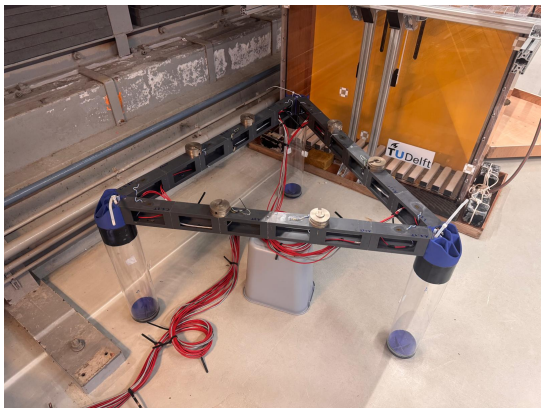

Figure 29: Assembled (CC) static test configuration.

Additional configurations included a clamped–free (CF) setup, depicted in Figure 30, in which the 10 mm thick outer endcap of the beam was rigidly fastened to an aluminium extrusion using the same bolt holes as for fastening to the Beam–Floater Interface. The opposite end of the beam remained unsupported. The third configuration was the simply supported (SS) setup, where the beams were carefully placed on aluminium extrusions to approximate simple supports.

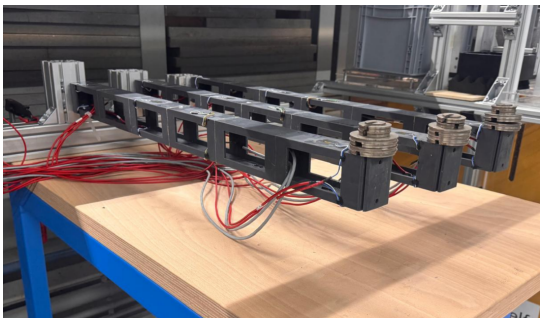

Figure 30: Clamped–Free (CF) static test configuration.

For the CC and SS configurations, two loading positions were considered. In the middle (m) loading configuration, weights were applied at the interface between Segments 3 and 4. In the outer (o) loading configuration, weights were applied at the interfaces between Segments 2–3 and 4–5. To assess potential geometric asymmetry effects, the SS configuration was additionally tested in both flipped (f) and unflipped (uf) orientations, resulting in two separate data subsets.

In the CF configuration, tests were performed in both f and uf orientations, Additionally the test was repeated with the left side of the beam acting as the clamped boundary (r), as well as the right side of the beam as the clamped boundary (l). This resulted in four distinct data subsets for the CF case.

The total number of experimental subsets per configuration is summarised in Table 13.

Table 13: Overview of static test subsets per configuration.

Configuration	Loading position	Orientation	Subsets
CC	m, o	uf	2
SS	m, o	f, uf	4
CF	r, l	f, uf	4

5.4.1. Static loading procedure

The static experiments were conducted through a single continuous, stepwise loading and unloading sequence for each beam. Prior to each test series, all instrumentation was rebalanced. Calibrated steel weights were then applied incrementally to impose the prescribed load levels.

Each load level was maintained for 10 s before proceeding to the next increment. The loading sequence ranged from level 0, corresponding to no applied weight, to level 6, representing the maximum applied weight. Subsequently, the beams were unloaded stepwise back to level 0. This protocol was adopted to minimise excessive creep accumulation in the printed Tough 2000 material.

6. Results

The validation strategy consists of three components. First, a static validation is performed to assess the global flexural stiffness of the model. The resulting flexural modulus is identified through strain–load curve fitting in Section 6.1.

Second, the dynamic properties of the structure are investigated. The modal identification procedure is described in Section 6.2, including frequency–damping clustering, accelerometer based mode extraction, and strain based mode shape reconstruction. These steps ensure objective identification of experimentally observed modes.

The experimentally determined modal properties are compared with numerical predictions in Section 6.3. Further analysis of the results, including beam similarity analysis and local mode identification are presented in Sections 6.4 and 6.5.

6.1. Static flexural modulus identification

During static validation tests, a clear time dependent drift in the strain signals was observed, indicating creep behaviour of the printed Tough 2000 material. This necessitated a dedicated post processing procedure to obtain reliable static strain levels.

The static testing procedure is outlined in Section 5.4. Raw strain time series were segmented into the individual load plateaus using an automated transition detection algorithm. Within each plateau, a linear fit was applied to quantify observed creep. The cumulative creep contribution was then removed from the initial plateau values. Finally, symmetric loading and unloading plateaus were paired. An example of the identification and linearisation is provided in Figure 31. By observing the slope of the linearised segments within this plot, the creep, and the manner in which it affects data can be observed. A detailed description of this procedure is provided in Appendix D.

The creep corrected strain values were plotted as a function of applied weight and compared to FEM predictions. The flexural modulus was treated as a fitting parameter and identified by minimising the difference between experimental and numerical strain load curves. An example is shown in Figure 32, here the coloured lines represent the observed strain-load curves, which are fitted with the black dotted lines representing numerical predictions. A description of the numerical modelling and the complete set of fitted curves for all loading conditions is provided in Appendix D.

The identified flexural modulus values for each segment and configuration are summarised in Table 14. In cases where curve fitting resulted in unrealistically low modulus values (below 0.1 GPa), no value is reported. These cases correspond to outer SS configurations, for which the underlying FEM assumptions are likely not fully representative of the actual boundary conditions. The presented results correspond to the average between flipped and unflipped beam configurations. Although minor differences between flipped and unflipped cases were occasionally observed, these were not systematic and typically remained within 0.1 GPa.

The predicted FEM based strain distributions obtained with $E = 1.9$ GPa, including SHELL181 top, middle and bottom

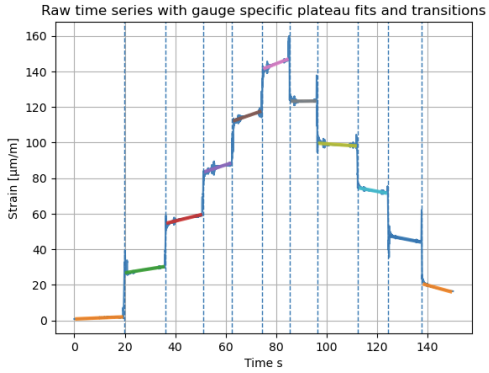

Figure 31: Linearised plateaus during loading steps

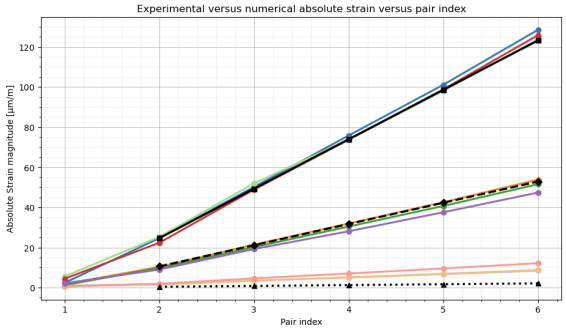

Figure 32: Clamped free configuration, outer loading position.

surface results and a BEAM188 approximation, are compared with the experimental measurements in Figures 33a to 33c. The BEAM188 representation was included to assess the adequacy of a beam formulation relative to the shell based model. For the outer loading cases, the beam based predictions align well with the shell mid surface response in the central segments. For the remaining segments, the agreement varies.

The shell based representations reveal pronounced through thickness strain gradients resulting from the presence of cutouts, consistent with the behaviour discussed in Section 3.4.5. These effects are attributed to shear induced relative cross sectional translation between the closed beam sections, leading to local three node bending patterns in the top and bottom flange surfaces at the cutout locations and consequently strong through thickness strain gradients.

The strain gauge locations, indicated by vertical lines and crosses, coincide with positions where the top, middle, and bottom shell responses intersect, and through-thickness effects are limited. However, these locations also correspond to regions where the strain spatial gradients are largest.

These observations highlight the strong sensitivity of both the numerical and experimental boundary conditions, as well as the assumption of a perfectly continuous stiffness distribution in the manufactured beams. Numerically, a displacement of the predicted strain distribution by only half an element length, approximately 2.2 mm, frequently produces strain variations several times larger than those resulting from a 0.1 GPa change in the assumed elastic modulus. It is therefore considered likely

that this spatial sensitivity resulted in the unreasonably low values for the outer gauges in the SS_o configuration and is a contributor to the variability observed in the fitted flexural modulus values.

A consistent trend nevertheless emerges. Segments subjected to the highest bending moments, namely the middle segments in CC_o and SS_o configurations and the segments closest to the clamped boundary in the CF configuration, systematically yielded the lowest fitted flexural modulus values. In these regions global bending dominates the structural response, while through-thickness effects are either absent or significantly reduced. These values are underlined in Table 14.

Based on the presented strain distributions and the consistency of this trend, these segments are considered to provide the most reliable representation of the true flexural modulus of Tough 2000. From these configurations, a mean flexural modulus of 1.94 GPa was obtained.

Table 14: Identified flexural modulus values in GPa obtained from strain load curve fitting.

	CC		CF		SS	
Segment	m	o	r	l	m	o
A1.1	2.3	2.3	2.4	1.9	–	–
B1.3	2.4	1.8	2.0	2.2	2.1	1.9
B1.1	2.3	2.2	2.0	2.5	–	–
B2.1	2.4	2.5	2.3	2.0	–	–
C2.3	2.4	1.8	2.2	2.4	2.4	2.1
C2.1	2.5	2.7	2.0	2.2	–	–
C1.1	2.5	2.5	2.4	2.0	–	–
A2.3	2.2	1.9	2.2	2.1	2.2	2.0
A2.1	2.4	2.4	2.1	2.5	–	–

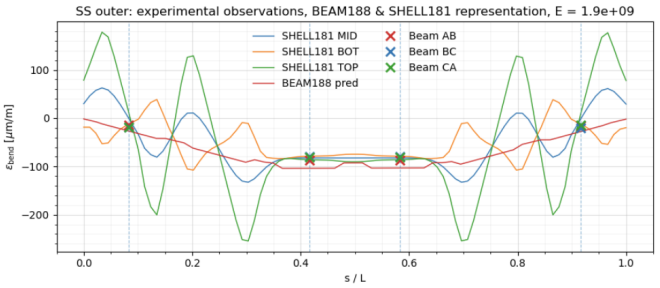

(a) Simply supported configuration, outer loading.

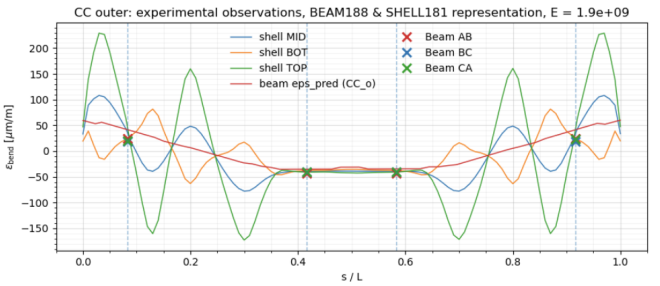

(b) Assembled configuration, outer loading.

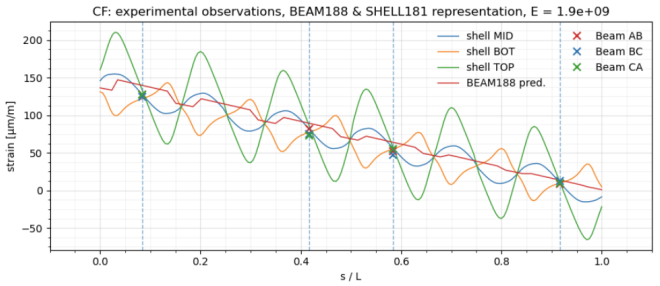

(c) Clamped free configuration.

Figure 33: Comparison between experimental strain distributions and finite element predictions obtained with $E = 1.9$ GPa for representative loading configurations.

6.2. Dynamic data post-processing

The data obtained from all modal experiments were analysed in three consecutive steps. First, a frequency and damping based clustering procedure was applied to objectively group the observed responses into distinct modal clusters, as described in Section 6.2.1. Second, the mode shapes within each cluster were preliminarily verified using the accelerometer data, allowing assessment of whether the experimentally observed modes corresponded to the full scale target modes and the numerically predicted results. This procedure is presented in Section 6.2.2. Finally, the clustered experimental mode shapes were compared directly with the numerical predictions using the strain gauge measurements. This strain based mapping and comparison are detailed in Section 6.2.3.

6.2.1. Frequency and damping based clustering

The modal identification procedure from time series data extracted during experiments is outlined in Appendix A.4. FRF's of both amplitude and local phase were extracted from all 24 measurement channels using the a Fast Fourier Transform algorithm and the H1-estimator. The FRF's were used to compute the Complex Modal Indicator function (CMIF), and identify stable poles corresponding to the natural modes of the model. Observed natural modes were combined across all runs and clustered using a DBSACN clustering algorithm.

It was observed that the modes which were captured differed between runs, the DBSCAN algorithm was therefore applied separately to the radial and tangential excitation data. The results for the four resulting subsets are shown in Figures 34a to 34d. The corresponding cluster statistics, including mean natural frequencies, mean damping ratios, and associated standard deviations, are summarised in Table 15. Detailed close up views of the first three clusters for each configuration are provided in Appendix E.1. To account for differences in clustering behaviour between the dry and wet data sets, the DBSCAN parameters were adjusted slightly for each case, with the selected settings reported in the captions of the respective figures.

Frequency standard deviations remain below 1 Hz, with most values lying between approximately 0.1 and 0.6 Hz, and only isolated higher frequency clusters approaching values close to 0.9 Hz. The standard deviations of the damping ratios are gen-

Table 15: Summary of DBSCAN clustered modal parameters for dry and wet conditions

Cluster	n_p	f_{mean}	f_{std} [Hz]	ζ_{mean}	ζ_{std} [%]
Dry bending					
DB 1	11	22.16	0.16	2.92	0.22
DB 2	11	30.38	0.11	2.46	0.09
DB 3	11	39.55	0.32	3.07	0.26
DB 4	13	70.67	0.19	3.12	0.18
DB 5	12	78.91	0.73	2.84	0.12
Dry torsion					
DT 1	13	21.97	0.44	2.95	0.42
DT 2	12	30.63	0.24	3.34	0.14
DT 3	13	40.30	0.52	3.33	0.24
DT 4	8	55.51	0.46	3.30	0.14
DT 5	12	71.06	0.31	3.07	0.19
Wet bending					
WB 1	20	11.82	0.11	3.62	0.42
WB 2	21	15.94	0.12	3.45	0.14
WB 3	17	20.11	0.06	1.48	0.13
WB 4	11	53.49	0.95	3.41	0.10
WB 5	13	53.65	0.84	1.99	0.14
Wet torsion					
WT 1	21	11.72	0.27	4.05	0.45
WT 2	21	20.37	0.13	3.19	0.48
WT 3	20	27.82	0.36	3.48	0.27
WT 4	9	38.87	0.36	0.52	0.13
WT 5	11	53.67	0.80	3.04	0.14

erally below 0.3 % for the dry configuration, whereas under wet conditions slightly larger spreads are observed for selected clusters, particularly for some of the lower frequency bending and torsional cases. Although a moderate increase in variability can be identified for certain higher frequency clusters and individual wet clusters, the relative scatter remains limited compared to the corresponding mean values.

As noted in Sections 5.2 and 5.3, five repetitions were performed for each excitation location in the dry configuration, whereas seven repetitions were conducted under wet conditions. This results in a maximum of 15 possible observations per physical mode for the dry tests and 21 possible observations per mode for the wet tests. Consequently, the number of data points assigned to each cluster additionally provides a direct measure of the consistency and reliability of the modal identification.

A roving excitation strategy was applied in the dry configuration, where the excitation location was changed after each run, whereas under wet conditions the excitation location was kept constant for a sequence of repetitions. In the clusters presented in Appendix E.1, this procedural difference between dry and wet runs is reflected in the observed spread of the clustered data. Although variability is still present in the wet data, systematic shifts can be observed depending on the excited floater.

6.2.2. Modal identification accelerometer data

A qualitative agreement between numerically predicted and experimentally observed mode shapes was assessed using the accelerometer data. As the accelerometers were positioned on the floater surfaces, the measured signals represent axis dependent translational components of rotational motion rather than distributed translational amplitudes along a single bending axis. A direct overlay of measured amplitudes with predicted mode shapes is therefore not meaningful. Instead, the response was interpreted through a three dimensional reconstruction of model deformation based on measured amplitudes and phase relations.

An example of this reconstruction is shown in Figure 34e. The right panel presents a top view of the bending dominated mode. The black arrows indicate the direction of motion of the accelerometers, while the coloured arrows represent the corresponding translational components measured along the individual accelerometer axes. The FRF's obtained from the accelerometers during the five radial excitation runs on floater B are also shown in Figure 34e, using the same colour coding to represent different accelerometers. A clear peak is observed at approximately 30 Hz, corresponding to cluster DB2 identified in Table 15. By comparing the relative lengths of the arrows with the amplitudes of the FRF's at 30 Hz, it can be seen that their relative magnitudes are consistent with the behaviour expected for Mode 2.

By extending this approach with the extracted phase angles of each node, as well as to the accelerometers located on the beams, the three dimensional representation shown in Figure 35 can be constructed. From this comparison, the horizontal axis of rotation of each floater can be observed, and a qualitative agreement between the numerically predicted bending mode and the experimentally observed mode shapes is observed. It can therefore be concluded that Cluster 2 is indeed made up of the global bending mode. Representative figures of deformed plots are presented in Appendix E.2.

6.2.3. Mapped strain mode shapes and MAC evaluation

Axial strain was measured using three strain gauges along each beam, as described in Section 5.1. For non-axially symmetric modes, the beam responses were spatially mapped relative to the excited floater such that all beams could be represented in a consistent reference frame.

Comparisons between normalised numerical strain predictions and experimental observations in the wet configurations are presented in Figures 36 to 41. Equivalent figures for the dry configuration are presented in Appendix E.3. For each identified cluster, the strain responses per gauge were averaged to obtain a representative experimental strain distribution. The candle plots at each gauge location illustrate the spread of the individual observations within each cluster. The resulting MAC matrices are depicted in Tables 16 and 17. As observed from the strong agreement along the diagonal for both dry and wet conditions, it can be confirmed that the predicted numerical modeshapes are well represented in experimental observations.

From the candle plots in Figures 36 to 41, it can be seen that the repeatability of the identified modes varies. In particular, the

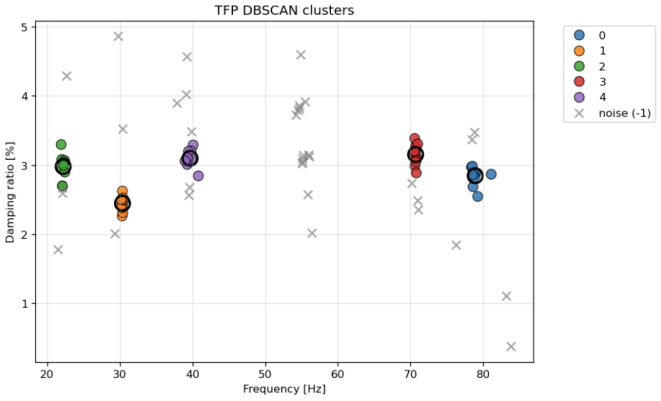

(a) Dry bending ($\varepsilon = 0.35$, $n_{\min} = 8$)

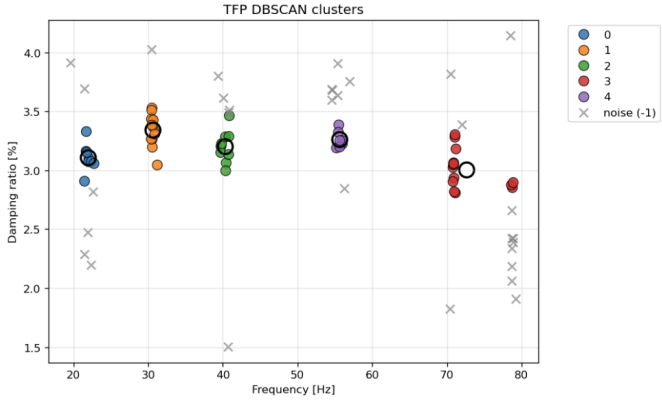

(b) Dry torsion ($\varepsilon = 0.35$, $n_{\min} = 8$)

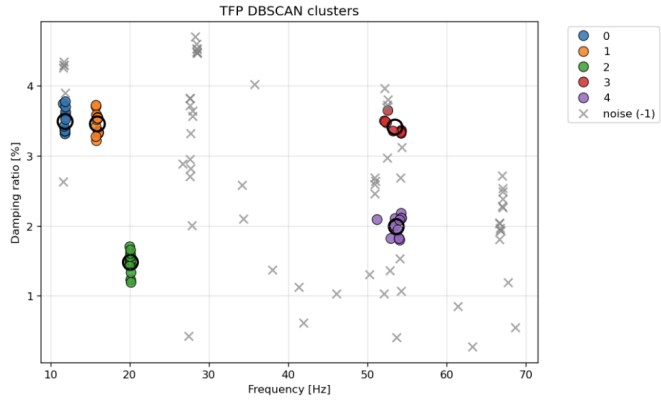

(c) Wet bending ($\varepsilon = 0.18$, $n_{\min} = 8$)

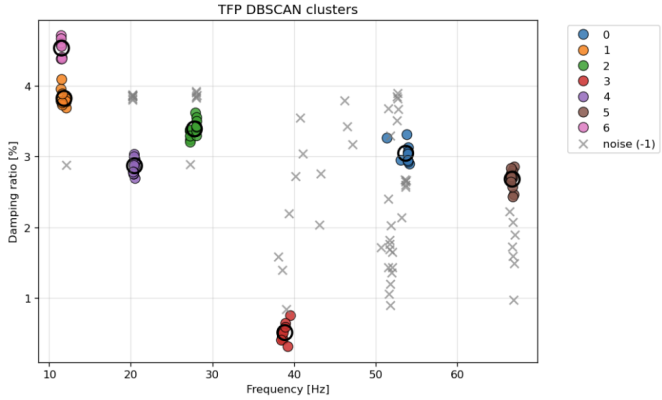

(d) Wet torsion ($\varepsilon = 0.20$, $n_{\min} = 8$)

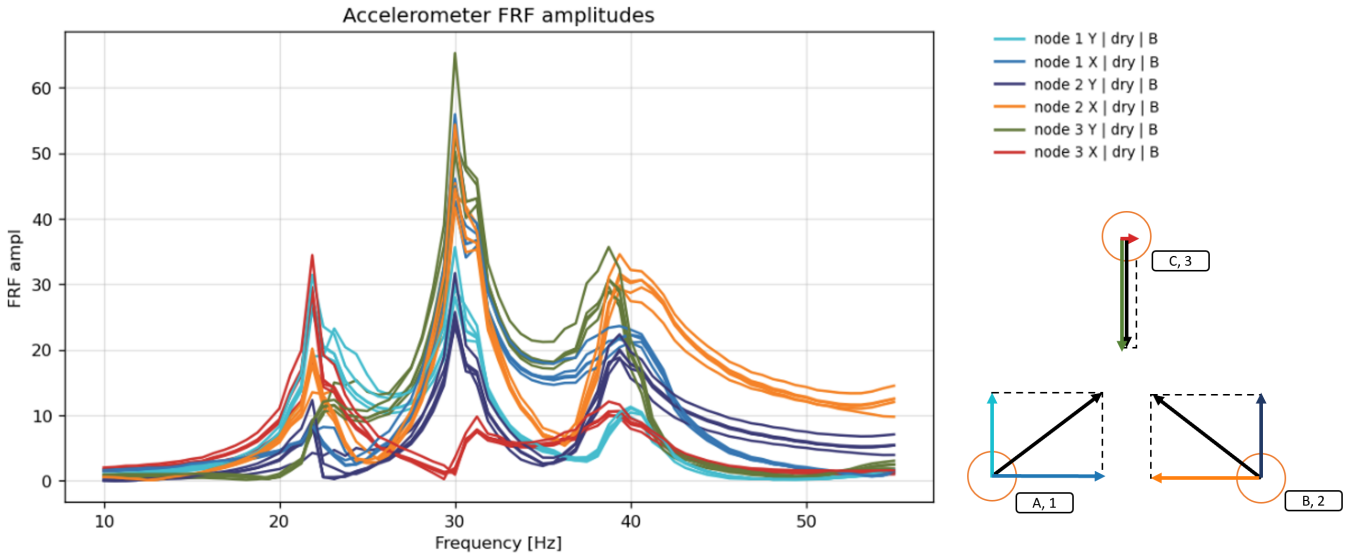

(e) Floater skin accelerometer FRF's for radial excitation of floater B, colour coded by measurement direction

Figure 34: DBSCAN clustering results for dry and wet bending and torsional modal data, with an example set of floater skin accelerometer FRF's. The DBSCAN settings are reported in the corresponding subcaptions.

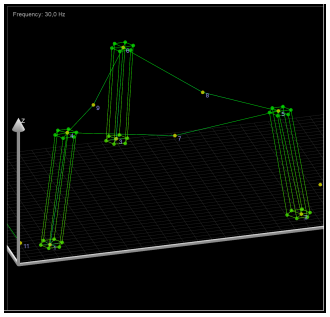

(a) Dry bending, Cluster 2 representation.

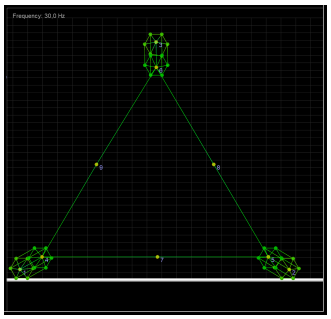

(b) Dry bending, Cluster 2 topview.

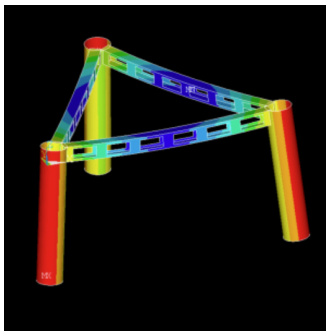

(c) FEM Mode 2 representation.

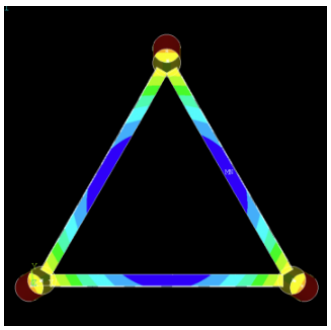

(d) FEM Mode 2 top view.

Figure 35: Comparison of experimentally identified and numerically predicted dry bending mode shapes

strain distributions shown in Figure 38 exhibits variable measurements. This is noteworthy, as the numerical prediction for this mode indicates a nearly uniform strain distribution along the beams.

For the wet configuration, no distinct cluster corresponding to Mode 4b was identified by the DBSCAN algorithm. Inspection of Figure 34c shows that observations are present in the relevant frequency range, but are dispersed in damping and therefore do not satisfy the density criteria required for cluster formation under the selected parameters.

To assess whether the data points observed between 25 and 30 Hz correspond to Mode 4b, the DBSCAN classification was disregarded and the results were manually filtered. As shown in Figure 41, these observations exhibit a reduced MAC value and high strain variability, indicating relatively poor correspondence with the numerical Mode 4b.

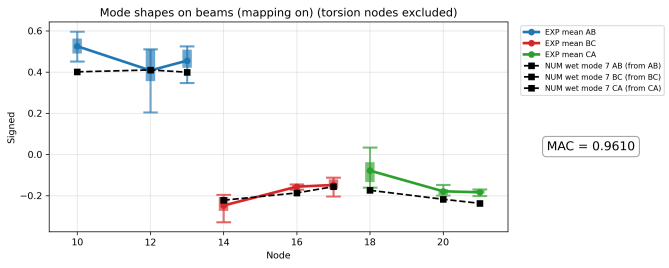

Figure 36: Wet condition MAC comparison between Cluster WB1 and numerical Mode 1a.

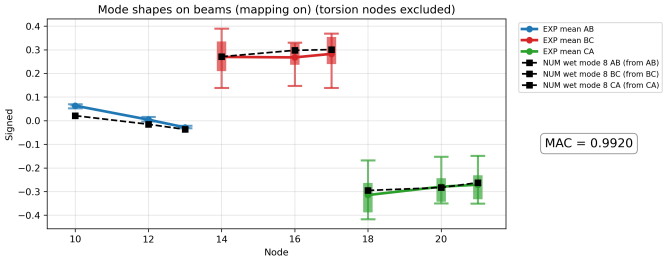

Figure 37: Wet condition MAC comparison between Cluster WT1 and numerical Mode 1b.

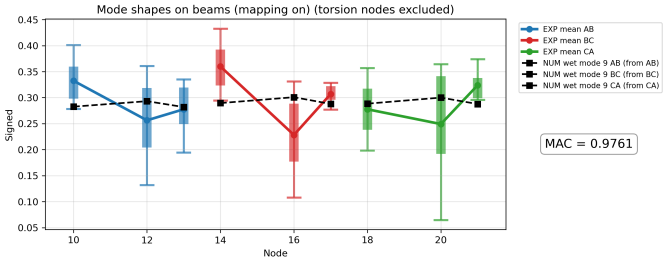

Figure 38: Wet condition MAC comparison between Cluster WB2 and numerical Mode 2.

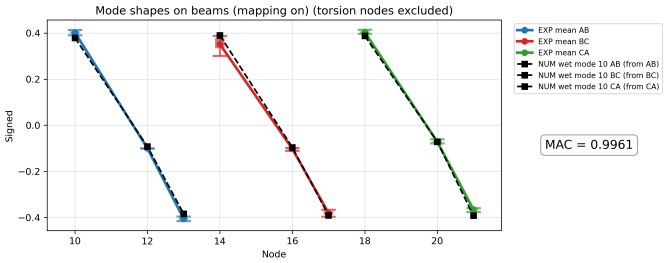

Figure 39: Wet condition MAC comparison between Cluster WT2 and numerical Mode 3.

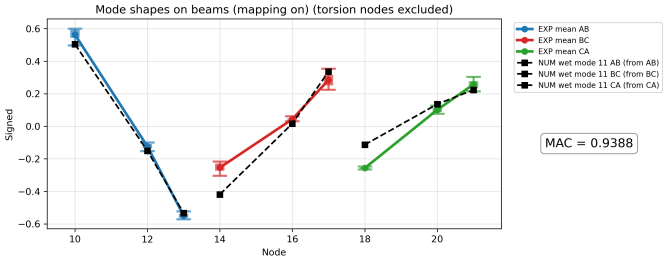

Figure 40: Wet condition MAC comparison between Cluster WT3 and numerical Mode 4a.

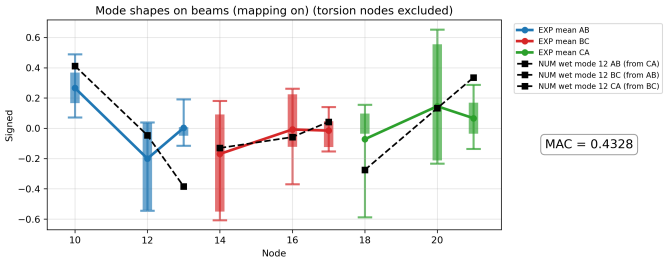

Figure 41: Wet condition MAC comparison observations between 25 and 30 Hz and numerical Mode 4b.

Table 16: MAC values between numerical modes and experimental clusters in dry conditions.

Mode	DB1	DT1	DB2	DT2	DT3	DB3
1a	.9592	.9028	.0012	.0005	.0074	.0734
1b	.8159	.9553	.0001	.0050	.0040	0.0086
2	.0002	.0002	.9955	.0307	.0007	.0169
3	.0022	.0002	.0058	.9863	.0015	.0003
4a	.0077	.0221	.0000	.0016	.9737	0.7569
4b	.1790	.0089	.0010	.0005	.8135	.9654

Table 17: MAC values between numerical modes and experimental clusters in wet conditions.

Mode	WB1	WT1	WB2	WT2	WT3	Man.
1a	.9610	.6850	.0000	.0001	.0091	.0837
1b	.6572	.9920	.0004	.0018	.0042	.0796
2	.0177	.0000	.9761	.0089	.0005	.0001
3	.0040	.0001	.0025	.9961	.0002	.0002
4a	.0018	.0044	.0058	.0001	.9655	.4625
4b	.0025	.0020	.0002	.0005	.9388	.4328

6.3. *Dynamic modal validation*

From all of the presented data and post-processing procedures, the consolidated modal identification results presented in Table 18 could be determined. Under dry conditions, all modes were consistently identified. In the wet configuration, all modes except 4b were isolated as distinct clusters. As discussed in Section 6.2.3, Mode 4b was not identified as a separate cluster by the DBSCAN algorithm. After manual filtering the mode is still not captured as clearly as all other observations.

6.3.1. *Dynamic Young's modulus calibration*

As outlined in Section 2.5, no definitive dynamic Young's modulus could be extracted from the specimen tests described in Appendix A. Based on the testing observations, a Young's modulus of 2.0 GPa was adopted as input for the numerical model.

Although this value is close to both the manufacturer reported modulus and the flexural modulus identified in Section 5.4.1, Table 18 shows that the numerical model systematically underpredicts the natural frequencies when $E = 2.0$ GPa is used.

An inverse identification of the effective structural stiffness was therefore performed. Increasing the modulus to 2.5 GPa best improves agreement, with most modes predicted within approximately 5% of the experimentally observed frequencies for both dry and wet configurations.

While inverse identification does not constitute direct material characterisation, an important observation is that the reduction in frequency deviation between $E = 2.0$ GPa and $E = 2.5$ GPa is nearly uniform across all identified modes. The theoretical relationship between natural frequency and stiffness, $f \propto \sqrt{E}$, predicts a frequency increase of approximately 11.8% for this stiffness change. The observed mean frequency shift of 11.36% closely aligns with this theoretical expectation.

Consequently, the relative error reduction is approximately 10% for each mode, with variations below 0.5%. This consistent and predictable shift indicates that the discrepancy at $E = 2.0$ GPa originates from a global stiffness underestimation rather than from mode specific modelling artefacts.

The results therefore support the interpretation of Young's modulus as an appropriate global calibration parameter. With $E = 2.5$ GPa, the numerical model adequately reproduces the experimentally observed natural frequencies across bending and torsional modes.

6.3.2. *BEM prediction validation and observed damping*

Table 18 shows that the frequency deviations obtained for dry and wet conditions are of comparable magnitude and remain largely consistent across the identified mode set. This indicates that the adopted BEM added mass representation, as introduced in Section 3.1, captures the dominant hydrodynamic inertia contribution adequately. It is therefore found likely that the remaining discrepancy is primarily governed by global structural stiffness rather than by deficiencies in the added mass approximation.

The mean identified damping ratio is 3.01% for the dry configuration and 3.56% for the wet configuration. A modest increase in damping is therefore observed in wet conditions. The damping levels remain of similar order across all modes, and the spread within individual clusters is limited.

6.3.3. *Modeshape variability*

Visual inspection of the deformed representations indicated that floater rotation angles generally align with numerical predictions. Additionally, MAC values from strain based measurements align closely with numerical predictions for almost all modes. In terms of observed floater rotation angles however, larger variability was observed, particularly under wet conditions. An example is shown in Figure 42, where deviations in rotation angles relative to the numerical prediction are apparent in the bottom two floaters. The magnitude of these deviations was however not consistent between repeated excitations.

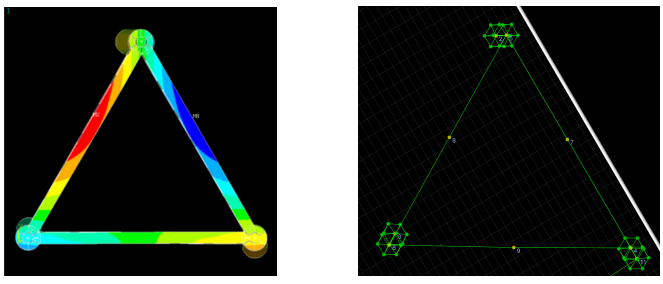

(a) Wet Mode 1a FEM representation (b) Deformed plot Cluster WT1

Figure 42: Top view comparison of Mode 1a and Cluster WT1.

Although a complete quantitative assessment of floater rotation angles was not performed, indications of this variability are observed in the MAC plots presented in Figures 36 to 41. The observed misalignment between numerical and experimental strain distributions reflect that the reconstructed modal shapes

do not perfectly capture the relative floater rotation angles. The candle plots similarly illustrate a measurable spread which is considered consistent with the visual variability observed in the deformed plots for the non-axially symmetric modes.

6.3.4. Accelerometer placement limitations

Part of the observed variability is attributed to the accelerometer placement strategy. Only a single vertical array of accelerometers was installed along each floater, and no sensors were positioned at the Beam–Floater Interfaces. The modal reconstruction therefore implicitly assumes that the Beam–Floater Interfaces remain perfectly stationary. Any rigid body motion of the beams relative to the floaters cannot be independently separated from the measured response and may therefore influence the reconstructed mode shapes.

This limitation becomes more pronounced under wet conditions. Added mass shifts the effective centre of rotation of the floaters downward for modes 3, 4a, and 4b. Consequently, the accelerometers on the skin were positioned closer to the instantaneous centre of rotation, leading to reduced measurable translational amplitudes and a higher variability in observed floater rotation angles.

6.4. Dynamic beam similarity analysis

As outlined in Section 3.4, the numerically predicted floater rotation angles were consistent regardless beam specifics. To assess possible causes of the observed misalignments in floater rotation angles, a more in-depth dynamic analysis of the individual beams is performed. This is done through observations of the extracted FRF's from the strain gauges.

The beam response can be compared in two manners, the first considers the response of strain gauges at Positions 1–4 for each beam when a specific floater is excited, as shown in Figure 43. In this representation, differences in beam behaviour can be observed based on their relative position with respect to the excitation. This enables an analysis similar to that performed for the accelerometer data in Section 6.2.2, where relative amplitudes at peaks such as those observed at 22 Hz and 30 Hz provide insight into the global beam response.

From this analysis, it is observed that the FRF's exhibit reasonably well clustered behaviour per beam and per run. As shown in Figure 43, the FRF's vary only to a limited extent between repeated runs. For the wet FRF's, for which no sequential runs were performed, this clustering behaviour appears even more pronounced.

The second method of analysis again considers the strain response at Positions 1–4, but applies the same mapping strategy adopted in Section 6.2.3. In this case, beams are plotted according to their position relative to the excited floater rather than their global position. This representation is illustrated in Figure 44. Here, the colours indicate which floater was excited, while the relative beam position remains fixed, causing the responses of three different beams to overlap.

Under ideal symmetry, identical responses would therefore be expected. Analysing the data in this manner enables a direct comparison between beams and between individual beam segments, allowing deviations from idealised behaviour to be identified.

The mapped representations shown in Figure 44 reveal that the strain responses exhibit a high degree of similarity between beams, with the dominant resonance peaks generally occurring at consistent frequencies and displaying comparable response distributions. However, the responses do not collapse onto a single curve. Instead, each beam forms a clustered group, with small but systematic offsets in amplitude relative to the others. As a result, the individual beam responses are more strongly clustered around their own characteristic trends than around a single global response.

Although this effect appears limited in the presented FRF's in Figure 44, discrepancies of up to approximately 50% at the resonance peak around 22 Hz (Position 1) and up to 70% at the peak around 30 Hz (Position 4) can be observed. In addition, the orange FRF's in Figure44, representing global Beam AB, consistently exhibit a delayed peak at approximately 40 Hz. While amplitudes represent possible local variability, a peak shift indicates a globally different behaviour.

The clearest discrepancies are observed when considering the FRF's of the mapped Beam BC, representing the beam located opposite the excited floater. This beam is hypothetically the least influenced by the boundary conditions imposed by the excitation, and should therefore depict the most consistent behaviour between beams. These responses are presented in Figure 45.

It can be observed that indeed the dominant resonance frequencies remain relatively consistent across beams. Nevertheless, systematic differences in peak magnitude and overall response level are present. For example, in the Dry torsional configuration presented in Figure 45b, Beam CA (depicted as the cyan curves) exhibits a different response from Beams AB and BC. This is most notable in Position 1, where the first resonance peak is observed at a lower frequency than Beam AB and CA. A similar difference in response can be observed in the Wet bending configuration depicted in Figure 45c.

Other observation can be made about Beam AB, which in the dry bending configuration (Figure 45a), is consistently observed to exhibit a reduced response at Position 2. The opposite behaviour can however be observed in the Wet bending configuration (Figure 45c), where it shows a consistently higher response at Position 2.

6.4.1. Beam similarity sensitivity

To assess whether the observed strain FRF differences could explain the variability in floater rotation angles outlined in Section 6.3.3, an intentionally non symmetric numerical model was analysed. The resulting floater rotation patterns, presented in Appendix E.3.1, demonstrate that even substantial imposed asymmetry has only a limited influence on the observed numerical modeshapes.

Table 18: Consolidated modal identification results for dry and wet configurations.

Cluster	Mode	f_{mean} [Hz]	ζ_{mean} [%]	n_p	f_{num} E2.0 [Hz]	Err [%]	f_{num} E2.5 [Hz]	Err [%]	$\text{MAC}_{\text{strain}}$
DT1	1a	21.97	2.95	13	19.28	-12.24	21.51	-2.09	0.9592
DB1	1b	22.18	2.92	11	19.29	-13.03	21.52	-2.98	0.9553
DB2	2	30.38	2.46	11	27.43	-9.44	30.54	0.83	0.9955
DT2	3	30.63	3.34	12	25.57	-16.52	28.50	-6.95	0.9863
DT3	4a	40.30	3.33	13	35.54	-11.81	39.55	-1.86	0.9737
DB3	4b	39.55	3.07	11	35.63	-9.91	39.65	0.25	0.9654
WB1	1a	11.82	3.62	20	10.60	-10.32	11.82	0.00	0.9610
WT1	1b	11.72	4.05	21	10.60	-9.56	11.82	0.85	0.9920
WB2	2	15.94	3.45	21	14.93	-6.34	16.60	4.14	0.9761
WT2	3	20.37	3.19	21	17.41	-14.53	19.40	-4.76	0.9961
WT3	4a	27.82	3.48	20	25.59	-8.02	28.43	2.19	0.9655
Man.	4b	27.93	3.55	19	25.65	-8.16	28.49	2.01	0.4328

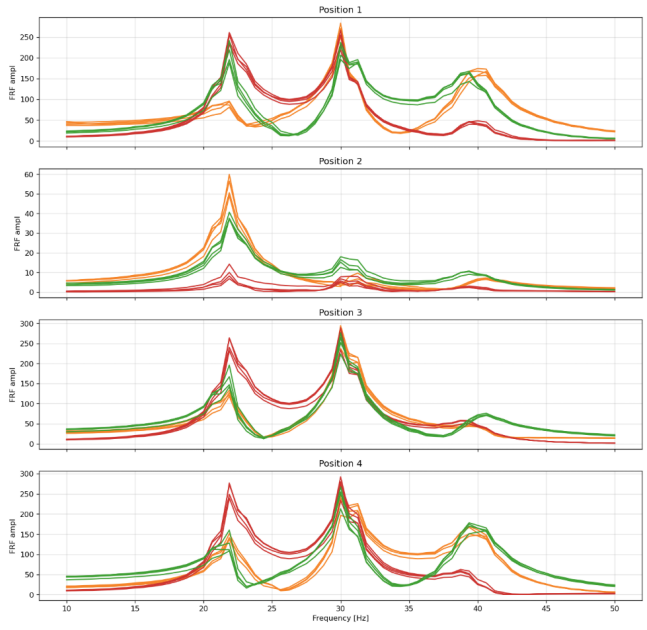

Figure 43: Dry bending test, floater A, Beams AB (orange), BC (red), CA (green), runs 1-5

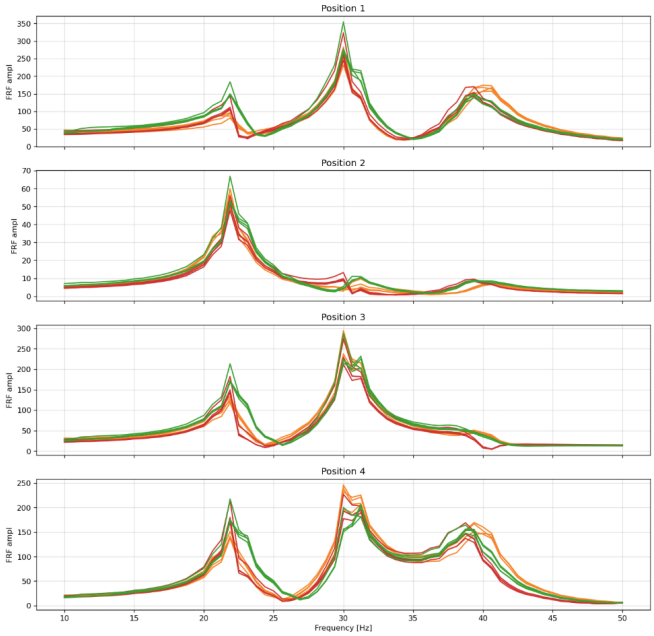

Figure 44: Dry Bending test, Beam right of excited floater A (orange), B (red), C (green), runs 1-5

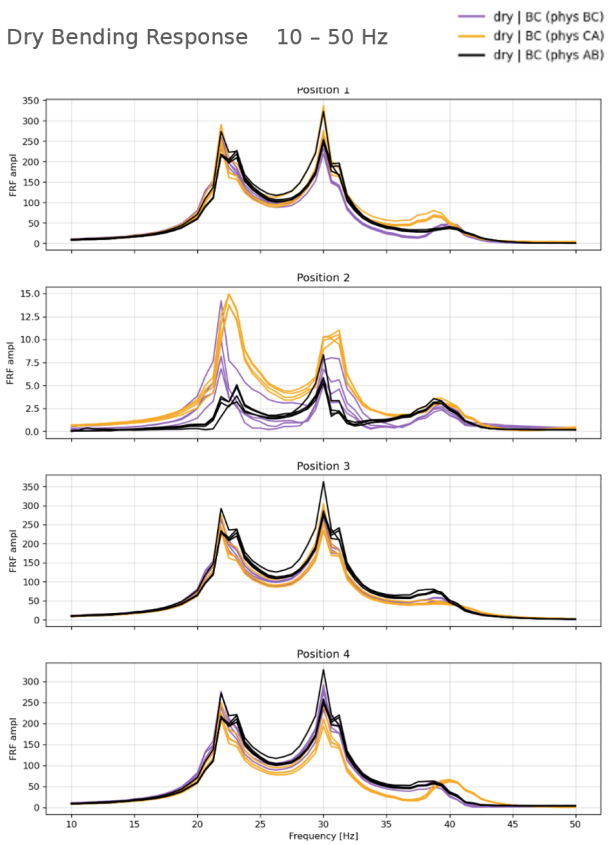

(a) Dry bending response

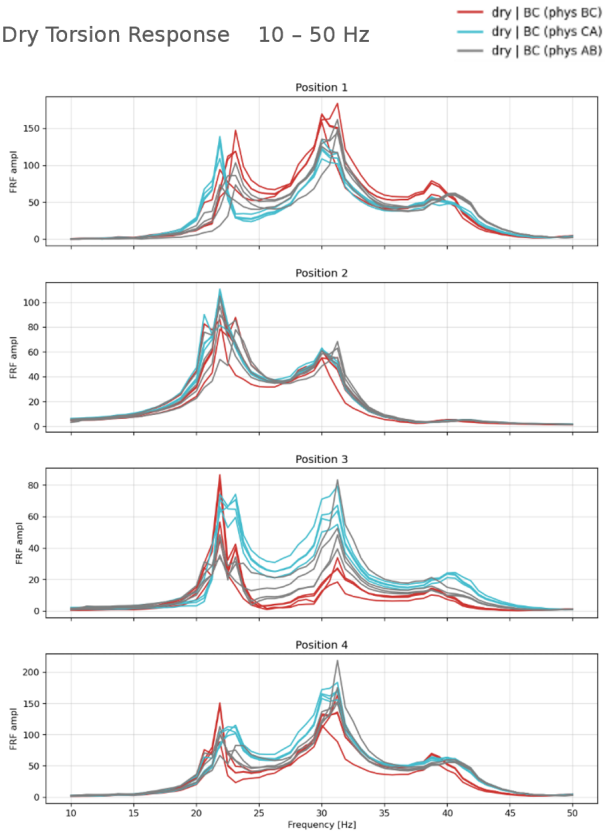

(b) Dry torsional response

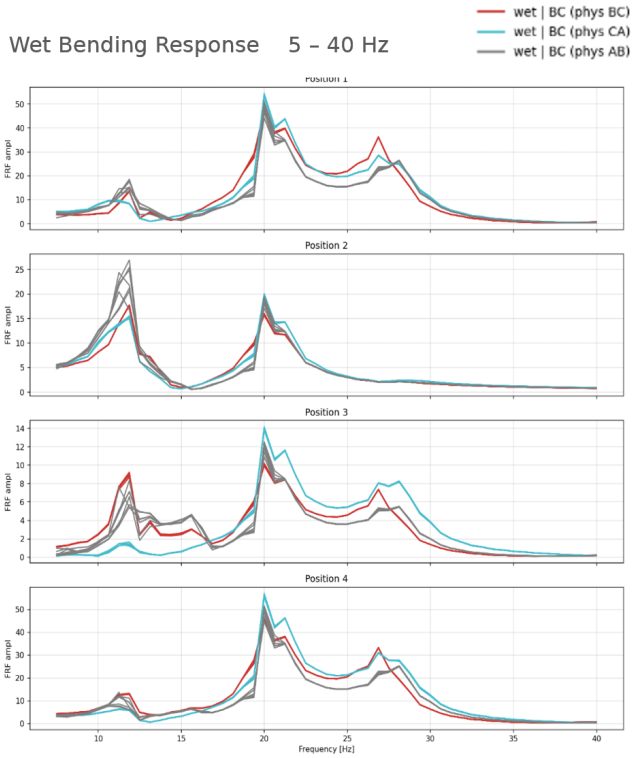

(c) Wet bending response

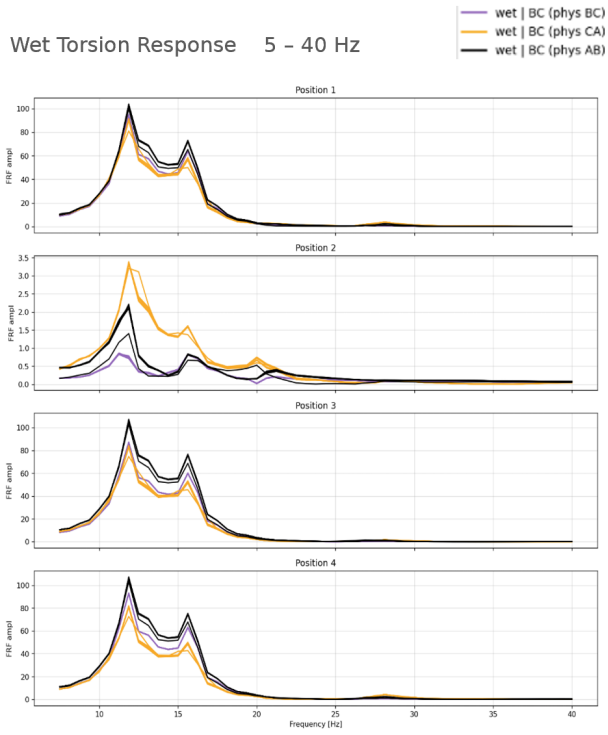

(d) Wet torsional response

Figure 45: Frequency response functions obtained from strain gauge measurements for dry and wet conditions, showing bending and torsional response components.

6.5. *Local mode identification*

From the clusters presented in Table 15, several higher frequency modes were observed during dynamic testing. These correspond to four additional modes that were numerically predicted below 70 Hz under wet conditions. Two horizontal beam bending modes and two vertical beam bending modes, occurring either in phase or out of phase, were predicted numerically beyond the presented global modes. These modes are depicted in Figure 46.

These modes were predicted at very similar frequencies in both dry and wet numerical conditions. For the horizontal bending modes, which were predicted around 53 Hz, experimental data points were observed in this frequency range. This is observed in Figures 34a to 34d.

However, as no strain gauges or accelerometers were fitted on the sides of the beams, these modes could not be reliably extracted from either accelerometer or strain gauge data, it is likely this also attributed to the strong scatter in this range. Given the strong agreement observed for the lower global modes however, it is considered confirmed that the identified data points correspond to the predicted horizontal bending behaviour.

The local vertical beam bending modes were clearly identifiable from the accelerometer measurements. Their deformed representations are presented in Appendix E.2. A comparison between numerical predictions and experimentally identified frequencies of all local modes is summarised in Table 19.

Numerically, these higher order modes are local in nature and involve only limited floater rotations. Consequently, during slamming events acting on the floaters, excitation of these modes is expected to be weak, as the forcing occurs away from their dominant deformation regions.

This limited participation is supported by the experimental data. The strain gauge FRF's shown in Figure 45 exhibit negligible strain response for frequencies above the identified global modes. Similarly, the beam mounted accelerometer FRF's in Figure 46e show clear resonance peaks around 70 and 80 Hz, corresponding to the predicted local vertical bending modes. However, these resonances do not translate into significant floater motion, as demonstrated by the floater accelerometer responses shown in Figure 46f.

Table 19: Comparison between experimentally identified higher order natural frequencies and numerical predictions.

Cluster	Mode	f_{mean} [Hz]	f_{num} E2.5 [Hz]	Error [%]
DT 4	5a	55.51	53.90	-2.99
DT 4	5b	55.51	53.98	-2.83
DB 4	6	70.76	65.29	-8.38
DB 5	7	78.91	73.26	-7.71
WB 4	5a	53.49	52.89	-1.13
WB 4	5b	53.65	52.96	-1.30
WT 7	6	68.09	61.95	-9.91
–	7	–	67.89	–

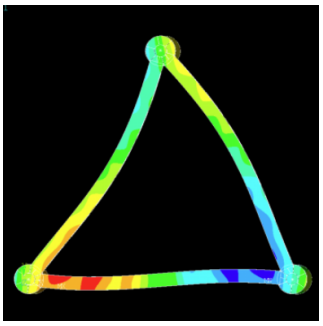

(a) Horizontal local beam bending Mode 1, predicted at 53.90 Hz.

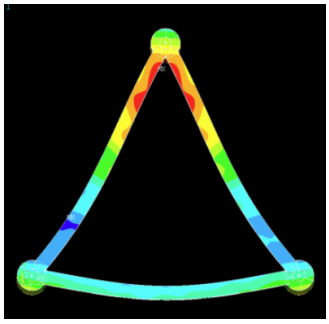

(b) Second horizontal local beam bending mode, predicted at 53.98 Hz.

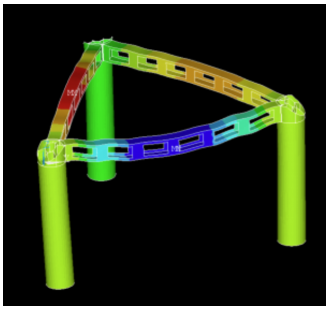

(c) Out of phase vertical local beam bending mode, predicted at 65.29Hz.

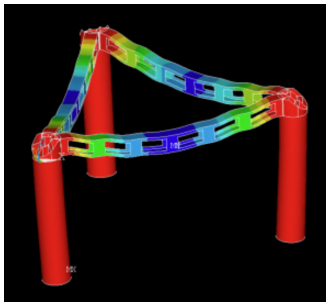

(d) In phase vertical local beam bending mode, predicted at 73.26 Hz.

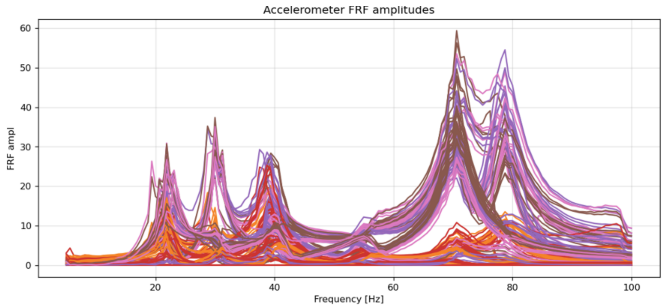

(e) Dry condition beam accelerometer FRF's.

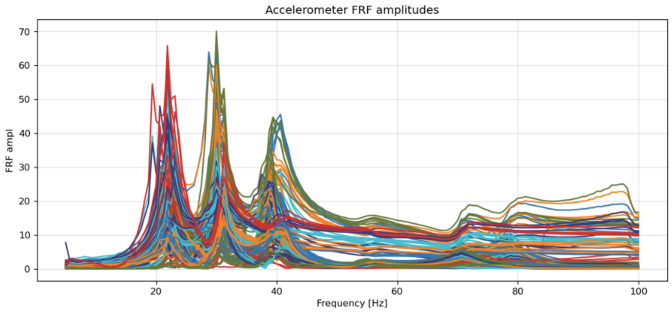

(f) Dry condition floater accelerometer FRF's.

Figure 46: Numerically predicted local beam bending modes under dry conditions.

7. Discussion

To evaluate the validity of the proposed methodology, several complementary analyses were performed. The target and experimentally observed natural frequencies are summarised in Table 20, together with a qualitative comparison of the corresponding modeshapes. However, a direct numerical comparison between target and observed frequencies alone does not fully reflect the validity of the methodology, as it is affected by the added mass modelling inconsistency discussed in Section 4.6.1.

Table 20: Target and observed natural frequencies.

Mode	f_{target}	f_{expected}	f_{realised} [Hz]	Modeshape acc.
1a	10.60	11.82	11.82	varying
1b	10.60	11.82	11.72	varying
2	12.52	16.60	15.94	good
3	17.54	19.40	20.37	good
4a	–	28.43	27.82	unknown
4b	–	28.49	27.93	unknown

Proposed numerical modelling methods

More meaningful conclusions regarding the validity of the methodology can be drawn from the overall modal verification results. As demonstrated in Section 6.3, following material calibration, the numerically predicted natural frequencies and global strain patterns, as indicated by the obtained MAC-values, show good agreement with the experimentally identified modes in both dry and wet configurations. The observed natural frequency deviations generally remain within 5% of the numerical predictions, which compares favourably with values commonly reported in the literature (7).

The arguments presented in Sections 6.3.1 and 6.3.2 indicate that the material stiffness serves as an effective global calibration parameter. Consequently, the coupled FEM–BEM modelling approach can be considered suitable for predicting the dominant global modal behaviour of the structure. This outcome aligns with the established role of coupled FEM–BEM formulations in hydroelastic analysis (20).

Proposed design and construction method

The proposed design and construction methodology demonstrates sensitivity to mass deviations. As discussed in Section 4.6, construction-related adjustments had a noticeable influence on the predicted natural frequencies. Within the optimisation framework described in Section 3.3.1, the model mass was determined numerically, and deviations from the target were compensated through ballast placement at the floater bottoms. Although this approach is expected to remain robust under more moderate mass targets, the realised construction results indicate that the implemented mass estimation did not accurately represent the final system mass.

The optimisation procedure did not produce a geometry that simultaneously matched all targeted global modes. This limitation is likely caused by competing stiffness requirements within the beam system, as described in Section 3.4.2.

The adopted square cross section with square cut-outs introduces structural constraints. As discussed in Section 3.4.5, this geometry leads to pronounced strain gradients during loading. Although the strain gauges were positioned to minimise sensitivity to these effects, as outlined in Section 6.1, the gradients remain a potential source of measurement variability.

One possible mechanism contributing to the observed strain variability is stiffness discontinuity across the beam cross-section. As discussed in Section 4.2.2, slight variability was observed in the snap-fit connections, particularly near the corner regions of the segment joints. If this variation results in non-uniform stiffness within the cross-section, it may introduce local stress concentrations and alter the strain distribution, thereby influencing the extracted strain measurements.

The construction method may also have introduced slight axial asymmetry in the model. The cluster close-ups presented in Appendix E.1 show that the identified natural frequencies vary depending on which floater is excited. This behaviour is observed in both dry and wet conditions and consistent with peak shifts observed between excitation locations in the strain FRFs presented in Section 6.4.

Although the modeshape variability discussed in Section 6.3.3 was initially attributed to axial asymmetry, the sensitivity study presented in Section 6.4.1 showed that the modeshapes are not sufficiently sensitive to asymmetry of the magnitude observed. The variability is therefore more likely caused by boundary condition effects introduced by the shaker, limitations in accelerometer placement as discussed in Section 6.3.4, or unidentified effects in measurement or post-processing.

Tough2000 and SLA manufacturing

The precise and continuous mechanical properties of Tough2000, as well as its reported isotropy (22), could not be verified with high certainty. Although, as described in Section 4.2.1, identical printing and post-curing procedures were applied to all segments, measurable variability between segments was observed.

A mean damping ratio of 3.80% was obtained from the material specimen tests. For the assembled model, damping ratios ranged between 2.46% and 3.34% in dry configuration and between 3.19% and 4.05% in wet configuration. Reported damping ratios for segmented and elastic hydroelastic ship models are typically lower, often around 0.5% – 2% for the first dry mode (7). The values identified here are comparatively high. The underlying cause of this elevated damping remains uncertain, though it is possibly related to the viscoelastic behaviour of Tough2000.

At the global level, the static experiments discussed in Section 6.1 indicated a flexural modulus of approximately 1.9 GPa. In contrast, dynamic specimen testing presented in Section 2.6 and model calibration discussed in Section 6.3.1 suggested values of 2.0 and 2.5 GPa, respectively. This discrepancy indicates strain-rate sensitivity, introducing uncertainty in the absolute material stiffness. The linear relationship observed in the weight–strain curves from the static tests indicates that Tough2000 behaves linearly elastic within the investigated loading range.

At the local level, strain measurements obtained during the static experiments were not fully repeatable under nominally identical boundary conditions and loading configurations. Similar behaviour was observed in the dynamic results. Variability is present in the strain gauge responses, as discussed in Section 6.2.3, and in the distributions of the strain FRFs presented in Section 6.4.

A representative example is provided in Figure 38. For the corresponding bending mode, the numerical model predicts an almost uniform axial strain distribution with negligible local variation. In contrast, measurable spatial variability is observed in the experimental strain data.

However, this behaviour cannot be attributed solely to material variability. The observed differences may also result from local stiffness variations caused by geometric sensitivity and segmentation effects, as discussed previously.

Previous studies have reported challenges associated with strain gauge application on polymer substrates, including gauge stiffening, creep effects, and thermal expansion mismatch (13; 18). In the present study, thermally compensated strain gauges in half Wheatstone bridge configuration were used to minimise these effects. Nevertheless, the results highlight the sensitivity of strain-based measurements in compliant polymer structures.

Technical Recommendations for Methodology Improvement

Based on the observations outlined in the preceding sections, two principal refinements of the proposed methodology are identified.

First, optimisation of the beam geometry is recommended. A segment design less susceptible to torsional warping and through-thickness strain gradients would reduce sensitivity to local stiffness variability. In practice, this implies avoiding square cross sections and square cut-outs. Reducing the number of segmented interfaces, or adopting a connection strategy with more controlled stiffness characteristics, would further decrease structural variability and associated uncertainty.

Second, a more conservative and systematic mass estimation strategy should be incorporated during the numerical design stage. Pre-fabrication identification of all required components and detailed estimation of their individual mass contributions would reduce the likelihood of weight overruns. Earlier anticipation of potential mass deviations would enable more proactive weight reduction measures, as well as preliminary adjustments to draft and added mass modelling prior to fabrication. This prevents relying on the reactive weight-handling approach adopted in the present study.

Model-specific recommendations

For experimental campaigns based on the present model configuration, systematic component-level dynamic testing under controlled boundary conditions is recommended. Complementary specimen testing using larger samples that are less sensitive to boundary effects would further increase confidence in the effective material properties.

The measurement configuration can also be refined. Installing an additional set of accelerometers near the Beam–Floater Interface would enable more accurate reconstruction of floater rotations, and provide more insight into the exact mechanisms leading to the observed floater rotation angle variability.

As discussed in Section 5.1.2, the addition of strain gauges alone would not eliminate aliasing effects. However, expanding strain gauge coverage to all beam segments would improve the spatial resolution of both static and dynamic strain measurements and provide a larger dataset for material property estimation. This would also facilitate identification of potential segment-level irregularities in currently uninstrumented segments.

Experimental validation of the mode shapes could also be expanded. Although the number of test runs was sufficient to confirm the dominant dynamic properties, additional measurements would provide greater insight into potential model asymmetry. In the dry configuration, roving excitation revealed slight asymmetry in the structural response. Under wet conditions, a more pronounced asymmetry was observed. Because the roving procedure was not repeated in the wet configuration, it remains difficult to determine whether this increased asymmetry reflects intrinsic structural behaviour or boundary-condition effects introduced by the modal shaker.

Finally, targeted component-level testing of the Beam—Floater Interface is recommended to quantify its effective stiffness. Although unintended compliance is not currently indicated, dedicated testing would verify this assumption. Verification of predicted floater skin frequencies through component-level testing is also advised prior to conducting slamming experiments.

Implications for slamming research

The suitability of the constructed model for slamming experiments aimed at quantifying the structural response of the full-scale *Merganser* platform cannot be conclusively established. The modelling inconsistency in the added mass formulation introduces deviations from the exact scaled frequency targets, thereby affecting dynamic similitude.

In addition, two global modes were identified beyond the scaled target frequency range. These modes involve floater rotations and are therefore likely to be excited during slamming events at model scale. To assess the representativeness of the scaled response, identification of corresponding higher-order global modes in the full-scale *Merganser* platform, is required.

More fundamentally, the observed segment-level strain variability, combined with uncertainty in the effective material properties, suggests that reliable characterisation of structural response under slamming excitation will be challenging. Inverse identification of slamming loads from measured structural response is therefore expected to be even more demanding, particularly given observed similar limitations reported in the literature and the highly non-linear and stochastic nature of slamming events (6).

For the present model, the rigid floater assumption enabled a clear separation between global structural modes and local floater deformation, as discussed in Section 6.5. The observed

six global modes are consistent with the rigid three-floater configuration. Each floater can rotate about two horizontal axes, resulting in six global rotational degrees of freedom for the system. A system with six dominant degrees of freedom can exhibit at most six global mode shapes; any additional dynamic behaviour must therefore be local in nature.

This clear separation was observed under the tested harmonic excitation conditions, where floater rigidity at model scale was sufficiently high. Whether this separation persists under high-frequency, high-amplitude slamming excitation remains uncertain. As outlined in Appendix C, local hydroelastic effects at floater level cannot be fully excluded and may influence the structural response. These uncertainties affect not only the scaled model but also the interpretation of full-scale behaviour, as the nature of potential local floater modes in the *Merganser* platform remains unknown.

8. Conclusions

The objective of this study was to develop a methodology for constructing a scaled flexible model capable of reproducing the global dynamic properties of the *Merganser* platform, thereby establishing a foundation for investigating slamming-induced structural behaviour.

This objective was achieved with identified limitations. Calibration of the Tough2000 material stiffness resulted in close agreement between predicted and measured frequencies in both dry and wet conditions, supporting the validity of the applied numerical modelling approach. Main contributions to deviation between target and observed frequencies included modelling inconsistencies and excessive model mass.

While accelerometer-based modeshape identification showed variability, likely influenced by measurement limitations or boundary conditions imposed by the modal shaker, strain-based measurements confirmed strong representation of all but one numerically predicted mode.

The fabricated model therefore demonstrates that the proposed methodology enables construction of a model, capable of reproducing the intended global dynamic behaviour, with acceptable accuracy under harmonic excitation.

The study further provides practical insight into the use of segmented, additively manufactured polymer beams as a controllable stiffness source within a response-based design framework. Limitations are identified and targeted refinements are proposed, establishing a structured basis for development of more robust beam geometries and connection strategies in future investigations. In addition, the dynamic behaviour of Tough2000 as a material for elastic model construction is characterised.

Although slamming experiments were out of scope for the presented study, the construction and validation of the globally flexible model provide a necessary foundation for such investigations. They identify the additional analyses required before suitability for transient slamming experiments can be conclusively established.

In conclusion, despite the identified uncertainties, the present work represents a methodological step toward integrating impulsive loading on cylindrical members, with incorporated global structural compliance, within a single experimental framework. By lowering the practical barrier to testing compliant *Merganser*-like platforms, the methodology enables further investigation of slamming-induced structural response. Given the design-driving nature of slamming loads for such systems, improved understanding of the associated response mechanisms holds clear engineering relevance.

Acknowledgements

This project was carried out as a collaboration between TU Delft and SolarDuck. I would like to sincerely thank everyone who contributed, with special appreciation to the SolarDuck team, who made me feel part of the organisation from the very beginning. The engaging and insightful discussions consistently challenged me to think more deeply about the problem at hand. I am especially grateful to Apostolos Grammatikopoulos for his guidance and support. His encouragement to pursue more complete answers, together with his direction during challenging phases of the project, greatly strengthened this research.

References

[1] C. J. Ramanan, King Hann Lim, Jundika Candra Kurnia, Sukanta Roy, Bhaskor Jyoti Bora, and Bhaskar Jyoti Medhi. Towards sustainable power generation: Recent advancements in floating photovoltaic technologies. *Renewable and Sustainable Energy Reviews*, 194:114322, 2024.

[2] DNV GL. Dnvgl-rp-c205: Environmental conditions and environmental loads, 2017. Recommended Practice.

[3] Y. Goda, S. Haranaka, and M. Kitahata. Study on impulsive breaking wave forces on piles. Technical Report 6, Port and Harbour Technical Research Institute, 1966. In Japanese.

[4] J. Wienke and H. Oumeraci. Breaking wave impact force on a vertical and inclined slender pile—theoretical and large-scale model investigations. *Coastal Engineering*, 52(5):435–462, 2005.

[5] Bo Terp Paulsen et al. Probabilistic assessment of wave impact loading on offshore structures. *Coastal Engineering*, 147:138–151, 2019.

[6] Yuxiang Ma, Bing Tai, Botao Xie, Tiaojian Xu, Marc Perlin, and Guohai Dong. Progress in the research of wave slamming forces on vertical cylinders. *Journal of Marine Science and Application*, 22:1–13, 2023.

[7] Apostolos Grammatikopoulos. A review of physical flexible ship models used for hydroelastic experiments. *Marine Structures*, 90:103436, 2023.

[8] CHEN Chaohe. JIAO Jialong, REN Huilong. Model testing for ship hydroelasticity: A review and future trends. 2017.

[9] Odd Magnus Faltinsen. Hydroelastic slamming. *Journal of Marine Science and Technology*, 6(2):49–58, 2001.

[10] Hui Sun and Odd M. Faltinsen. Water impact of horizontal circular cylinders and cylindrical shells. *Applied Ocean Research*, 28(5):299–311, 2006.

[11] Bjørn C. Abrahamsen, Frode Grytten, Øyvind Hellan, Tore H. Søreide, and Odd M. Faltinsen. Hydroelastic response of concrete shells during impact on calm water. *Journal of Fluids and Structures*, 116:103804, 2023.

[12] Winkler S. Davis M. Holloway D. Matsubara S. Lavroff j. French B. Thomas, G. Slam events of high-speed catamarans in irregular waves. *Journal of Marine Science and Technology*, 16:6–21, 2011.

[13] Adolfo Marón and Geert Kapsenberg. Design of a ship model for hydro-elastic experiments in waves. *International Journal of Naval Architecture and Ocean Engineering*, 6:1130–1147, 2014.

[14] Daniele Dessi and Elena Ciappi. Slamming clustering on fast ships: From impact dynamics to global response analysis. *Ocean Engineering*, 62:110–122, 2013.

[15] Ingo Drummen. *Experimental and Numerical Investigation of Nonlinear Wave-Induced Load Effects in Containerships Considering Hydroelasticity*. Phd thesis, Norwegian University of Science and Technology (NTNU), 2008.

[16] Jason Lavroff, Michael R. Davis, Damien S. Holloway, and Giles Thomas. The whipping vibratory response of a hydroelastic segmented catamaran model. In *Proceedings of the 9th International Conference on Fast Sea Transportation (FAST 2007)*, pages 600–607, Shanghai, China, 2007.

[17] Apostolos Grammatikopoulos, Joseph Banks, and Pandeli Temarel. The design and commissioning of a fully elastic model of a uniform containership. *Marine Structures*, 78:103014, 2021.

[18] Yingying Chen, Shanli Zhang, Wei Kean Chen, and Allan Magee. Design, construction and testing of a fully elastic ship model for investigating hydro-elastic responses of container ships. *Marine Structures*, 98:103663, 2024.

[19] Apostolos Grammatikopoulos, Joseph Banks, and Pandeli Temarel. Prediction of the vibratory properties of ship models with realistic structural configurations produced using additive manufacturing. *Marine Structures*, 73:102801, 2020.

[20] Ocid Mursid, Erkan Oterkus, and Selda Oterkus. Coupled ship simulation in hydrodynamics and structural dynamics induced by wave loads: A systematic literature review. *Journal of Marine Science and Engineering*, 13(3), 2025.

[21] Cristina Espinar, María M. Pérez, Rosa Pulgar, Alberto Leon-Cecilla, Modesto T. López-López, and Alvaro Della Bona. Influence of printing orientation on mechanical properties of aged 3d-printed restorative resins. *Dental Materials*, 40:756–763, 2024.

[22] Liam O'Connor. Comparative analysis of the mechanical properties of fdm and sla 3d printed components. *Journal of Micromanufacturing*, 0(0):25165984251364689, 0.

[23] Carmela Riccio, Marco Civera, Oliver Grimaldo Ruiz, Perla Pedullà, Mariana Rodriguez Reinoso, Giulia Tommasi, Martina Vollaro, Vito Burgio, and Cecilia Surace. Effects of curing on photosensitive resins in sla additive manufacturing. *Applied Mechanics*, 2(4):942–955, 2021.

[24] Formlabs Inc. Tough 2000 resin technical data sheet, 2020. FLTO2001, Rev. 01.

[25] E. Loukogeorgaki, C. Stergiopoulou, and N. Karaloulis. "Dry" and "wet" mode superposition approaches for the hydroelastic analysis of floating structures. *Applied Ocean Research*, 47:273–286, 2014.

[26] Ingo Drummen and Andreas Holtmann. Benchmark study of slamming and whipping. *Ocean Engineering*, 86:3–10, 2014.

[27] Formlabs Inc. *Tough 2000 Resin V2 Technical Data Sheet*. Formlabs Inc., 10 2025. Engineering Resin. Prepared 10/06/2025.

Appendix A. Material validation: specimen tests

The dynamic material validation methodology proposed by Grammatikopoulos et al. (19) was adapted in several respects for the present study. In contrast to the approach adopted by Grammatikopoulos et al., in which the specimen length was varied, the present study varied the wall thickness of the specimens. This choice was motivated by the absence of a sufficiently reliable adhesive joining technique at the time of testing and allowed the influence of thickness variations on the identified dynamic response to be assessed directly.

In addition, the specimens were intentionally designed with a non-square cross section. Preliminary numerical modelling indicated that the mass of the accelerometers would reduce the bending frequency of the instrumented side. If bending about both principal axes were captured simultaneously during testing, this effect would complicate modal identification and interpretation. By employing a non-square cross section, the bending stiffness differed between the two principal axes, resulting in well separated bending frequencies. This enabled unambiguous identification of individual modes while also allowing the specimens to be tested about two orthogonal axes, thereby increasing the amount of usable data obtained from each specimen.

Two commercially available photopolymer resins produced by Formlabs were considered during the material selection phase, their respective post curing material properties are summarised in Table A.22. Clear Resin was investigated due to its comparatively high stiffness, while Tough2000 was selected as it is marketed by the manufacturer as the strongest available engineering resin.

Appendix A.1. Specimen design

The two specimen geometries investigated are illustrated in Figure A.47 and summarised in Table A.21. The specimen length was selected based on the maximum allowable height compatible with the available post curing equipment.

Appendix A.2. Specimen numerical prediction.

The numerical model of the beam specimen was developed in PyMAPDL using a shell based representation, following the modelling approach adopted by Grammatikopoulos et al. (19). The study showed that shell discretisation more accurately captures the dynamic behaviour of additively manufactured components than analytical beam models. The hollow rectangular cross section was represented by four shell surfaces corresponding to the side faces of the specimen. These surfaces were defined using four corner keypoints at the two end stations of the beam, after which each face was meshed with a uniform element size.

SHELL181 elements were employed for the discretisation, consistent with the approach adopted by Grammatikopoulos et al. (19). This choice was motivated by the thin to moderately thick nature of the beam walls and the need to retain through thickness effects, transverse shear deformation, and consistent representation of bending moments within each element. Alternative representations such as plate elements were therefore not suitable. The presence of accelerometers was modelled for different experimental configurations through the connection of MASS21 elements to the shell mesh using RBE3 type constraint relations at the corresponding accelerometer locations.

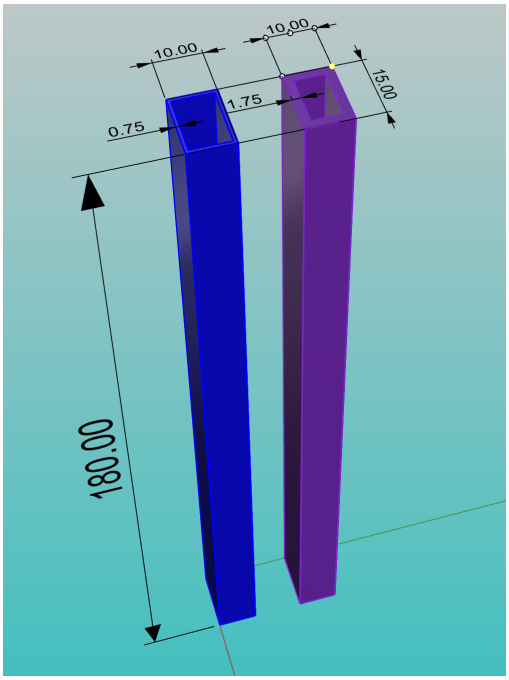

Figure A.47: Specimen dimensions.

A mesh convergence study was performed to evaluate the sensitivity of the predicted modal properties to the in-plane element size. The results indicate that the modal predictions are largely insensitive to mesh refinement, with differences of only $1-2\%$ observed between element sizes of 7 and 0.2 mm. The predicted natural frequencies for all four specimen are summarised in Table A.23.

Appendix A.3. Specimen testing

Figure A.48 presents the experimental set-up used for the dynamic testing of the printed material specimens. During testing, the sampling rate of all instruments was set to the maximum available frequency of 20 kHz. Each specimen was suspended using soft rubber bands to approximate free–free boundary conditions. Owing to the non-square cross section of the specimens, two testing configurations were applied in order to excite bending about both principal axes.

Three piezoelectric accelerometers (PCB 352C22) were used to measure the dynamic response of the specimens. The sensitivities of the accelerometers were 1.119, 1.108, and 1.130 mV/(m/s^2, respectively. Five discrete locations along the specimen length were defined at normalised positions Z_1 to Z_5, corresponding to 0/4, 1/4, 2/4, 3/4, and 4/4 of the total specimen length. For each test configuration, three accelerometers were mounted simultaneously at selected combinations of these locations. Two measurement sets were employed, with accelerometers positioned at (Z_1, Z_3, Z_5) and (Z_2, Z_3, Z_4), respectively. This ensured that both 2–node and 3–node bend-

Table A.21: Specimen geometry and derived sectional properties.

Specimen	L [mm]	b [mm]	h [mm]	t [mm]	A [mm^2]	EI [N m^2]	J [mm^4]	m/L [g/cm]
t0.75_clear	180	10	15	0.75	35.25	2.942	1109	0.35
t0.75_T2000	180	10	15	0.75	35.25	2.353	1109	0.35
t1.75_clear	180	10	15	1.75	75.25	5.469	1945	0.91
t1.75_T2000	180	10	15	1.75	75.25	4.375	1945	0.91

Table A.22: Post cured material properties used for numerical modelling, as reported by the manufacturer.

Property	Clear Resin V5	Tough 2000
Tensile modulus [GPa]	2.75	2.2
Flexural modulus [GPa]	2.70	1.9
UTS [MPa]	60	46
Density [g/cm^3]	1.21	1.21

Figure A.48: Specimen testing set-up example, Clear resin.

ing modes could be captured reliably. These two accelerometer layouts are referred to as the end configuration and the mid configuration, respectively.

The specimens were excited using a modal shaker (Dewesoft DS MS 100), applying a sine sweep excitation. The excitation range was set to $0 - 2000$ Hz to both bending modes. The excitation force was measured using a dynamic force sensor (Dytran 1051V1) mounted in line with the shaker stinger, with a nominal sensitivity of 112.4 mV/N. Petroleum wax was used to attach the force sensor to the specimen in order to provide sufficient stiffness while avoiding local stress concentrations.

A roving excitation procedure was adopted during the measurements. For a given accelerometer configuration, the specimen was excited sequentially from Z_1 to Z_5 in five consecutive runs. This procedure was repeated four times for a given configuration. After completing this sequence, the accelerometers were repositioned to the alternative configuration and the same procedure was repeated.

Appendix A.4. Post-processing

The measured force and acceleration time signals were transformed to the frequency domain using a Fast Fourier Transform (FFT) within the built-in Modal Test module in Dewesoft. Frequency response functions (FRFs) between the input force and each accelerometer were computed using the H1 estimator. For each run, the magnitude and phase of the FRFs, as well as the coherence, were extracted, as illustrated in Figure A.49. The coherence provides a measure of the linear correlation between the input and output signals and was used as an indicator of data quality over the frequency range of interest. In general, coherence values were found to be close to unity for all tests. Occasional drops in coherence were almost always associated with loss of adhesion of the petroleum wax used to mount either the accelerometers or the force sensor.

Natural modes were first identified by inspecting peaks in the FRFs in combination with corresponding local phase changes. Based on the measured FRFs, computation of the Complex Mode Indicator Function (CMIF) provided an additional indication of the presence and separation of natural modes, as shown by the cyan curve in Figure A.50. Final modal parameters were obtained using the stabilisation diagram, where poles were identified across increasing model orders. Stable poles, shown as green circles in Figure A.50, were selected based on consistency in frequency and damping as the model order increased. By varying the model order, a suitable balance between accurate modal identification and over-fitting of the data was achieved. Each selected pole represents a natural mode,

Table A.23: Predicted eigenfrequencies of the beam specimen manufactured from Clear Resin and Tough2000 at an element size of 1 mm.

Material	t [mm]	Bending A f_1 [Hz]	Bending B f_2 [Hz]	3–node Bending A f_3 [Hz]	Torsion f_4 [Hz]	3–node Bending B f_5 [Hz]
Clear Resin	0.75	686.5	1271.2	2053.8	3031.2	3135.2
	1.75	515.7	855.3	1610.9	2830.2	3004.0
Tough2000	0.75	619.7	1147.4	1853.9	2736.2	2830.0
	1.75	465.5	772.0	1454.1	2554.7	2711.6

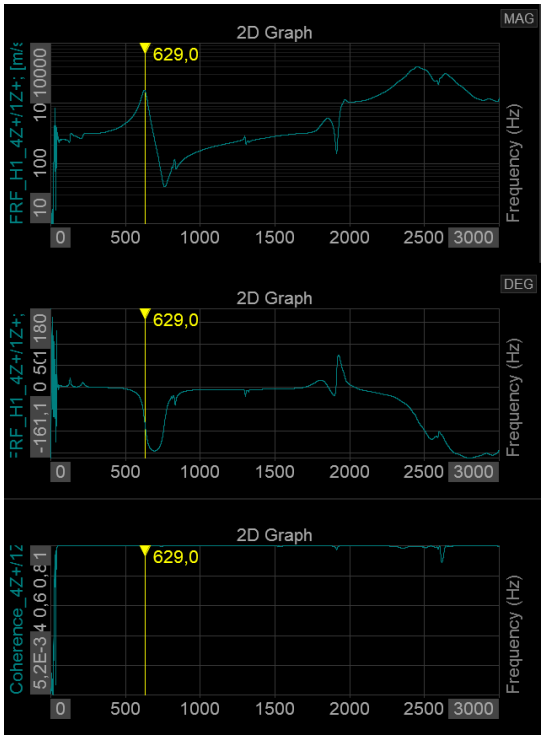

Figure A.49: Measured frequency response function magnitude, phase, and coherence from Dewesoft. t0.75A_CR

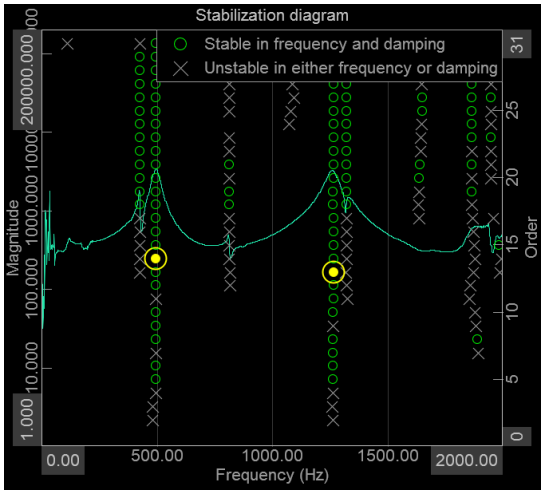

Figure A.50: Stabilisation diagram and Complex Mode Indicator Function obtained from Dewesoft modal analysis, t1.75A_T2000

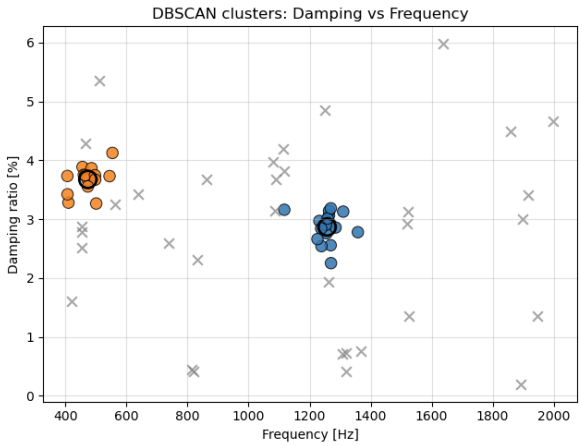

Figure A.51: DBSCAN results, t1.75A_T2000.

from which the mode number, natural frequency, damping ratio, and corresponding mode shape were exported for further post-processing.

Appendix A.4.1. DBSCAN clustering

To avoid subjective manual filtering of the data, and given the number of repeated test runs and excitation locations considered in this study, an automated post-processing procedure was required to consistently group modal identifications and quantify their scatter. To this end, a density-based spatial clustering (DBSCAN) algorithm was applied to the combined frequency and damping data. DBSCAN groups data points based on local density and does not require the number of clusters to be specified, which makes it suitable when the number of observable modes may vary between test conditions and when spurious identifications or noise points are present. The output of the clustering consists of a set of dense clusters representing repeatedly identified natural modes, as well as a set of noise points that do not belong to any cluster. An example of the resulting clustering is shown in Figure A.51.

The algorithm is defined by two main parameters. The parameter ε defines the neighbourhood radius in the two-dimensional frequency–damping space and therefore controls the maximum variation in identified modal parameters that is still considered representative of the same physical mode. The parameter n_{min} specifies the minimum number of data points that must be present within a neighbourhood for a cluster to be formed.

Table A.24: Comparison between experimentally observed and numerically predicted natural frequencies for the first bending modes of the Tough2000 specimens.

		Experimental				Numerical			
Conf.	Mode	f_{obs} [Hz]	σ_f [Hz]	ζ_{obs} [%]	σ_ζ [%]	E = 2.2 GPa [Hz]	Error [%]	E = 1.9 GPa [Hz]	Error [%]
End	1.75_A	465	55.5	3.79	0.31	462	-0.65	430	8.14
End	1.75_B	594	30.8	3.42	0.16	652	9.76	604	-1.66
End	0.75_A	438	51.5	4.84	0.60	473	7.99	439	-0.23
End	0.75_B	626.3	70.0	3.67	0.36	657	4.90	610	2.67
Mid	1.75_A	512.8	58.5	3.54	0.20	510	-0.55	474	8.19
Mid	1.75_B	664	38.5	3.97	1.02	719	8.28	661	0.45
Mid	0.75_A	467.7	69.7	3.86	0.71	536	14.60	498	-6.08
Mid	0.75_B	619	10.6	3.31	0.17	744	20.19	686	-9.77

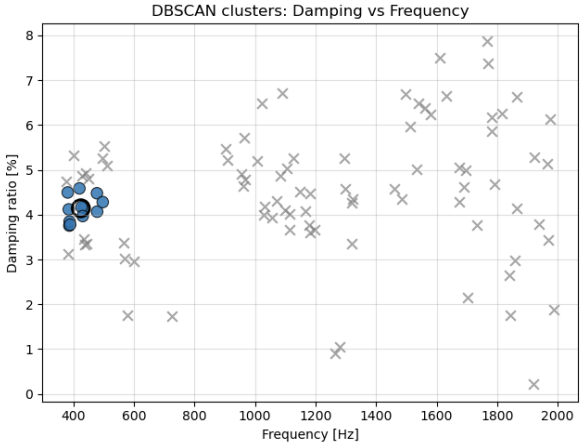

Figure A.52: DBSCAN clustering results, t1.75A_CR.

Appendix A.5. Specimen test results

From the material testing, Tough2000 observed higher consistency of its dynamic response. For the Clear Resin specimens, standard deviations in the identified 2–node bending frequencies were consistently larger, by a factor of approximately 1.1–1.3, than those observed for Tough2000. In addition, while higher order mode could occasionally be identified for the Tough2000 specimen when excited at locations Z_2 or Z_3, for the Clear resin specimens these observations were frequently inconsistent, showed unreasonably high standard deviation within clusters or were entirely absent, as illustrated by the dispersed clustering behaviour shown in Figure A.52. These observation are in line with the manufacturer's classification of Tough2000 as an engineering resin. For these reasons, Tough2000 was selected as the most suitable resin for further consideration. The detailed statistical comparison is therefore limited to Tough2000. The resulting comparisons are summarised in Table A.24.

Besides selection of a suitable resin, an objective of the specimen testing was to identify resin behaviour by iteratively tuning the material properties such that numerical predictions matched experimentally observed natural frequencies for 2–node bending, following the approach proposed by Grammatikopoulos et al.

In principle, this procedure relies on the ability to identify the natural mode consistently across repeated runs, excitation locations, and sensor configurations. In the present measurements however, this tuning method could not be executed properly. As highlighted in Table A.24, the sensitivity of the results to both material properties and test configuration was too pronounced.

Standard deviations in the observed natural frequencies are on the order of 30 – 70 Hz, corresponding to relative variations of approximately 6 ˘ 15%. These variations are of the same order of magnitude as the frequency shifts induced by changing the Young's modulus in the numerical model from 1.9 to 2.2 GPa. As a result, attempts to iteratively tune the material properties to achieve agreement across multiple test configurations were inherently ambiguous. Additionally, it was observed that improving the agreement for one test configuration would simultaneously degrade the agreement for another.

Multiple factors are believed to have contributed to this, one of which is the added mass and stiffness of the accelerometers and attached cables. The influence of the accelerometer configuration is evidenced by the pronounced differences in both numerically predicted and experimentally observed natural frequencies between the end and mid configurations shown in Table A.24. Although efforts were made to minimise cable influence by supporting their weight independently of the specimen, repeated repositioning of the shaker during sequential runs often required reattachment of sensors or adjustment of cable routing. These inconsistencies combined with known influence of the accelerometers are therefore considered to have contributed to the variability observed in the identified natural frequencies and damping ratios.

Additionally, the excitation location was found to affect the identified modes. For the first bending mode, the absence of a clear response when the specimen was excited at Z_2 and Z_4 is expected, as these locations coincide with nodal positions of the 2–node bending mode. However, even when the same mode was excited away from nodal locations, the identified natural frequencies were not consistent. Excitation at the specimen ends (Z_1 and Z_5) yielded identified frequencies that differed by approximately 3 – 5% compared to excitation near mid-span (Z_3) for the same mode. This excitation-location dependence is also expected to have contributed to the dispersed damping ratios extracted from the measurements. An attempt was made to reproduce the influence of the shaker in the numerical model; however, no boundary condition formulation was found that could accurately reproduce the experimentally ob-

served behaviour.

Given the modelling uncertainties, no definitive conclusions can be drawn regarding the influence of specimen orientation or material thickness on the dynamic properties of the specimens. Across both accelerometer configurations however, the experimentally observed frequencies were consistently bounded by the numerical predictions obtained using Young's moduli of 1.9 and 2.2 GPa, with closer agreement generally observed for 1.9 GPa. As the dynamic response of both the test specimens and the final structural model is governed primarily by global bending, it is expected that the flexural stiffness provides the most representative description of the effective material behaviour. On this basis, a Young's modulus of 2.0 GPa was selected as a representative value for subsequent numerical analyses.

Appendix B. BEAM188 represented model

Appendix B.1. Space exploration for improved frequency matching

To investigate whether an idealised beam configuration could reproduce the targeted natural frequencies, an auxiliary numerical study was performed using BEAM188 elements. In this representation, each connecting beam between the floaters was replaced by a single BEAM188 element. The purpose of this exercise was not to obtain a manufacturable design, but rather to explore whether a beam within the admissible stiffness space could theoretically match the requested modal properties.

The sectional properties assigned to the BEAM188 elements were derived from the fully representative SHELL181 beam models. Specifically, the equivalent vertical bending stiffness EI and torsional rigidity GJ were extracted and used as input parameters. BEAM188 is formulated based on Timoshenko beam theory, thereby accounting for both bending and shear deformation. Torsional behaviour is represented through Saint Venant torsion using the specified torsional constant J, allowing coupled bending and torsional response to be captured analytically within a one dimensional beam formulation. The obtained frequencies for the symmetric and asymmetric stiffness variations are summarised in Table B.25.

Table B.25: Frequency comparison between BEAM188 idealised representations and SHELL181 model [Hz]

Mode	Sym	75%	125%	SHELL181
1a	9.42	8.83	10.07	9.51
1b	9.47	9.82	10.25	9.53
2	12.44	12.10	13.12	13.24
3	22.50	21.81	24.21	17.67
4a	33.50	31.28	33.84	25.93
4b	34.12	33.65	36.59	25.94

The unaltered symmetric BEAM188 representation presented in the first column captures the global modal trends reasonably well, particularly for the lower modes. More notably, the corresponding mode shapes exhibited immediate convergence toward the same floater rotation patterns as observed in the SHELL181 model.

This behaviour indicates that for a three beam axially symmetric configuration, the global deformation patterns are primarily governed by geometric symmetry and overall stiffness ratios rather than detailed sectional distribution. In other words, once the structure satisfies the symmetry and connectivity conditions, the modal deformation shapes are strongly constrained by structural topology. Variations in stiffness predominantly shift the natural frequencies, while the underlying global rotation patterns remain invariant.

To investigate whether a combination of bending stiffness and torsional rigidity could reproduce the requested spacing of natural frequencies, the BEAM188 section properties were systematically scaled. The equivalent bending stiffness EI and torsional rigidity GJ were multiplied by factors within a prescribed range, thereby defining a two dimensional stiffness parameter space. The purpose of this exploration was to determine whether an idealised beam, unconstrained by manufacturability, could match the targeted frequency spacing obtained from the optimisation of the full model.

Within this defined stiffness space, no combination of parameters was found that allowed exact alignment of the scaled Merganser platform frequencies. While individual frequencies could be shifted through stiffness scaling, the relative spacing between modes remained constrained. In particular, reducing the torsional constant J by several orders of magnitude did not produce the required separation between bending and torsion dominated modes.

This behaviour is explained by the coupled nature of the global deformation patterns. The nominally torsion dominated mode induces 3-node bending deformation along the beams. As a result, the associated natural frequency is not governed solely by GJ, but by a combination of bending and torsional stiffness contributions. Consequently, bending and torsional frequencies cannot be tuned independently in this three beam symmetric configuration.

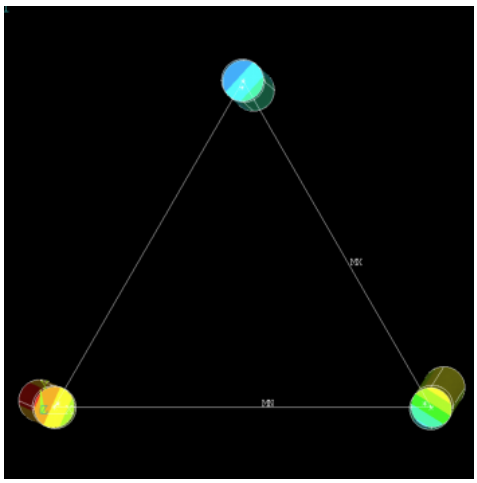

Figure B.53: BEAM188 representation Mode 1a.

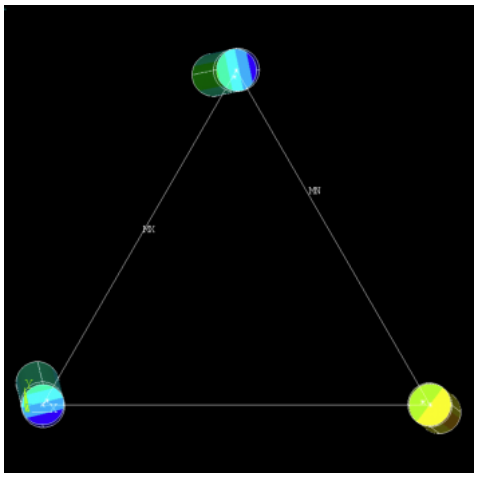

Figure B.54: BEAM188 representation Mode 1b.

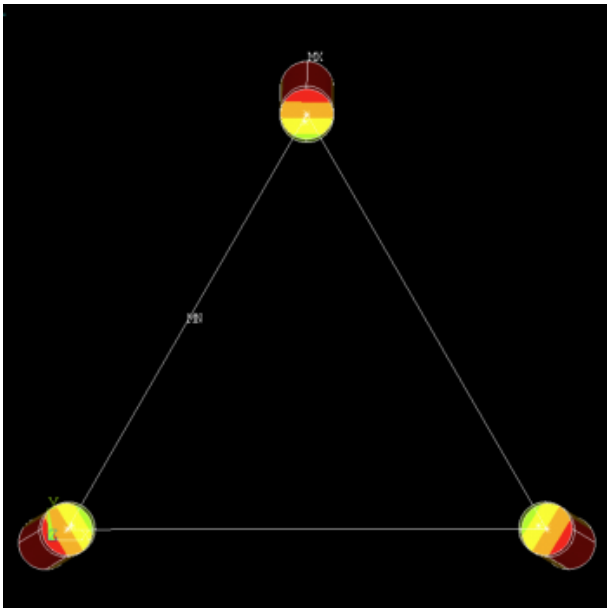

Figure B.55: BEAM188 representation Mode 2.

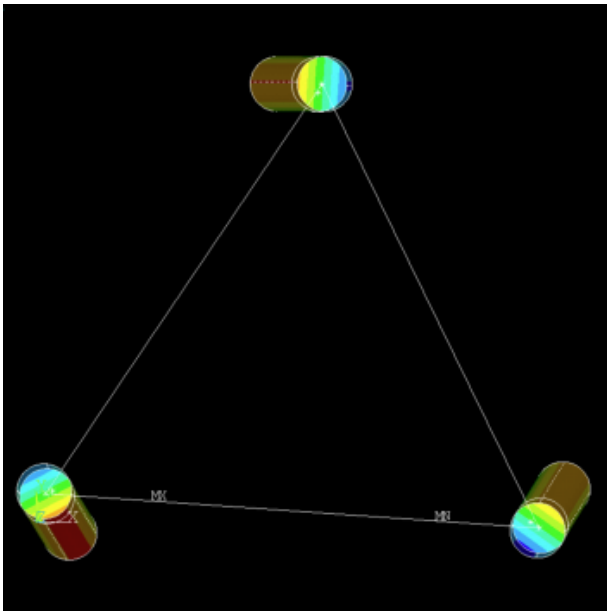

Figure B.56: BEAM188 representation Mode 3.

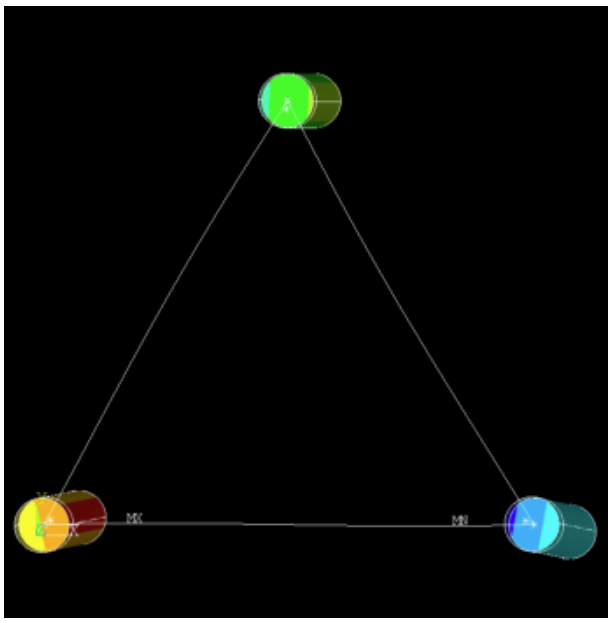

Figure B.57: BEAM188 representation Mode 4a.

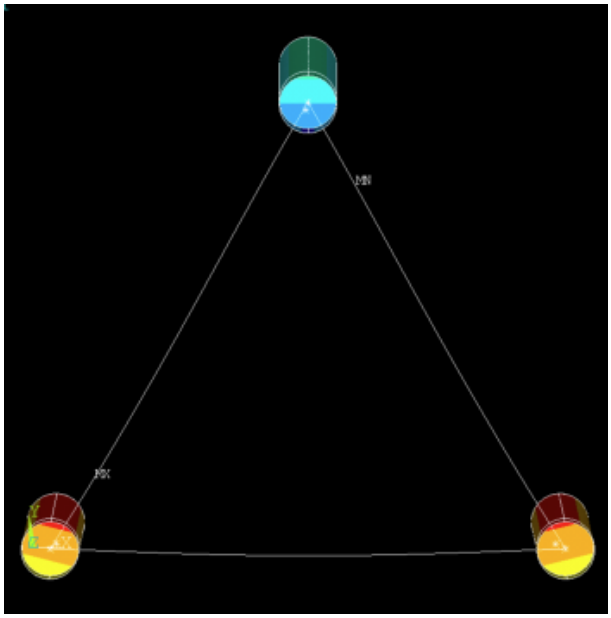

Figure B.58: BEAM188 representation Mode 4b.

Appendix C. Rigid floater modelling

The minimum required stiffness of the floaters was assessed based on two considerations. Both considerations are formulated as estimates intended to guide the structural design, rather than as strict dynamic criteria.

Appendix C.1. Separation from Global Platform Modes

The floaters are intended to behave as rigid bodies within the global hydroelastic response of the platform. To limit potential modal interaction between local floater deformation modes and global structural modes, sufficient separation between their respective natural frequencies is desirable.

To reduce the likelihood of modal interaction, it was considered desirable that the lowest natural frequency of the floater exceeds the highest predicted global platform mode by approximately one order of magnitude. For this reason, the targeted lowest floater frequency was set to a minimum of 176.9 Hz.

Appendix C.2. Relation to Slamming Duration

The second consideration relates to the possibility of local hydroelastic response during slamming. As the intended use of the model is the investigation of the global structural response to a slamming event, it was deemed necessary to prevent possible dynamic amplification effects at floater scale from influencing the measured response.

Dynamic structural effects become relevant when the structural natural period approaches the characteristic impact duration (9). In order to determine the range of floater natural frequencies for which such effects could influence the intended slamming tests, the slamming duration was estimated using the analytical formulation of Wienke and Oumeraci (4). For an oblique impact, the total impact duration is given by

$$T_s = \frac{13}{32}\frac{R}{V\cos\gamma}$$

where R is the cylinder radius, V is the impact velocity, and γ is the impact angle.

For the present configuration, a water depth of $h = 30$ m was considered representative for the intended site of the *Merganser* platform. Under shallow water assumptions, the impact velocity was approximated as

$$V = \sqrt{gh}$$

which results in $V \approx 17.15$ m/s. For $R = 2.25$ m and $\gamma = 0$, the resulting slamming duration becomes

$$T_s \approx 0.053 \text{ s}$$

which corresponds to a characteristic slamming frequency defined as

$$f_s = \frac{1}{T_s} \approx 18.77 \text{ Hz}.$$

Scaling to model scale yields a corresponding slamming frequency of approximately 83.95 Hz. This value neglects potential rigid body motion of the platform in the opposite direction of impact.

Appendix C.3. Implications for Floater Design

As the model was constrained in the total allowable mass, materials such as aluminium extrusion could not be used. Lighter and equally stiff materials such as carbon composites were not commercially available at the required diameter within the time frame of this research.

The most suitable material balancing stiffness and mass was identified as a commercially available PMMA extrusion with an outer diameter and a wall thickness of 3 mm. Numerical modal analyses was performed to assess the clamped free deformation behaviour of this extrusion when modelled with closed ends. The first global bending mode was identified at approximately 143 Hz, while the first in plane cross sectional deformation mode occurred at approximately 243 Hz. The corresponding deformed shapes are presented in Figure C.59.

Further analyses indicated that increasing the height of the top inserts, which were approximated as rigid in the numerical model, effectively reduced the free span of the floater. As a result, the corresponding global bending and cross sectional deformation frequencies increased to approximately 188 Hz and 312 Hz, respectively.

The dry natural frequency of 188 Hz exceeds the scaled slamming frequency estimate of 83.95 Hz. However, the floater modal analysis was performed under dry conditions. In reality, hydrodynamic added mass will reduce the natural frequency. In addition, coupling with the global platform may influence slamming durations, for example through rigid body motion prior to impact or through global structural effects.

For this reason, the stiffness design was approached conservatively. The floaters were constructed as stiff as reasonably achievable within material and manufacturing constraints. Further stiffening would have required significantly thicker shells or alternative materials, both of which were incompatible with geometric scaling, total mass constraints, and manufacturing limitations.

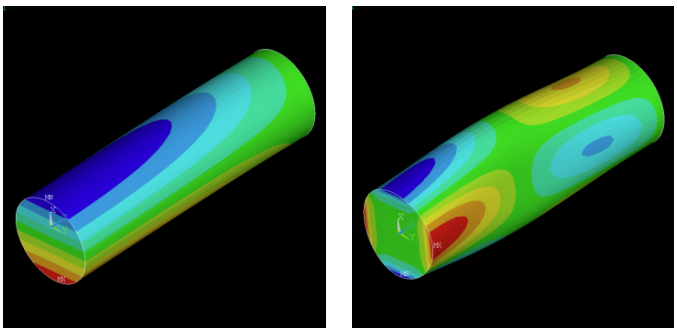

(a) First global bending mode (b) First in plane deformation mode

Figure C.59: Numerically predicted deformation modes of the PMMA floater, colours denote z-translation.

Appendix C.4. BFI modelling

In addition to stiffness requirements, mass constraints played a significant role in the design of the beam floater interface. It was apparent that the total platform mass would likely exceed the correctly scaled target value. The beam floater interface could therefore not be over-dimensioned indiscriminately, and stiffness had to be achieved in a weight-efficient manner.

To meet these requirements, a circular PLA-CF printed geometry was adopted, reusing the same inner ring and stiffener concept applied in the top insert design. In order to mobilise as much material as possible, the fastening method was designed such that the bolts passed through both the inner and outer rings. The diameter and circumferential spacing of the fasteners were selected such that the resulting bending stiffness of the bolted connection exceeded that of the beam cross section, providing a conservative design requirement.

An initial test construction of the beam floater interface with a nominal thickness of 2 mm revealed that achieving sufficient bending stiffness constituted the primary design challenge. When subjected to torsional loading, the assembly remained effectively rigid even under load levels sufficient to induce substantial deformation in the beam itself. Under bending loading, however, visible deformation of the beam floater interface was observed while the beam remained comparatively un-deformed.

Appendix C.4.1. beam floater interface modelling

Creation of a model which could accurately capture all behaviour would be difficult. Predominantly because the interaction between the outer beam and the bolted interface would introduce a complex combination of contact, friction, and local stress redistribution within a non-isotropic printed material. Therefore, prior to developing a representation of the full beam floater interface, a simplified representation of the intended design was constructed, enabling a numerical sensitivity study to systematically explore and bound the relevant design space.

The simplified numerical model is presented in Figure C.60a. In this representation, a single beam end was modelled with the outer beam end cap as a rigid area between two stiffeners. The presence of the M6 bolts was represented using BEAM188 connections between the inner and outer ring regions. The bottom row of nodes was fully constrained to represent the solid bottom cap of the beam floater interface, which would be bolted to the top insert. To obtain a conservative estimate of interface deformation under loading, this assembly was subjected to a static vertical load of 50 N applied at a distance L_b. The assessed geometry and loading configuration are illustrated in Figure C.60b.

The mean nodal rotation of the rigid outer beam cap, ϕ_{cap} was assessed as a function of the thickness of the stiffeners and ring regions, denoted by t_c, and the inner ring radius R_i. The results of this analysis are presented in Figure C.62a.

Inspection of the internal load paths revealed that a portion of the beam floater interface remained weakly loaded under the applied bending configuration. To exploit this observation and reduce structural mass, a parametric cut plane was introduced

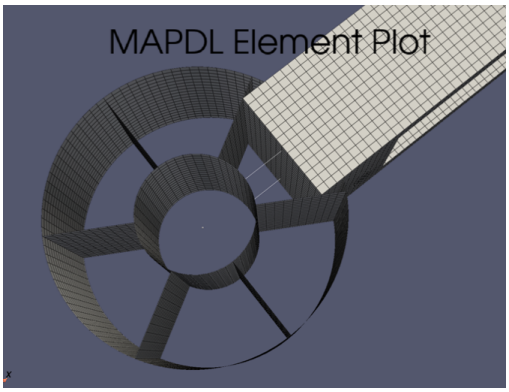

(a) Element representation of the beam end model.

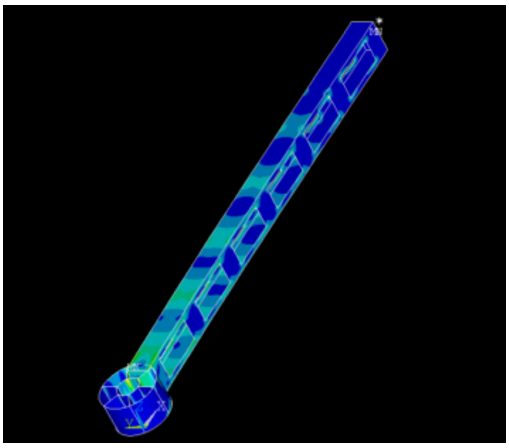

(b) Equivalent strain response from static loading.

Figure C.60: Beam end modelling approach and corresponding static strain verification.

to selectively remove material from this region. The cut plane geometry was defined using two non-dimensional parameters, illustrated in Figure C.61. The parameter α_h denotes the relative intersection height at the outer side of the component (green line), while α_w denotes the relative intersection width at the top surface (red line). The results of the parametric sweep are presented in Figure C.62b.

The parametric sweeps showed that the beam end cap rotation was weakly dependent on the inner ring radius, while exhibiting a strong but decreasing dependence on the local material thickness, with diminishing stiffness gains observed beyond a thickness of approximately 5 mm. The cut–away study further showed that material removal at larger values of the height parameter α_h had a limited effect on bending stiffness, whereas increases in the width parameter α_w, corresponding to material removal closer to the load introduction region, led to a stronger stiffness reduction.

The nominal thickness was capped at 5 mm to limit mass. To accommodate rings within the PLA–CF material, local reductions in thickness were introduced where required. In total, approximately 30% of the material volume was removed relative to a configuration without material removal. The bottom plate comprised a 3 mm thick solid plate, with extrusions positioned

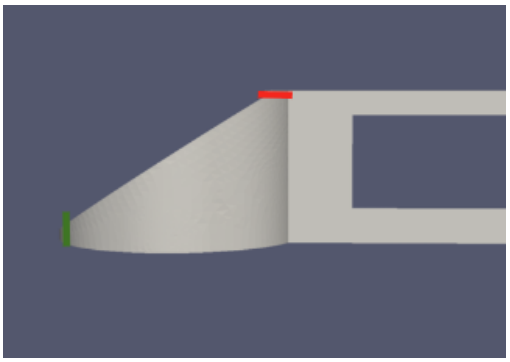

Figure C.61: Cut plane parameter definition.

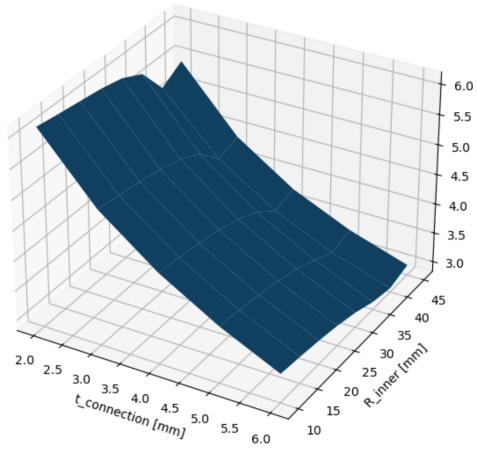

(a) Outer beam cap rotation (ϕ_{cap}, t_c, R_i) [1×10^{-5} rad]

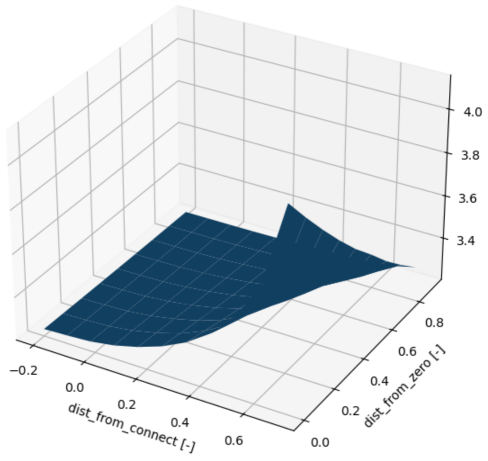

(b) Outer beam cap rotation (ϕ_{cap}, α_w, α_h) [1×10^{-5} rad]

Figure C.62: Parametric sensitivity of outer beam cap rotation.

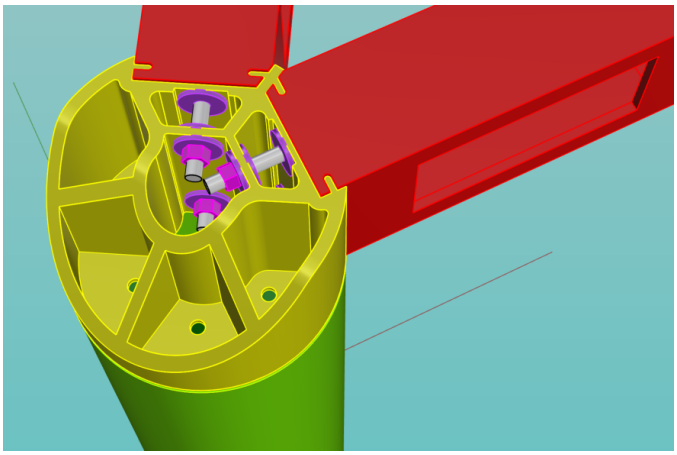

Figure C.63: Final geometric design of the beam floater interface as implemented in the physical model.

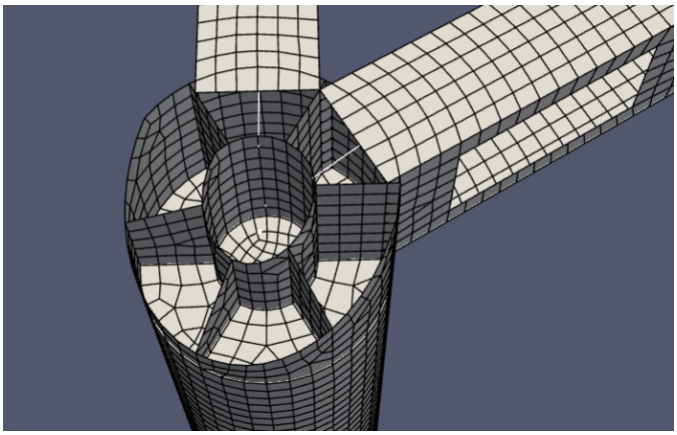

Figure C.64: Simplified numerical representation of the beam floater interface used for the parametric stiffness study.

at fastener locations.

The component was test–printed prior to final assembly and loaded in combination with a representative beam section. In contrast to earlier prototype iterations, no noticeable deformation of the beam floater interface was observed, with deformation instead occurring predominantly in the beam itself.

The numerical representation was subsequently extended to the as–constructed full corner assembly shown in Figure C.64 and implemented in the global numerical modal analysis. This refinement resulted in a shift in the predicted natural frequencies, on the order of 0.1 Hz. Given the number of modelling assumptions inherent to the connection representation, the predictive value of the observed frequency shift is limited. However, as the use of a conservative static load level of 50 N resulted in only limited deformation for a thickness of 5 mm. Together with the experimental observations obtained from the test prints, this provides a high degree of confidence that the manufactured beam end assemblies behave effectively as rigid connections within the frequency range of interest.

Appendix D. Static Flexural modulus determination

Appendix D.1. Finite element model for static strain prediction

The same FEM modelling techniques as used for the beams in the assembled model was used for the static strain prediction. The beams were discretised using SHELL181 elements, consistent with the modelling strategy adopted for the global modal analysis. The mesh size was set to 4.4 mm for the static predictions. To represent the physical beams, 10 mm thick endcaps were included at both beam ends using SHELL181 elements.

Boundary conditions were applied according to the experimental configuration. Depending on the test case, simply supported (SS), clamped–free (CF), or clamped–clamped (CC) constraints were imposed using direct displacement constraints on the corresponding end nodes. For clamped conditions, both translational and rotational degrees of freedom were restrained. For simply supported conditions, vertical translations were constrained while allowing rotational freedom about the bending axis.

Static loads were introduced as concentrated forces applied at the designated loading positions, consistent with the experimental procedure. The resulting strain fields along the beam surface were extracted at the gauge locations and used for direct comparison with the creep corrected experimental measurements described in the subsequent sections.

An example of the numerically predicted equivalent strain distribution for the SS_o configuration is shown in Figure D.65. The corresponding out of plane translation field in global z direction is depicted in Figure D.66.

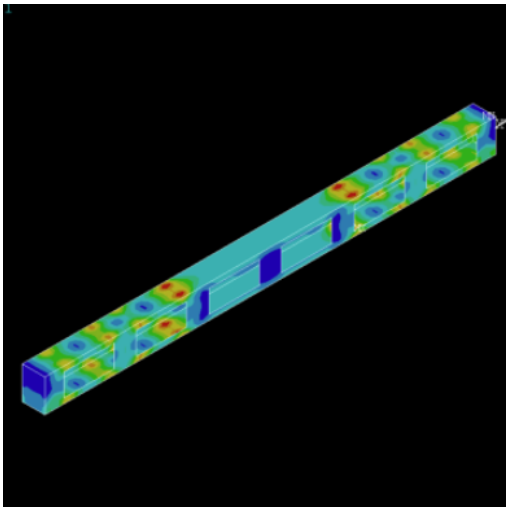

Figure D.65: Example equivalent strain distribution for SS_o configuration.

Appendix D.2. Post processing procedure

This appendix describes the post processing workflow applied to the static strain gauge measurements obtained during the static loading tests. The complete static testing procedure, including the employed setups and loading configurations, is described in Chapter 5.

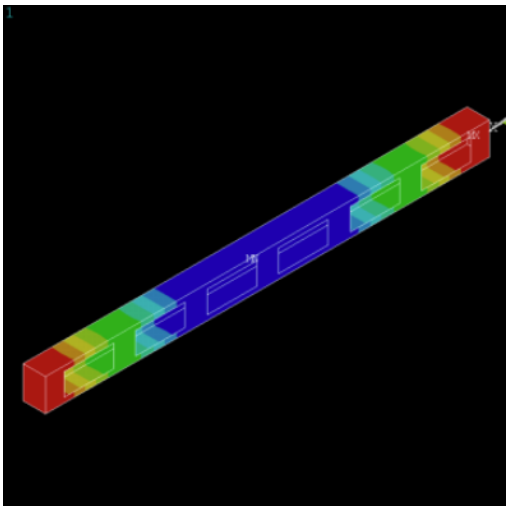

Figure D.66: Example global z translation field for SS_o configuration.

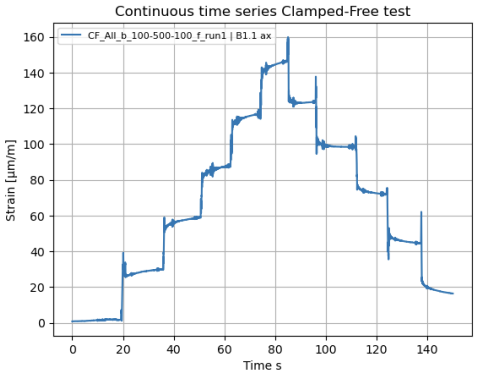

Figure D.67: Example time series data.

Appendix D.3. Creep Behaviour and Motivation for Correction Procedure

During the initial static tests it was observed that the measured strain levels exhibited time dependent creep under sustained loading, this behaviour can be observed from the raw time series data presented in Figure D.67. Between sharp transitions where the beam was loaded or unloaded, strain clearly depicts a non-continuous behaviour.

To quantify this behaviour, a dedicated creep assessment trial was conducted. The results are shown in Figure D.68. In this trial, the fully assembled model was subjected to the outer loading configuration with a total applied mass of 2000 grams. The load was maintained for approximately 12 minutes, after which it was fully removed in order to observe the recovery behaviour of the material. As shown in Figure D.68, a continuous increase in strain is observed during the static loading phase, despite the applied load remaining constant. This confirms the presence of primary creep during the load plateau. After removal of the load, the strain did not instantaneously return to its original value. Instead, a gradual recovery was observed, with the initial strain level only being re established after approximately 10 minutes.

This behaviour is consistent with the technical data sheet

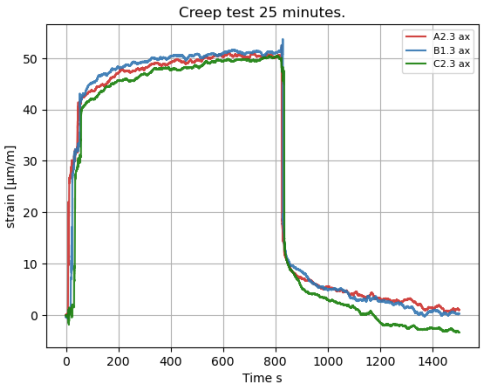

Figure D.68: Measured strain response during a 25 minute creep trial under 2000 gram loading, followed by unloading.

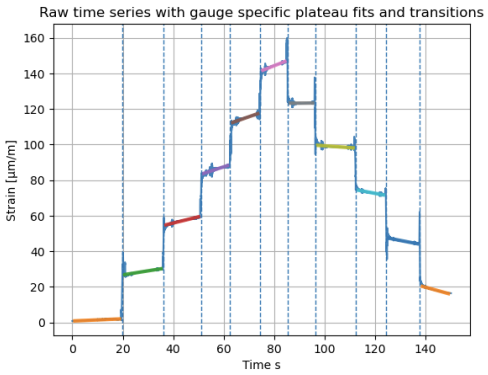

Figure D.69: Linearised plateaus during loading steps

provided by the material manufacturer for Tough 2000 Resin V2 (27). The flexural creep results reported in the data sheet, obtained according to ISO 6602 at 22 °C under a constant stress of 4.0 MPa, indicate a creep strain of approximately 1.25% after 14 days of sustained loading. Importantly, the creep curve shown in the data sheet demonstrates that the initial rate of deformation is significantly higher during the early stages of loading, after which the strain increase gradually reduces over time.

Although the duration of the static validation tests in the present study is considerably shorter than the 14 day period reported in the data sheet, the pronounced initial creep rate observed in the manufacturer data explains the measurable time dependent strain drift during the static load plateaus.

The objective of the post processing procedure is therefore not to explicitly quantify the creep of the material but rather to transform the raw time domain strain signals into creep corrected and symmetrically paired strain values. These processed strain levels provide a stable and reproducible representation of the static structural response and enable a direct comparison with the deterministic numerical predictions.

Appendix D.4. Transition detection and plateau segmentation

To automatically identify the individual load steps within the static tests, a step detection algorithm is applied to the filtered strain signal. First, a rolling median filter is used to suppress high frequency noise while preserving the stepwise structure of the signal. A step metric is then computed based on the difference between the medians of left and right moving windows. Peaks in this metric that exceed a prescribed threshold are identified as load transitions. A minimum separation criterion is enforced to prevent double detection of a single transition. The resulting transition indices divide the time series into consecutive load plateaus.

Using these detected transitions, the signal is segmented into individual plateaus, each corresponding to a constant load level. To avoid contamination by transient behaviour immediately after load application or removal, a fixed number of samples at both edges of each plateau are discarded. For each strain gauge and each plateau, A linear fit was applied to the plateau in order to characterise the time dependent strain evolution within the quasi static intervals, this is depicted in Figure D.69. From each linear interval the initial value of the plateau was observed as the recorded strain.

Appendix D.5. Creep correction and symmetric pairing

The applied loading sequence is symmetric. For a total of n plateaus, plateau i is paired with plateau $n + 1 - i$, resulting in load pairs with identical magnitude but opposite position in the loading sequence.

If paired values are combined without creep correction, a biased strain distribution is obtained. As shown in Figure D.70, plateaus corresponding to identical weights during loading and unloading do not coincide due to creep.

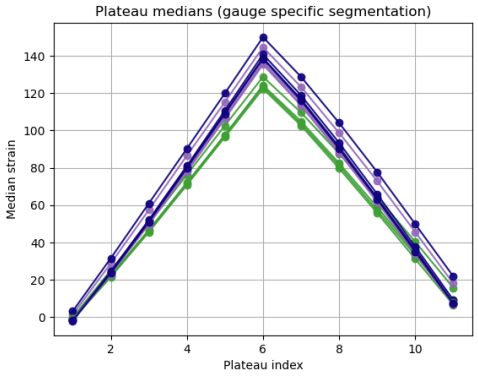

Figure D.70: Plateau median strain values prior to creep correction.

The creep contribution within each plateau is estimated from the product of the plateau duration and the fitted drift slope. An example of the measured drift slopes for three gauges in clamped free configuration is shown in Figure D.71. A clear trend is observed in which the magnitude of creep increases with increasing load level. This behaviour was consistent across all gauges and configurations.

The cumulative creep is obtained by summing the previously recorded creep contributions and subtracting this value from the initial value of each plateau. The resulting creep corrected values are shown in Figure D.72. After correction, loading and unloading plateaus corresponding to identical weights align more closely.

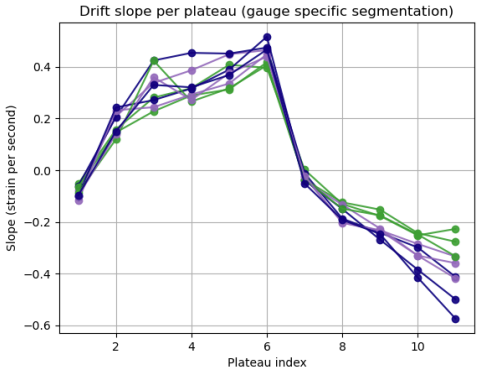

Figure D.71: Measured creep per plateau for representative gauges.

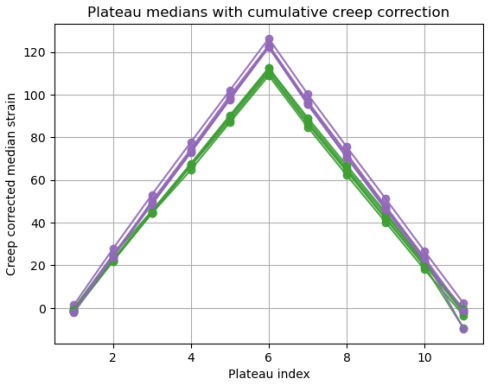

Figure D.72: Plateau medians after cumulative creep correction.

This procedure provides an efficient and robust method for compensating time dependent strain drift. Although minor misidentifications of plateau boundaries occasionally occurred, particularly for lower load levels, such cases were identified and excluded in subsequent post processing steps.

Appendix D.6. Flexural modulus identification by strain load curve fitting

The flexural modulus of Tough 2000 was identified by fitting finite element predictions to the experimentally measured strain response under static loading. For each instrumented segment and each experimental configuration, the creep corrected strain was plotted as a function of applied weight. An example for the clamped free configuration is shown in Figure D.73. Each coloured curve represents a different strain gauge location along the length of the three constructed beams.

The slope of each strain weight curve reflects the effective bending stiffness of the corresponding segment. Small variations between gauges indicate minor stiffness differences along the beam, which may arise from manufacturing tolerances or local geometric variations.

For each setup, strain curves were first averaged per gauge over repeated runs. The resulting experimental curves were then compared to finite element predictions generated for the corresponding boundary conditions and loading cases. The flexural modulus was treated as a fitting parameter and adjusted

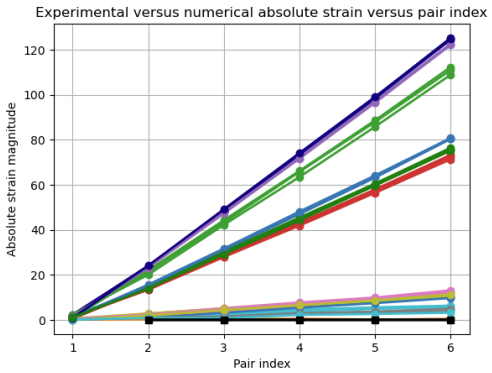

Figure D.73: Measured strain as function of applied weight for representative gauges in clamped free configuration.

such that the numerical strain weight curves best matched the experimental data.

The combined experimental and fitted numerical responses for all six configurations are shown in Figures D.74 to D.79. Each figure presents the comparison between measured and simulated strain responses across all gauges for a given setup. Numerical predictions are plotted with black dotted lines.

For each segment and configuration, an optimal flexural modulus was obtained through this fitting procedure. The identified values are summarised in Table 14 in Section 6.1.

Despite the systematic fitting procedure, it remained difficult to draw definitive conclusions regarding the static flexural modulus of Tough 2000 based solely on individual configurations. The creep correction procedure, although effective in most cases, was not fully robust. This created some noise which made the identification of minor variations between setups and between segments difficult.

A consistent pattern was nevertheless identified. Segments subjected to the highest pure bending moment, namely the middle segments during outer loading in the SS and CC configurations, and the segments closest to the clamped boundary in the CF configuration, systematically yielded the lowest fitted flexural modulus values. In these regions, strain levels were highest, reducing the relative influence of through-thickness effects. Furthermore, these locations most closely approximate pure bending conditions.

Based on this consistent behaviour across configurations, it is concluded that the static flexural modulus of Tough 2000 lies in the range of 1.9 to 2.0 GPa. A comparison between numerically predicted strain distributions, BEAM188 represented strain distribution and experimentally observed results are presented in Figures D.80 to D.84.

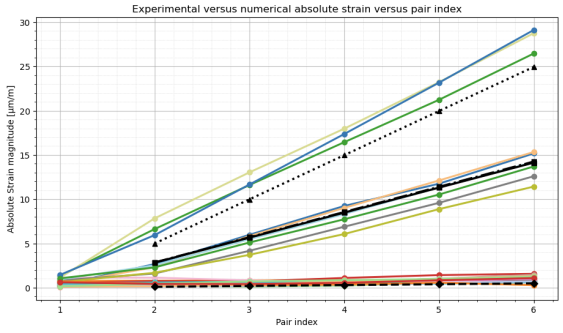

Figure D.74: Assembled configuration, middle loading position.

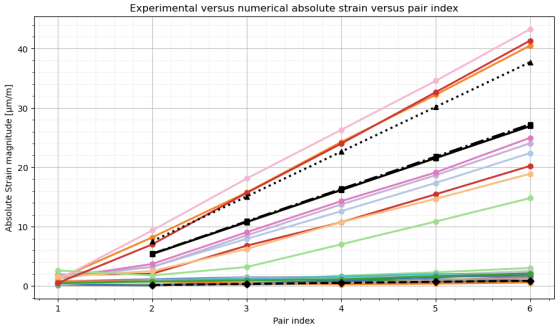

Figure D.75: Assembled configuration, outer loading position.

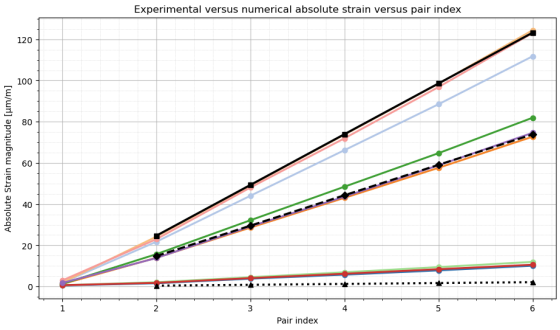

Figure D.76: Clamped free configuration, middle loading position.

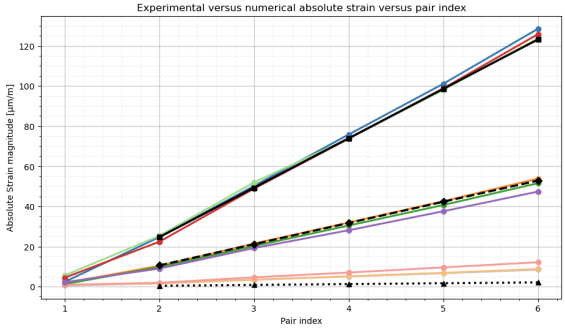

Figure D.77: Clamped free configuration, outer loading position.

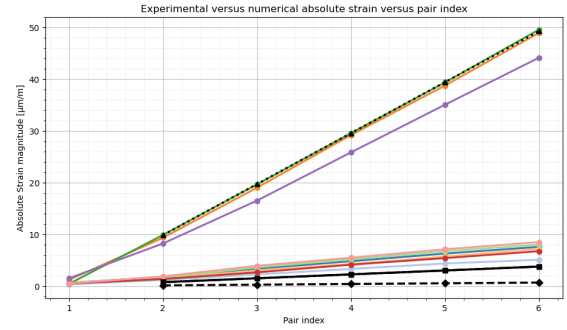

Figure D.78: Simply supported configuration, middle loading position.

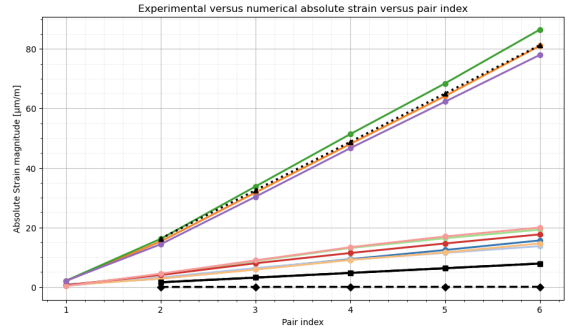

Figure D.79: Simply supported configuration, outer loading position.

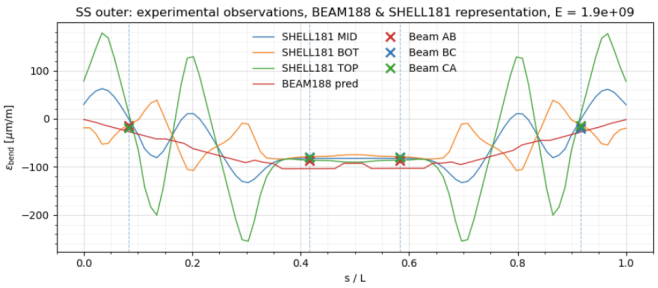

Figure D.80: Simply supported configuration, outer loading, $E = 1.9$ GPa.

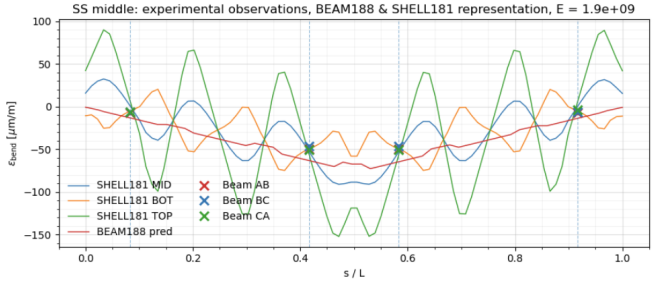

Figure D.81: Simply supported configuration, middle loading, $E = 1.9$ GPa.

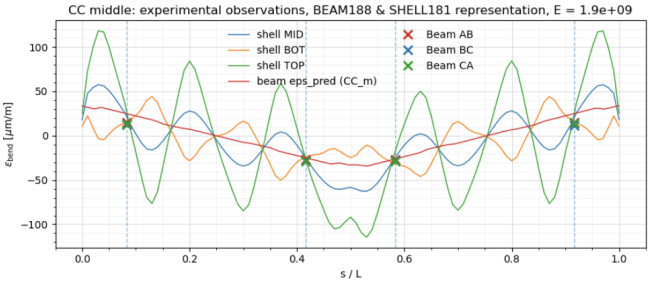

Figure D.82: Assembled configuration, middle loading, $E = 1.9$ GPa.

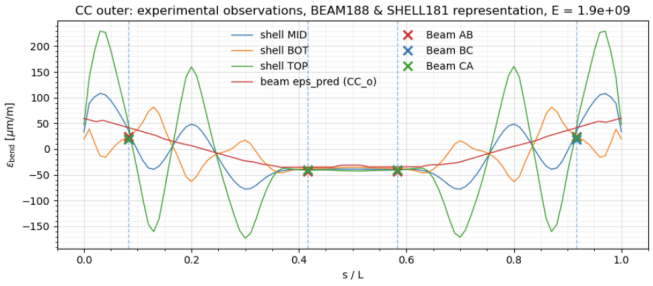

Figure D.83: Assembled configuration, outer loading, $E = 1.9$ GPa.

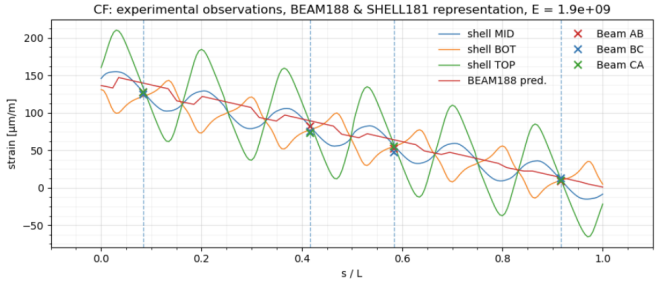

Figure D.84: Clamped free configuration, $E = 1.9$ GPa.

Appendix E. Dynamic Results

Appendix E.1. Close-ups observed mode clusters

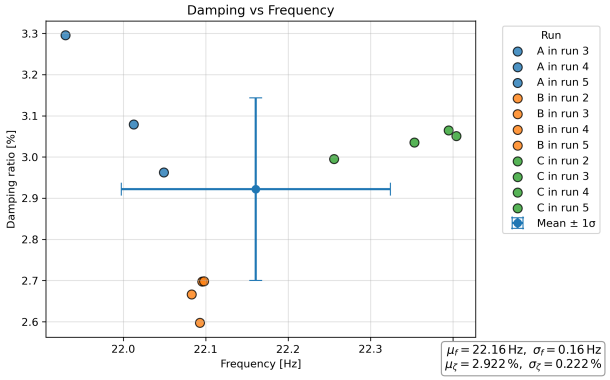

Figure E.85: Cluster DB1

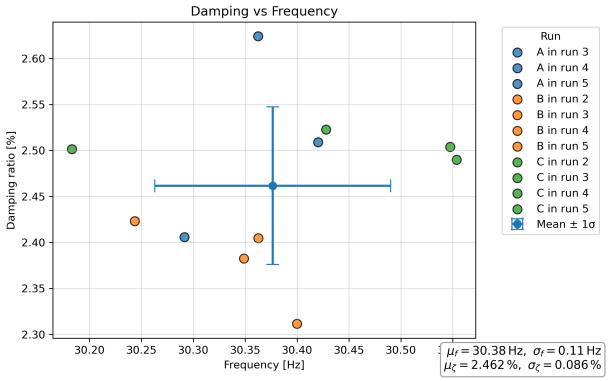

Figure E.86: Cluster DB2

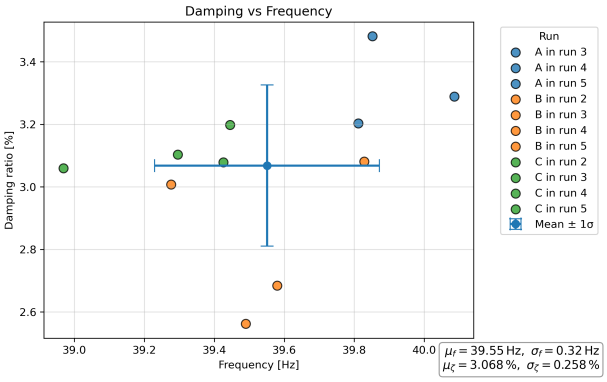

Figure E.87: Cluster DB3

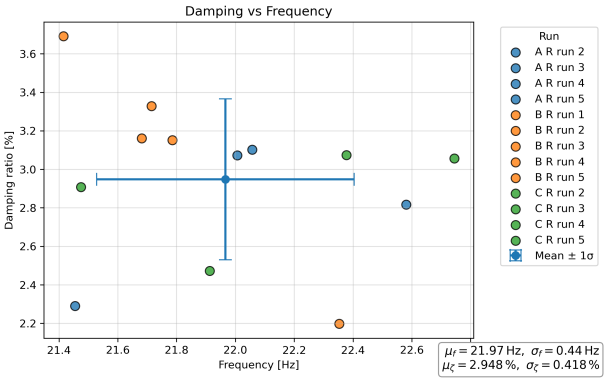

Figure E.88: Cluster DT1

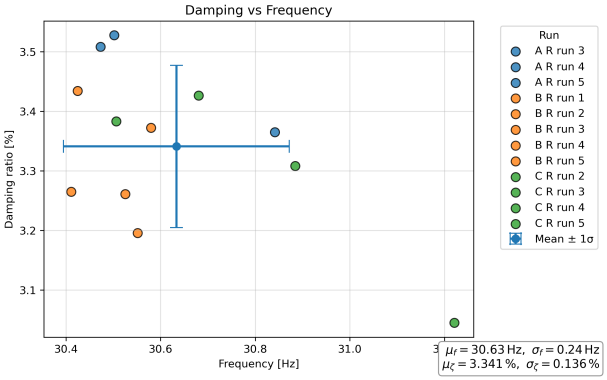

Figure E.89: Cluster DT2

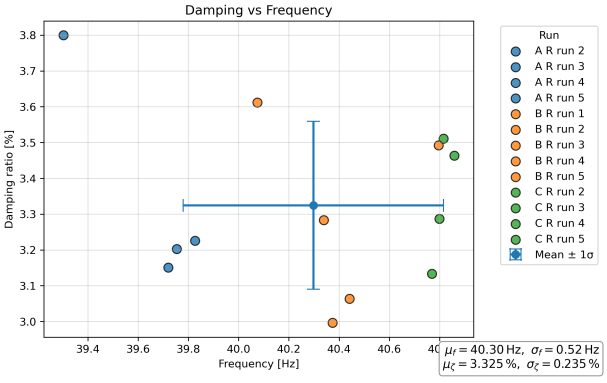

Figure E.90: Cluster DT3

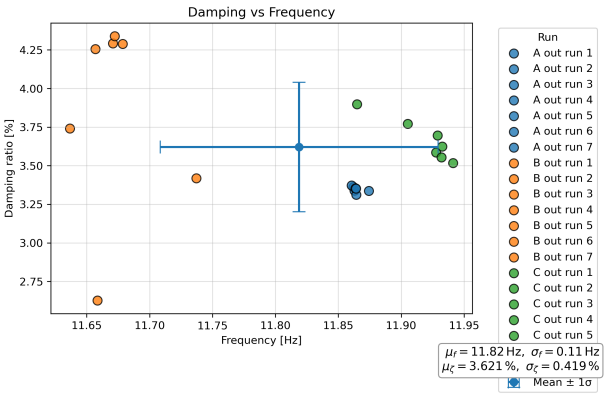

Figure E.91: Cluster WB1

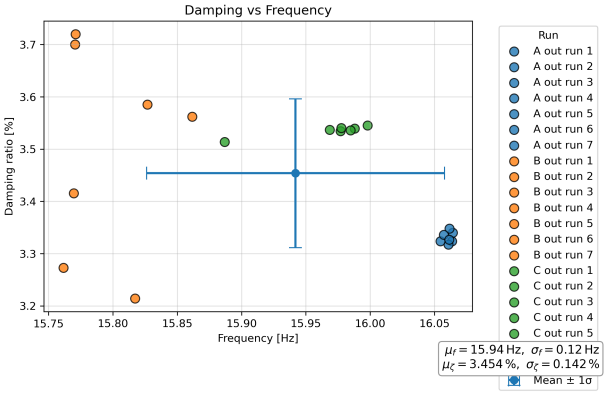

Figure E.92: Cluster WB2

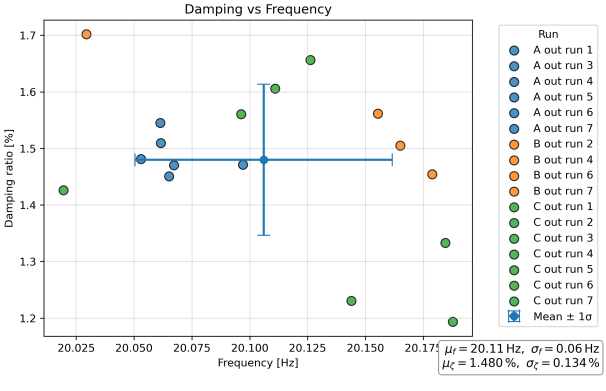

Figure E.93: Cluster WB3

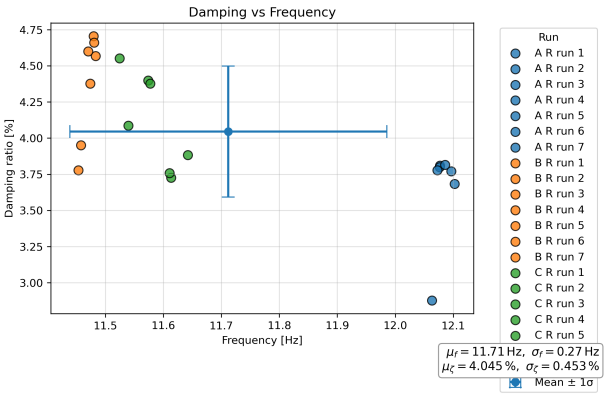

Figure E.94: Cluster WT1

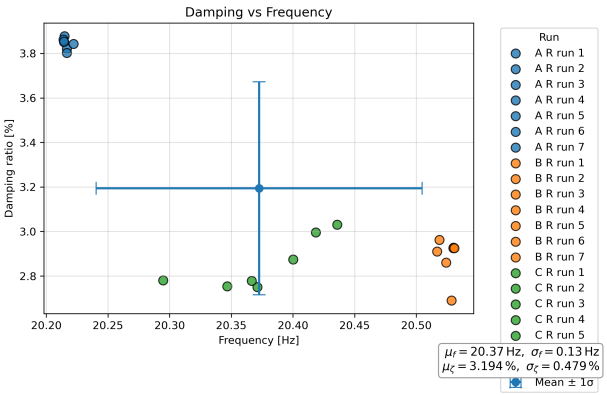

Figure E.95: Cluster WT2

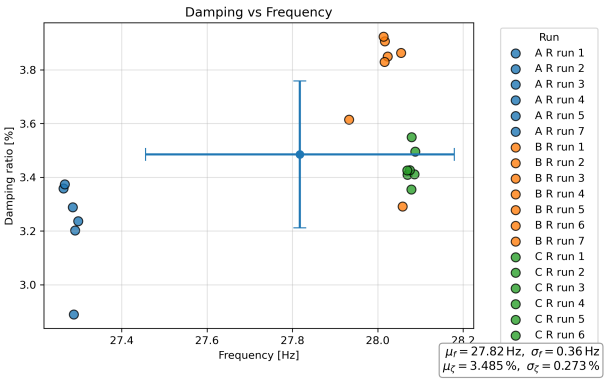

Figure E.96: Cluster WT3

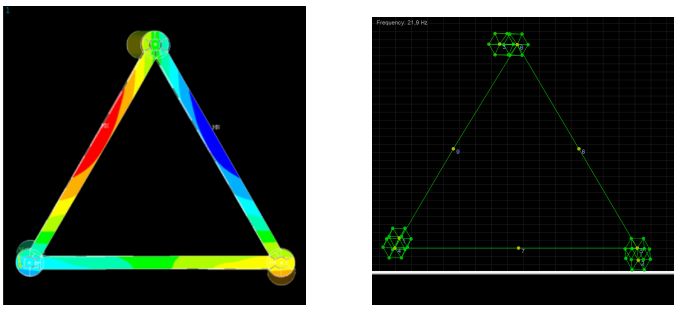

(a) Mode 1a FEM representation

(b) Dry Torsion, Cluster 1.

Figure E.97: Top view comparison of Mode 1a and Dry torsion Cluster 1.

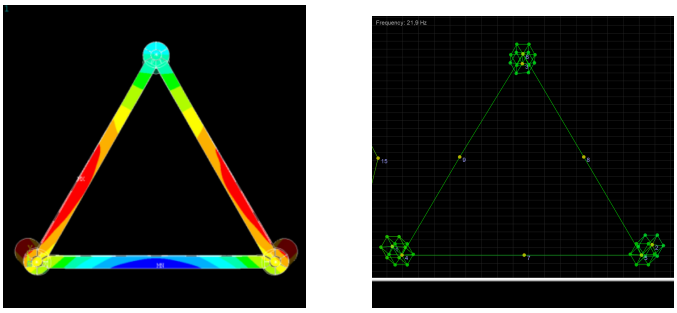

(a) Mode 1b FEM representation

(b) Dry bending, Cluster 1

Figure E.98: Top view comparison of Mode 1b with and FEM representation.

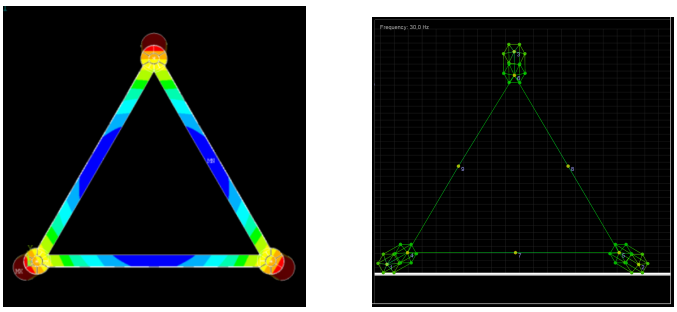

(a) Mode 2 Experimental representation

(b) Dry bending, Cluster 2

Figure E.99: Top view comparison of Mode 2 with and FEM representation.

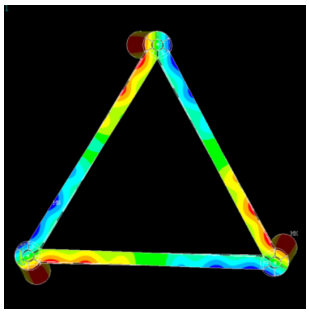

(a) Mode 3 FEM representation

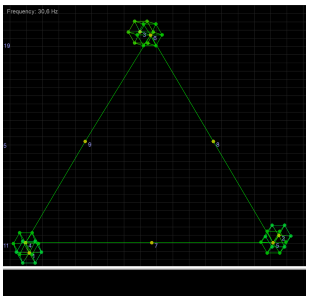

(b) Dry torsion Custer 2

Figure E.100: Top view comparison of Mode 3 with and FEM representation.

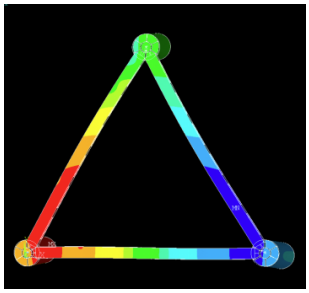

(a) Mode 4a FEM representation

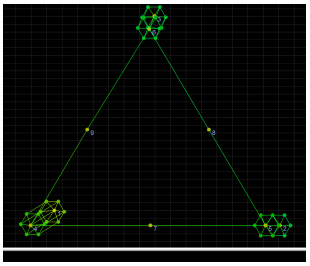

(b) Dry bending, Cluster 3

Figure E.101: Top view comparison of Mode 4a and dry bending Cluster 3.

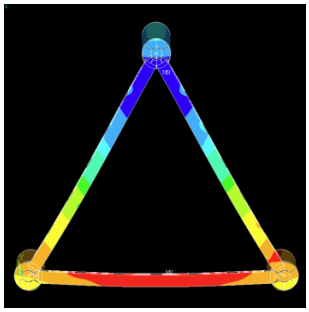

(a) Mode 4b FEM representation

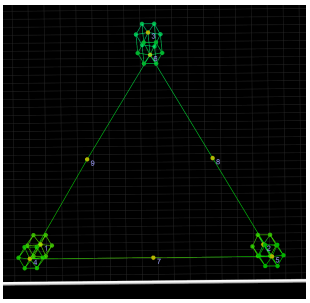

(b) Dry torsion, Cluster 3

Figure E.102: Top view comparison of Mode 4b and dry torsion Cluster 3.

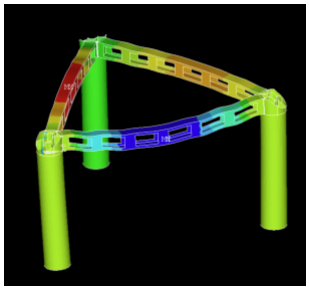

(a) Numerical representation

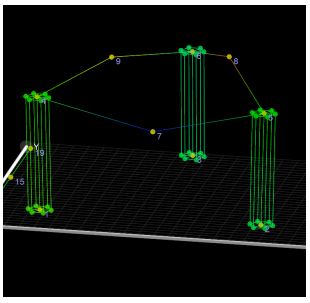

(b) Dry bending, Cluster 4

Figure E.103: Top view comparison of Mode 1a and wet torsion Cluster 1.

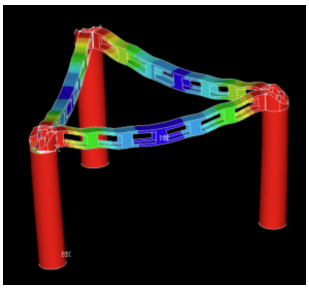

(a) Numerical representation

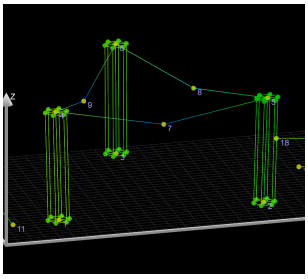

(b) Dry bending, Cluster 5

Figure E.104: Top view comparison of Mode 1b and wet bending Cluster 1.

Appendix E.3. Dry configuration diagonal MAC plots

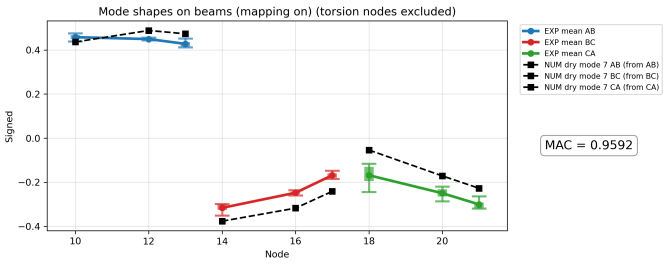

Figure E.105: Dry condition MAC comparison between Cluster DB1 and numerical Mode 1a.

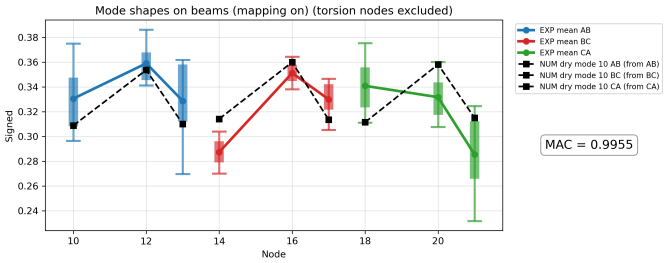

Figure E.106: Dry condition MAC comparison between Cluster DB2 and numerical Mode 2.

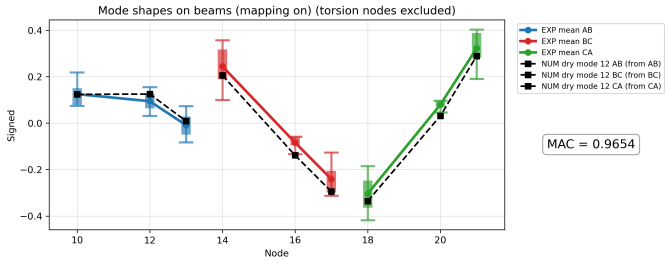

Figure E.107: Dry condition MAC comparison between Cluster DB3 and numerical Mode 4b.

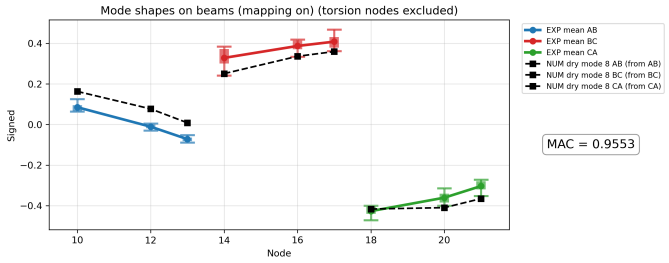

Figure E.108: Dry condition MAC comparison between Cluster DT1 and numerical Mode 1b.

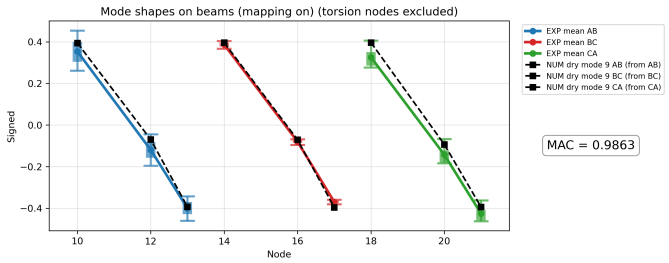

Figure E.109: Dry condition MAC comparison between Cluster DT2 and numerical Mode 3.

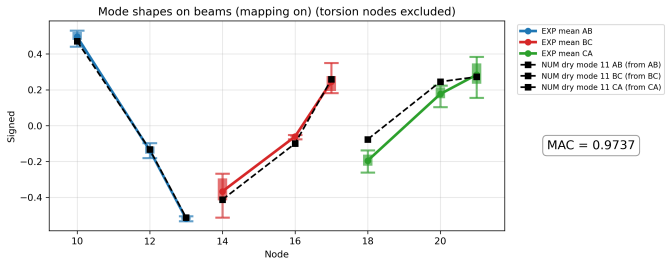

Figure E.110: Dry condition MAC comparison between Cluster DT3 and numerical Mode 4a.

Appendix E.3.1. Imposed asymmetry model

To assess the influence of inter beam stiffness asymmetry on the global mode shapes, a numerical sensitivity study was performed in which the material stiffness of Beam AB was modified to 75% and 125% of its nominal value. All other beams were kept unchanged. This approach isolates the effect of stiffness imbalance without altering geometry or mass distribution.

Observed effect on Frequencies are presented in Table E.26. The resulting global mode shapes are presented in Figures E.111 to E.116. While frequency shifts are observed, the relative floater rotation patterns remain largely unchanged. The orientation and phase relationships between floaters are preserved across all investigated modes.

These results indicate that the global floater rotation angles exhibit limited sensitivity to inter beam stiffness differences. Even under pronounced stiffness asymmetry, the system converges toward similar global deformation patterns, further confirming that the modal characteristics are governed primarily by overall stiffness levels rather than segment specific variations.

Table E.26: Comparison between asymmetric BEAM188 representations and SHELL181 reference frequencies.

Mode	Asym – 75%	Asym – 125%	Sym. E2.0
1a	9.59	10.63	10.60
1b	10.56	11.28	10.60
2	14.43	15.58	14.93
3	16.44	17.95	17.40
4a	23.75	25.75	25.58
4b	23.52	27.47	25.65

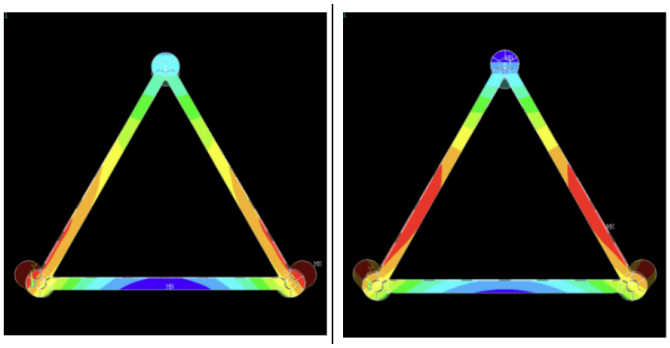

Figure E.111: Mode 1a under asymmetric beam stiffness (Beam AB at 75% and 125% stiffness).

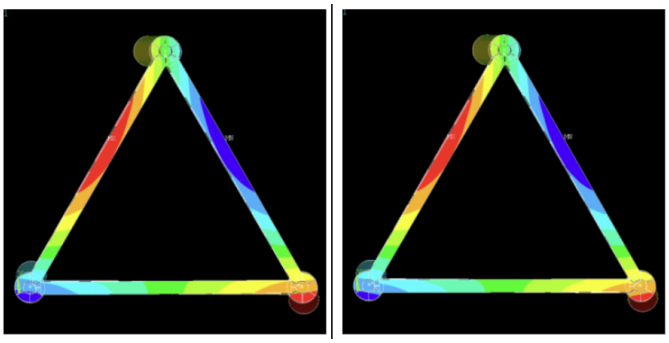

Figure E.112: Mode 1b under asymmetric beam stiffness (Beam AB at 75% and 125% stiffness).

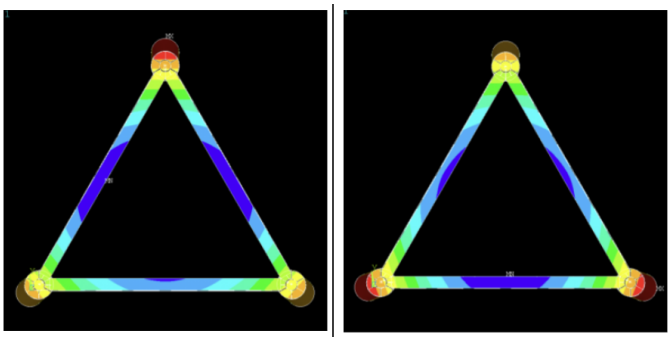

Figure E.113: Mode 2 bending under asymmetric beam stiffness (Beam AB at 75% and 125% stiffness).

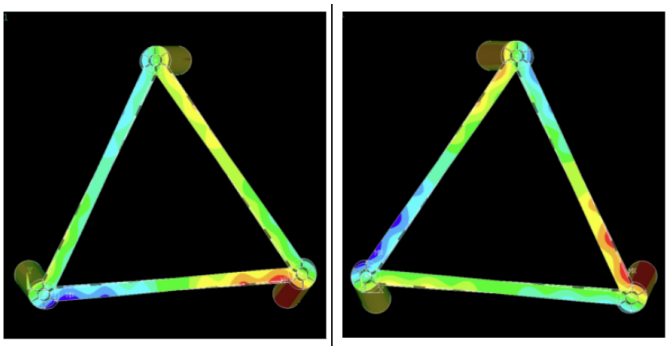

Figure E.114: Mode 3 torsion under asymmetric beam stiffness (Beam AB at 75% and 125% stiffness).

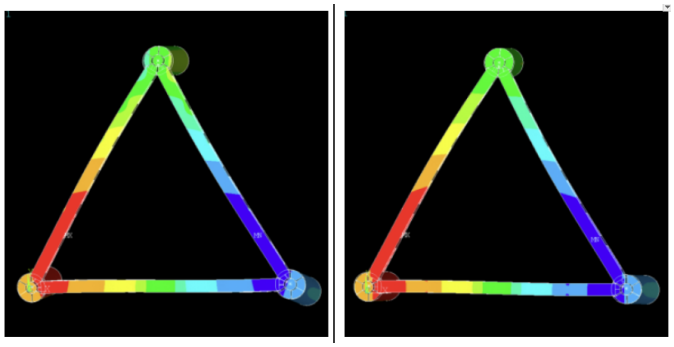

Figure E.115: Mode 4a under asymmetric beam stiffness (Beam AB at 75% and 125% stiffness).

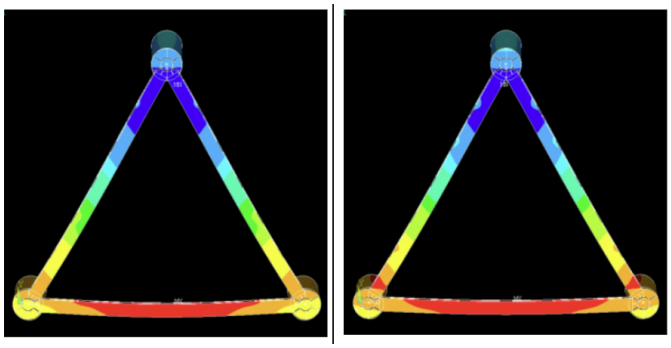

Figure E.116: Mode 4b under asymmetric beam stiffness (Beam AB at 75% and 125% stiffness).